Modélisation du phénomène d'hémolyse au sein d'un dispositif d'assistance ventriculaire gauche (LVAD)

Ali Maghouli

HESAM UNIVERSITÉ

Arts et Métiers Sciences et Technologies

ÉCOLE DOCTORALE SCIENCES DES MÉTIERS DE L'INGÉNIEUR
[Laboratoire de Mécanique des Fluides de Lille – Campus de Lille]

THÈSE

présentée par : Ali MAGOULI

soutenue le : Mai 2023

pour obtenir le grade de : Docteur d'HESAM Université

préparée à : École Nationale Supérieure d'Arts et Métiers

Spécialité : Génie énergétique

Modélisation du Phénomène d'Hémolyse au Sein d'un Dispositif d'Assistance Ventriculaire Gauche (LVAD)

THÈSE dirigée par :
Mme. Annie-Claude BAYEUL-LAINÉ

et dirigée par :
M. Olivier COUTIER-DELGOSHA
Mme. Sophie SIMONET

Jury

Mme Regiane FORTES-PATELLA, Professeur, Université Grenoble Alpes, Laboratoire des Écoulements Géophysiques et Industriels	**Rapporteure**
M. Miguel FERNANDEZ, Directeur de Recherche, Inria Paris	**Président**
M. Stéphane GARRIGUE, Directeur scientifique, FineHeart	**Examinateur**
Mme Annie-Claude BAYEUL-LAINÉ, Maître de Conférences Emérite HDR, Arts et Métiers Sciences et Technologies	**Examinatrice**
M. Olivier COUTIER-DELGOSHA, Professeur, Arts et Métiers Sciences et Technologies	**Examinateur**
Mme Sophie SIMONET, Maître de Conférences, Arts et Métiers Sciences et Technologies	**Examinatrice**
M. Mohammad HADDADI, Directeur Recherche et Développement, FineHeart	**Invité**

THÈSE

Acknowledgment

Firstly, I would like to express my gratitude to Prof. Annie-Claude Bayeul-Lainé, Prof. Olivier Coutier Delgosha, and Prof. Sophie Simonet, my supervisors at **Arts et Métiers, ENSAM**, for providing me with the opportunity to pursue my doctoral studies. Their insightful suggestions and constructive feedback have significantly enhanced the quality of my Ph.D. work.

I extend my sincere thanks to my colleagues at **Medrik Dynamic Technology**, especially Dr. Laure Magnan, Maryam Haddadi, Zahra Charkhchiha, Rita Nsimba, and Mouna El-Dhaher, for their invaluable assistance with my work and for making my stay in France a memorable experience. It has been a pleasure working with such a wonderful team.

I am grateful to my colleagues at **FineHeart** for sharing their in vivo and in vitro data of their innovative blood pump (the ICOMS). Additionally, I would like to thank Dr. Stephane Garigue and Dr. Mohammad Haddadi for reviewing my thesis work and providing helpful feedback.

I would also like to express my appreciation to the Advanced Research Computing (ARC) at **Virginia Tech** for providing me with access to their powerful computational platform. I am especially thankful to my friend from ENSAM, Yang Zhidan, for providing me with guidance on how to use the supercomputer.

Finally, I would like to convey my love and gratitude to my wife, my parents, my wife's parents, and friends, Dr. Mohammad Sadegh Karimi and Hossein Talebi, for their unwavering support throughout my Ph.D. journey.

Abstract

In recent years, the idea of using a mechanical pump as a left ventricle assist device is being well developed by several groups. Meanwhile, one of the challenges in this field is the occurrence of biological phenomena such as hemolysis. From an engineering point of view, a solution to this problem is to provide an accurate and efficient numerical method to predict the phenomenon. Hemolysis models are typically based on equivalent scalar stress and exposure time. Meanwhile, they are inaccurate in predicting the absolute values of the hemolytic parameters. The main objective of this thesis is to provide a model that can forecast the phenomena precisely. This work aims to study the impact of considering extensional stresses as the main reason for hemolysis in the three test cases: FDA nozzle benchmark, FDA pump benchmark, and FineHeart innovative blood pump (the ICOMS). For the first two geometries, the standard models provided by FDA, the objective is to validate the numerical methodology. While for the more realistic test case, the FineHeart blood pump, the final goal is to provide some pieces of advice to reduce the hemolysis level.

For the FDA nozzle benchmark, firstly, the accuracy of the steady flow simulation was validated by comparing the predicted normalized axial velocity in several sections with the experimental data. For that purpose, the Reynolds-Averaged Navier-Stokes (RANS) equations in conjunction with three different turbulence models k-ϵ, k-ω, and k-ω SST were employed. As expected, the k-ω SST turbulence model was found to be the most accurate model. In the next step, hemolysis indexes were calculated using different expressions for the equivalent stress. In this case, the impact of scaling up the extensional stresses on predicted hemolysis is studied by adding a coefficient C_n to equivalent stress. It is concluded that the hemolysis index would be in a reliable range of $18<C_n<30$. Moreover, the impact of different C_n values have been studied for several species. Comparing the results, the C_n coefficient can make a wide range of hemolysis, especially for higher values of it.

For the FDA pump benchmark, transient simulations were conducted with the k-ω SST as the turbulence model. In the first step, hemodynamic parameters, velocity, and pressure were validated by comparing CFD results with FDA experimental data. Secondly, the hemolysis power-law model was added to the simulations using the same expression for the equivalent stress. Comparisons with experimental measurements have indicated that the new methodology provides accurate hemolysis

predictions. In addition, the impact of C_n is studied and it is shown that the hemolysis index is highly impacted by the C_n value, and $18<C_n<27$ is found to be an appropriate range.

Finally, the study conducted transient simulations using identical configurations for FineHeart innovative blood pump, the ICOMS. Hemodynamic parameters, such as velocity and pressure, were compared and validated using two types of experimental data provided by the company: correlation loop tests and particle image velocimetry tests. Subsequently, predictions of hemolysis were compared and verified using in vitro data. The study presents and discusses the local values of hemolysis levels, which allowed for the identification of suggestions to decrease hemolytic levels for the blood pump.

List of Contents

Table of Figures

Table of Tables

Acronyms

AHA	American Heart Association
ANN	Artificial Neural Networks
CFD	Computational Fluid Dynamics
CVDs	Cardiovascular Diseases
EF	Ejection Fraction
FDA	Food and Drug Administration of the United States
GGI	General Grid Interface
HF	Heart Failure
HFrEF	Heart Failure with Preserved Ejection Fraction
HFrEF	Heart Failure due to Reduced Ejection Fraction
HI	Hemolysis Index
IABP	Intra-Aortic Balloon Pump
ICOMS	Implantable Cardiac Output Management System
LV	Left Ventricle
LVAD	Left Ventricle Assist Device
MIH	Modified Index of Hemolysis
PfHb	Plasma Free Hemoglobin
PIV	Particle Image Velocimetry
RANS	Reynolds-Averaged Navier-Stokes
RBC	Red Blood Cell
SST	Shear Stress Transport
TAH	Total Artificial Heart

URANS	Unsteady Reynolds-averaged Navier-Stokes
VAD	Ventricular Assist Device
WHO	World Health Organization

Nomenclatures

Latin Letters

C	A non-dimensional constant in the power-law model	-
C_n	Weighting coefficient in the equivalent stress expression provided by Faghih and Sharp	-
d_t	Throat diameter in the FDA nozzle benchmark	m
D_{LB}	Non-dimensional damage	-
e	The error of the simulation compared to the reference results	%
F_1	The first blending function in the k-ω SST turbulence model	-
F_2	The second blending function in the k-ω SST turbulence model	-
h	Enthalpy of the fluid	J
HI	Hemolysis Index	-
H	The ratio of released hemoglobin to total hemoglobin within the RBC	mg/mg
Hct	Hematocrit	%
k	Turbulent kinetic energy	j
k_T	Heat transfer coefficient	W/m^2K
MIH	Modified index of the hemolysis	mg/mg
n	Rotational Speed	rpm
P	Pressure	Pa
P_{hyd}	The hydraulic power of blood pumps	Watts
P_{mech}	The mechanical power of blood pumps	Watts
P_{mech}	Total Pressure generation of a pump system	Pa
P_{tot}	Total Pressure	Pa
$\widetilde{P}_k$	The rate of turbulent kinetic energy production	-
$\overline{R}_{ij}$	Unknown tensor in k-ω SST turbulence model	-
t	Exposure time	s
$\bar{t}$	Averaged exposure time	s
time	Free hemoglobin sampling interval time in hemolysis tests	min

T	Temperature	K
u_j	Velocity component in j direction	m/s
$\tilde{u}_j$	Density weighted average velocity in j direction	m/s
U_z	Axial velocity in the FDA nozzle benchmark	m/s
$\overline{U_z}$	Mean axial velocity at the inlet for the FDA nozzle benchmark	m/s
U_z^*	Normalized axial Velocity in the FDA nozzle benchmark	m/s
V	The volume of the blood pump to the total loop volume	-
y	Distance from the wall in k-ω SST turbulence model	m

Greek Letters

α	A non-dimensional constant in the power-law model	$-$
α_1	A Coefficient in k-ω SST turbulence model	$-$
α_2	A Coefficient in k-ω SST turbulence model	$-$
β	A non-dimensional constant in the power-law model	$-$
β^*	A Coefficient in k-ω SST turbulence model	$-$
β_1	A Coefficient in k-ω SST turbulence model	$-$
β_2	A Coefficient in k-ω SST turbulence model	$-$
$\dot{\gamma}$	Shear rate	s^{-1}
ΔP	Generated pressure by a blood pump	Pa
η	The efficiency of blood pumps	$-$
η_{exp}	The efficiency of blood pumps calculated based on an experimental approach	$-$
η_{CFD}	The efficiency of blood pumps calculated through a numerical approach	$-$
μ	Dynamic viscosity	cP
ν_t	Eddy Viscosity	$Pa.s$
ρ	Density	kg/m^3
σ_{k1}	A Coefficient in k-ω SST turbulence model	$-$
σ_{k2}	A Coefficient in k-ω SST turbulence model	$-$
$\sigma_{\omega 1}$	A Coefficient in k-ω SST turbulence model	$-$
$\sigma_{\omega 1}$	A Coefficient in k-ω SST turbulence model	$-$
τ	Stress	Pa
ω	The specific rate of dissipation	$-$

1. Introduction

1.1. Background of the Work

In the American Heart Association (AHA) guidelines, Heart Failure (HF) is defined as "a complex clinical syndrome that can result from any structural or functional cardiac disorder that impairs the ability of the ventricle to fill or eject blood" [2,3]. From a physiological point of view, Heart failure means reducing the heart's efficiency in sending or receiving blood flow according to the needs of natural organs. According to the latest statistics from the World Health Organization (WHO), cardiovascular diseases (CVDs) are the leading cause of death globally, taking an estimated 17.9 million lives each year [1]. Among developed societies, the prevalence of recognized heart disease is estimated at 1% to 2% of the elderly population, with associated healthcare costs in the United States exceeding $30 billion annually.

One old method of classification of heart failure is by the side of the heart involved, left heart failure versus right heart failure (see Figure 1-a). Right heart failure compromises blood flow to the lungs compared to left heart failure compromising blood flow to the aorta and consequently to the brain and other organs. However, mixed presentations are common, and left heart failure is a common cause of right heart failure. A more accurate characterization of heart failure can be considered by measuring ejection fraction (EF), or the proportion of blood pumped out of the heart during a single contraction [1]:

1. Heart Failure due to Reduced Ejection Fraction (HFrEF) occurs when the heart muscles are not sufficiently powerful to eject the blood flow through the ejection phase[1] (Figure 1-b).

[1] Systolic phase

2. Heart Failure with Preserved Ejection Fraction (HFpEF) occurs when the heart muscles have no problem ejecting the blood flow but are not effectively operating in the relaxation phase[2] (see Figure 1-c).

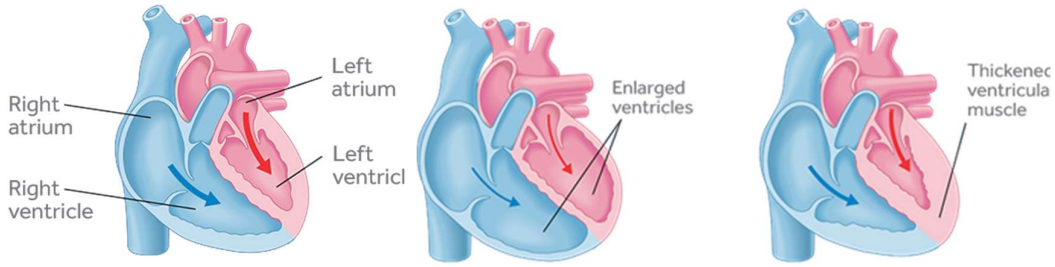

Figure 1. a) Normal heart anatomy b) enlarged ventricles due to HFrEF c) thickened ventricle muscles due to HFpEF [2].

In all stages of heart failure treatment, the main goals include treating the underlying cause, improving symptoms, stopping the progression of the disease, and ultimately increasing the quality of life of the patient. In the initial stage, these treatments are in the form of medication and lifestyle changes. In acute cases of the disease, heart transplantation is known as the best option for treatment. Although this treatment method is not applicable for all patients who need to receive an organ due to the severe limitation of the number of transplanted hearts, and in more than 90% of cases, the need for temporary or permanent replacement treatment has been fully felt. Meanwhile, the spread of CVDs has motivated scientists and innovators to provide an appropriate assist device for the heart. As mentioned, the objective of all these systems is to make a bridge between heart failure and heart transplantation. Total Artificial Heart (TAH), Intra-Aortic Balloon Pump (IABP), and Ventricular Assist Device (VAD) are different types of assist devices.

Total artificial heart systems include two mechanical pumps that take over heart duties by completely removing the ventricles from the cardiac circuit. Due to the complexity and problems of the implantation, the use of this assist device is limited compared to the other two types [3]. Intra-aortic balloon pump is a system that is usually used for a short period, less than ten days, and mainly in patients suffering from heart attacks to reduce the load on the left ventricle. After being implanted inside the aorta, the balloon is lumped by the flow of helium gas, which increases the blood flow of the coronary artery. On the other hand, the suction caused by emptying the balloon at the beginning of the ventricular contraction reduces the workload of the left ventricle.

A ventricular assist device (Figure 2-a), commonly known as a blood pump, is a mechanical pump connected to the ventricular muscles and related arteries to assist the ventricle and increase cardiac output. This equipment is used for heart transplant patients and patients without transplant conditions. Due to the limitations of heart transplants, VAD use as a targeted therapy has been increasing in recent

[2] Diastolic phase

years. Almost one out of every two patients with acute conditions has been treated with this equipment [4].

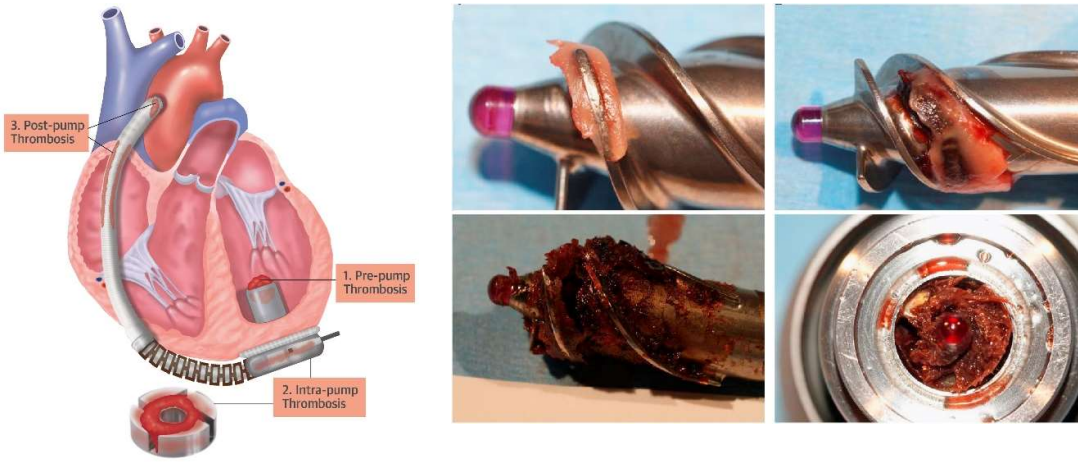

(a) (b)

Figure 2. a) positioning of a conventional ventricular assist device in the left ventricle and thrombosis issues of LVAD systems [5] b) Thrombosis in the heart mate 2, a commercial LVAD, after implantation and operation [6].

In the meantime, despite extensive research to develop these devices, undesirable natural phenomena have created challenges for them. To be more specific, the occurrence of hemolysis and thrombosis causes the formation of blood clots inside the blood pumps and prevents them from running (see Figure 2-b). Hemolysis is the release of hemoglobin from red cells into plasma due to the damage of the cells' membranes (Figure 3) [7], while thrombosis is the formation of a blood clot within the cardiac system and can occur both within the arteries and ventricles [8]. Due to this issue, deep research has been done on hemolysis and thrombosis during the last decades. Subjects include physiological aspects of two phenomena [9–11], the relationship between hemolysis and thrombosis [12–14], experimental prediction of their onset [15–18], and modeling of two phenomena [19–21]. At the moment, it is proven that thrombosis in the cardiovascular system results from hemolysis [12,22]. In other words, controlling the hemolysis level in an LVAD system leads to decreasing thrombosis inside it, which requires advanced tools and equipment.

The tools used in blood pump design include experimental methods and numerical simulations. Flow visualization techniques and in vitro and in vivo tests are among the most used examples of experimental methods. Flow visualization is usually performed using the Particle Image Velocimetry (PIV) technique and provides quantitative information regarding the flow field [23–26]. The PIV results enable us to inspect and monitor critical hemolytic points in the system. Nevertheless, weak points of the PIV technique, including the low resolution of the images, result in low-quality and unreliable observations of the flow's pattern. Moreover, there is no possibility of using the blood itself as the testing fluid within the PIV. On the other side, despite revealing the general information about the test equipment, in vivo experiments are highly complex, expensive, and require transplantation into the circulatory system of

the living organism. The dependence of this type of study on the conditions of the target organism leads to the inevitable occurrence of uncertainty in the results. Although these tests are safe for predicting natural conditions, they face many limitations and problems. An in vivo test requires using a large amount of fresh blood as the test fluid, and it is not easy to access a sufficient amount of human blood. On the other hand, blood-like fluid or animal samples show different behavioral characteristics than human blood [18]. All these factors lead to the complexity of providing accurate and reproducible values through this experimental method.

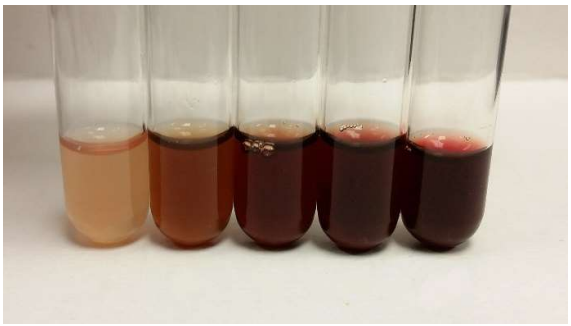

Figure 3. In the case of Hemolysis, the released hemoglobin will cause the plasma to appear cherry red [27].

From an engineering point of view, one possible solution is to predict and remove the sources of the phenomenon using mathematical models. Hemolysis modeling can help LVAD developers reduce the phenomenon's risks in these devices. This objective requires an accurate and reliable model that has to act as a connection between the mechanical and the physiological aspects of the blood flow.

1.1.1. Physiological and Rheological Behavior of Blood

Blood is a heterogeneous mixture of suspended particles including blood cells and platelets in the plasma fluid space (Figure 4-a). Red blood cells (RBCs), also called erythrocytes, are the most important components of the blood, comprising nearly half of the blood volume [20]. Consequently, the mechanical and rheological behavior of the blood is usually dominated by RBCs. Figure 4-b indicates the statistical shape and dimension of red blood cells. As shown in this figure, a red blood cell has a biconcave shape, that helps it to increase the rate of oxygen transformation [28].

Like other intracellular elements, RBCs don’t have a cell nucleus. This fact allows hemoglobin, a protein molecule responsible for carrying oxygen, to use the maximum space. The total amount of hemoglobin (intracellular and extracellular) in the blood is typically 12–13.5 g/dl. However, the normal level of extracellular hemoglobin, called plasma-free hemoglobin (PfHb), is very small (0.008 g/dl). Plasma-free hemoglobin is the most important parameter to quantify the hemolysis level. In fact, in the case of hemolysis, the thick membrane of RBCs is ruptured, and free hemoglobins are released into the plasma. Consequently, the concentration of the PfHb increases in the blood.

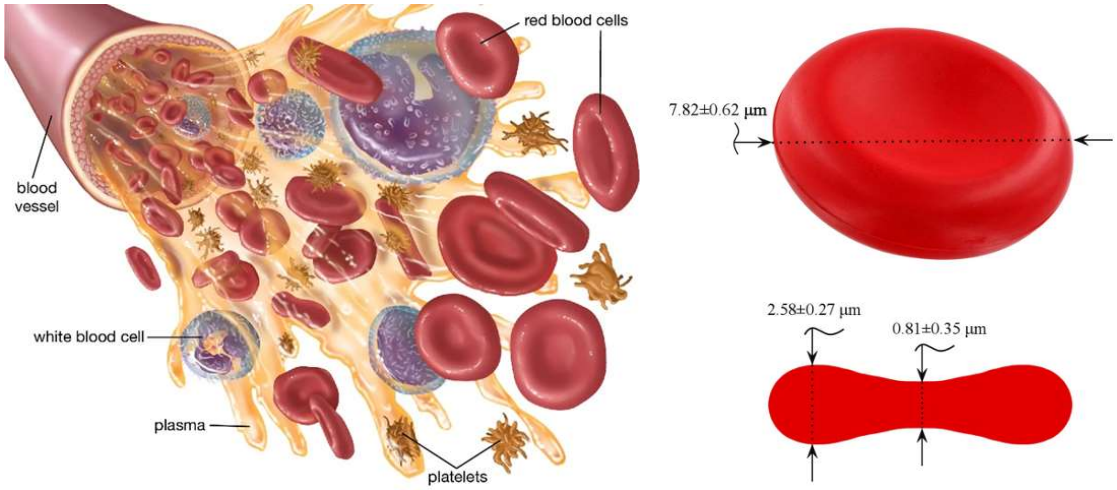

(a) (b)

Figure 4. a) blood components diagram [29]. b) Shape and statistical dimensions of red blood cells [20].

A typical human RBC has a diameter of approximately 7.82±0.62 µm and a thickness at the thickest point of 2.58±0.27 µm and a minimum thickness in the center of 0.81±0.35 µm, being much smaller than most other human cells (see Table 1). These cells have an average volume of 94±14 μm^3. Hematocrit, also known by several other names, is the volume percentage of red blood cells in the blood, measured as part of a blood test. The measurement depends on the number and size of red blood cells. For an adult male, the average value for the hematocrit is 47±7 %. While for female adults, the hematocrit is 42±6 %.

Table 1. Statistical properties of red blood cells [30–32].

Property of RBC	Value	Unit
Diameter	7.82±0.62	µm
Volume	94±14	μm^3
Membrane thickness	5-10	nm
Hematocrit (adult male)	47±7	%
Hematocrit (adult female)	42±6	%
Normal life	104±14	days

Blood exhibits various rheological and mechanical characteristics under different conditions. This issue doubles the importance of the studied geometry and flow conditions for modeling blood flow behavior. In general, blood is a viscoelastic fluid, which reduces its effective viscosity when exposed to high shear rates due to the deformation of red blood cells. However, for specific ranges of shear rates ($\dot{\gamma} < 10^{-2}\ s^{-1}$ and $\dot{\gamma} > 10^{2}\ s^{-1}$), the viscosity of the blood tends to have constant values (Figure 5) [33]. In other words, the behavior of the blood becomes a Newtonian fluid.

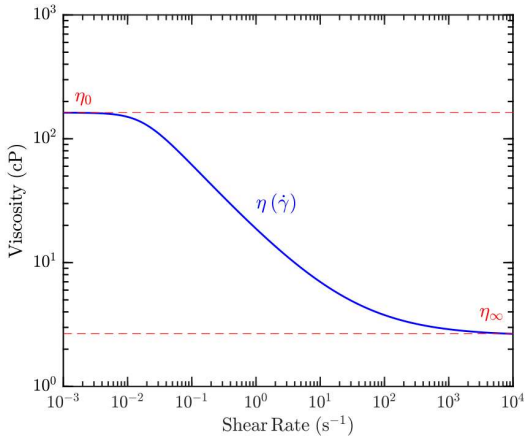

Figure 5. Viscosity in (cP) against shear rate in (s^{-1}) for the blood provided by Aycock et al. (2016) [33].

To our knowledge, most of the flow regions within blood pumps are prone to relatively intense shear rates ($\dot{\gamma} > 10^2\ s^{-1}$) [34]. For example, Mohammadi et al. (2022) [35] reported that the volume average of the shear rate in several regions of the FDA blood pump is over 300 s^{-1}. Therefore, it could be a reasonable hypothesis to consider the blood as a Newtonian fluid with constant viscosity.

1.2. Literature Review

In recent years, computational fluid dynamics analysis has been increasingly used in the development process of medical blood-contacting devices, especially ventricular assist devices. Most of the studies were focused on investigating the characteristics of the flow and the performance of the devices. In some works, numerical methods have been implemented as a design improvement and optimization tool. Finally, they are being used as a prediction process to evaluate blood pumps in physiological aspects like the hemolysis phenomenon. In the following, research related to these issues is explained and reviewed.

1.2.1. Numerical Simulations and Blood Pumps

In recent years, Computational Fluid Dynamics (CFD) analysis has been increasingly used in the development process of blood-contacting medical devices and especially ventricular assist devices. Most of the studies are focused on investigating the flow field and the performance of the equipment. Also, in some works, numerical methods have been used for design improvement and optimization. In the following, related studies are explained and reviewed.

Numerical studies of hydraulic performance analysis and investigation of the blood damage in various types of blood pumps have been started since the 1990s. Pinotti and Rosa (1995) conducted one of the first studies in this field, focusing on a bladeless centrifugal blood pump [36]. They used two co-rotating as a simplified model of a centrifugal pump to study the effect of flow rate on hemolysis

intensity. Simulations revealed that flow behavior at the entrance region of the pump is the main cause of blood damage in this device. Song et al. (2004) [37] used this tool to predict flow behavior inside another blood pump (HeartQuest). The main objective of their work was to evaluate the impact of flow unsteadiness at the pump's inlet (see Figure 6). They compared CFD results in two cases (Transient and steady inlet flow) by monitoring flow parameters, including the pressure generation, fluid forces and moment, and discharge velocity. In conclusion, they noted that neglecting the pulsed flow rate causes meaningful simulation errors (20-45%).

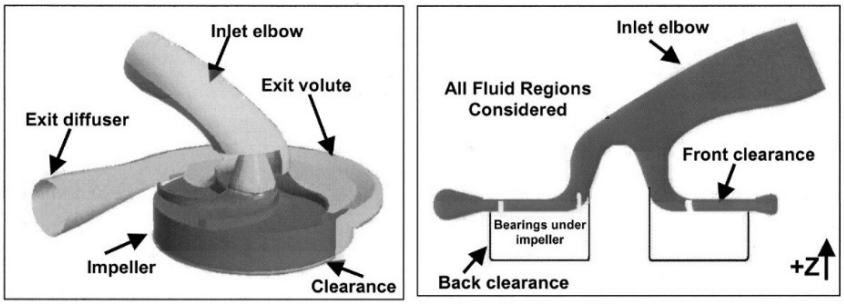

Figure 6. Computational fluid dynamics model used by Song et al. (2004) [37]. Regions include an inlet elbow, rotor, clearance region between the internal housing and rotor, exit volute, and exit.

In 2005, Untaroiu et al. [38] used CFD simulations as well as experimental measurements to improve the performance of an axial blood pump (LEV-VAD). Three different design strategies or the pump's diffuser (three-bladed and six-bladed diffuser) were simulated, tested, and compared for wide ranges of flow rates (Q) and rotational velocity (n) ($2 < Q < 10\,lpm,\ \ 5000 < n < 8000\,rpm$). As a consequence of a numerical and experimental work, it was found that the three-bladed configuration for the diffuser results in better performance.

During the 2000s and 2010s, several papers were published focusing on improving the blood pumps' hemodynamic performance using numerical methods [25,39–42]. Meanwhile, other studies concentrated on the numerical models to develop more reliable ways of the simulations. For example, Al-Azawy et al. (2016) [43] investigated the impact of turbulence model selection on the accuracy of the CFD results. In this study, numerical predictions were carried out using various turbulent models (Spalart-Allmaras, k-ε, k-ω, k-ω SST, RSM) inside a centrifugal blood pump developed by Medvitz et al. (2008) [44] (see Figure 7). The outcomes of different numerical methods were compared with the experimental PIV data. Apparent discrepancies were observed between the results, emphasizing the importance of turbulent model selection. In another study, Al-Azawy et al. (2017) [45] used the same test case to study the impact of considering the blood flow as a non-newtonian fluid in terms of viscosity. Two common models for non-Newtonian blood flow were compared to the Newtonian model to investigate their impact on predicted levels of wall shear stress (WSS) and turbulent kinetic energy (TKE). These two parameters have been studied as they can impact the hemolysis predictions directly.

Numerical results indicate that the WSS and TKE are generally predicted to be higher in a non-Newtonian fluid than in a Newtonian one.

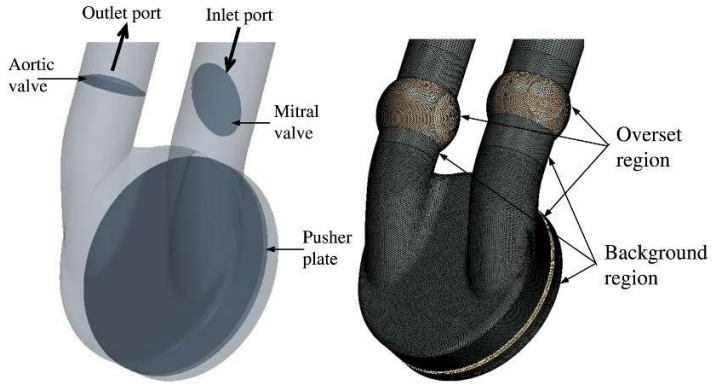

Figure 7. The geometry of a centrifugal pump was developed by Medvitz et al. (2008) [44] and used as a test case by Al-Azawy et al. (2016, 2017) [43,45].

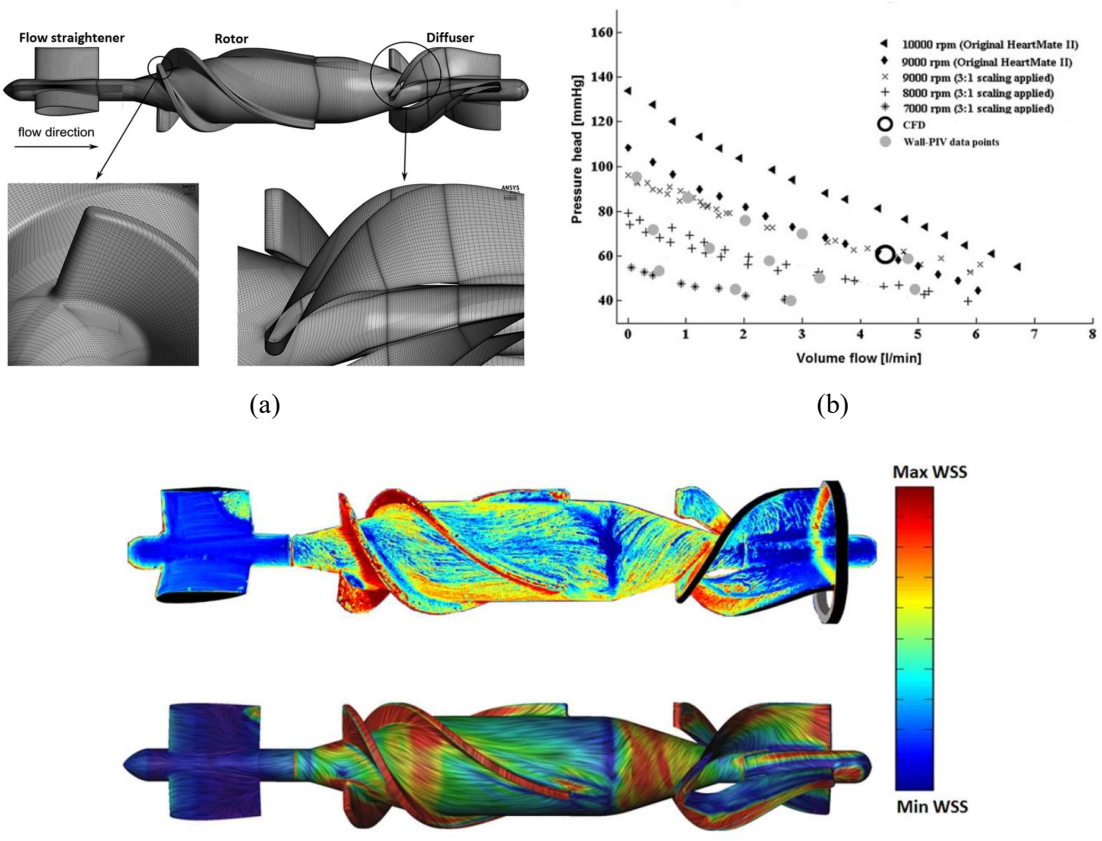

(a) (b)

(c)

Figure 8. Schule et al. (2016) [24] implemented CFD simulations as well as experimental techniques to evaluate an axial blood pump, HeartMate 2. a) Surface imprint mesh generated to perform hemodynamic simulations. b) Comparison between experimental and numerical H-Q curve to evaluate the numerical method. c) Comparison between calculated WSS in PIV measurements and CFD study.

Schule et al. (2016) [24] implemented CFD simulations as well as experimental techniques to evaluate an axial blood pump, HeartMate 2 [46] (Figure 8-a). In this work, the near-wall flows'

experimental data were collected using the wall PIV technique and visualized by a paint erosion method. A qualitative comparison was made between PIV-based WSS and the CFD predictions for a particular operating condition ($Q = 4.5\ lpm\ , \Delta P = 59\ mm\ Hg$). Figure 8-c indicates an acceptable agreement between the two results, despite minor discrepancies (i.e., in the impeller's hub). In addition, they evaluated the numerical results regarding hemodynamics, comparing the experimental H-Q curve[3] with the CFD predictions. Figure 8-b indicates the H-Q curve obtained from the correlation loop and CFD output over an operating condition (n=9000 rpm, Q=4.5 lpm). It is clear that the predicted point is within a good range of test data. They concluded that the CFD-based RANS modeling of the heartmate 2 was sufficiently reliable to recreate experimental data, for both test rigs.

In addition to numerous studies investigating the performance of various blood pumps, increasing the efficiency and improving the performance of these devices have also been the focus of some studies. This goal is pursued according to the two procedures of "Design Improvement" and "Optimization". In the "Design Improvement" process, the most favorable design is determined by making changes in the configuration of the basic design and comparing the performance parameters of the resulting configurations. Several articles have been published on the subject of design improvement in blood pumps, including Miyazoe et al. (1999) [47], Anderson et al. (2000) [48], Curtas et al. (2002) [49], Arvand et al. (2004) [50], Zhang et al. (2007) [51], Zhu et al. (2010) [52], Mozaffari et al. (2017) [53].

On the other side, "Optimization" based on numerical simulations is a complicated and high-level procedure compared to "Design Improvement", which requires coupling a numerical solver with the algorithm used for optimization. The "Optimization" process is time-consuming and expensive, mainly due to the algorithms used.

Ghadimi et al. (2019) [54] implemented an optimization process to improve the performance of one of the latest commercial blood pumps, HeartMate 3 [55]. The objective of the work was to develop the HeartMate 3 design in terms of hemodynamics and hemolysis. After parametrizing its geometry, eleven geometric parameters were selected as design variables (Figure 9-a). The target parameters included pressure generation, hemolysis index, and hydraulic efficiency which is the ratio of generated hydraulic power against the required mechanical power ($\eta = P_{hyd}/P_{mech}$). They were optimized based on the three following scenarios in the form of the optimization algorithm (Figure 9-b):

1. Increasing the efficiency (η) as much as possible, increasing the pressure generation (ΔP) by at least 5%, and decreasing the hemolysis index (HI) by at least 5%.
2. Increasing the pressure generation as much as possible, increasing the efficiency, and decreasing the hemolysis index by at least 5%.

[3] H-Q curve: A curve that expresses how much flow rate (Q) can be generated due to the increased head (H) (pressure) by a mechanical pump.

3. Decreasing the Hemolysis index as much as possible, increasing the pressure generation by at least 5%, and increasing the efficiency.

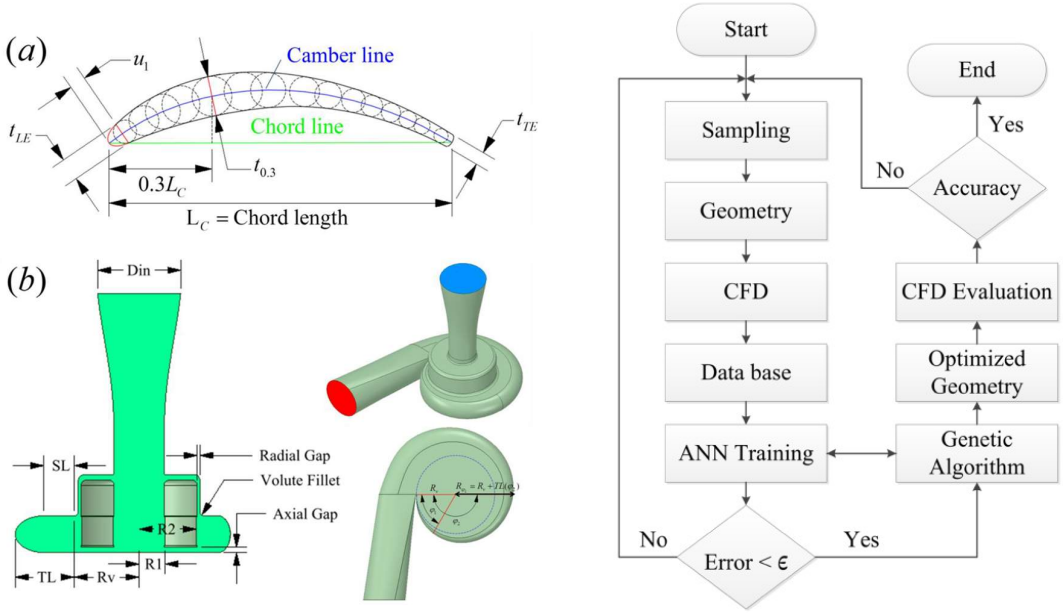

(a) (b)

Figure 9. a) The design parameters used in the optimization process of HeartMate 3 [54]. b) Flowchart of optimization algorithm followed by Ghadimi et al. (2019) [54].

Due to the complexities of numerical simulation and the high number of design variables, solving the optimization problem in the existing algorithm required several years of computations and practically made it impossible. As a result, this group made alternative models for each scenario using artificial neural networks (ANN) and reduced the optimization time to three months. Table 2 indicates the results of the optimization process for each scenario reported by [54]. Considering the importance of the hemolysis index in the design of blood pumps, they suggested the optimized model of scenario 3. This model provides the most efficient design in the hemolysis index, with a 14.7% decrease compared with the base model. Simultaneously, this design significantly improved hydraulic efficiency by 6.1%.

Table 2. The results of the optimized geometries for each scenario were provided by Ghadimi et al. (2019) [54].

Scenario	**Efficiency (η) %**	**Pressure (ΔP) mm Hg**	**Hemolysis ($HI \times 10^4$)**
Base Design	42.51%	93.39	1.77
Scenario 1	47.22%	93.93	1.56
Scenario 2	44.35%	93.46	1.68
Scenario 3	45.69%	93.20	1.51

1.2.2. Hemolysis Modeling

As mentioned in section 1.1, Hemolysis is a phenomenon during which, due to partial or complete damage to the membrane of red blood cells, the hemoglobin contained in them leaks into the blood plasma. Hemolysis is one of the primary problems facing the development and use of blood-contacting devices, especially ventricular assist devices. During the past century, extensive research has been conducted to investigate the nature of hemolysis based on standard procedures [56–60]. However, since the behavior of red blood cells at the microscopic scale is too complex, an adequate mathematical model of blood damage and hemolysis has not been provided yet. Therefore, most of the numerical models only use the macroscopic quantities of the flow, such as the velocity field, without considering any microscopic effect.

Earlier in the 1960s and 1970s, the relationship between shear stress (τ) and exposure time (t), as two mechanical parameters, and the hemolysis phenomena was proven [56,60]. At that time, the researchers' objective was to determine a threshold for the onset of hemolysis. For example, Blackshear et al. [60] provided an explicit formulation to predict the occurrence of hemolysis (equation 1). This formula was later improved by adding a threshold shear stress to the model:

$$\tau t^{0.5} = const. \quad (1)$$

This formula was later improved by adding a threshold shear stress to the model. Other studies observed that hemolysis would never occur for specific shear stress conditions. For instance, Sharp and Mohammad (1999) measured the hemolysis index in various catheters and noted that a threshold shear stress (τ_{th}) should be considered in equation 2:

$$(\tau - \tau_{th})t^{0.5} = const. \quad (2)$$

Table 3. Experimental studies on the threshold shear stress (τ_{th}).

Reference	Species	Viscosity (cP)	Experimental setup	Exposure Time (ms)	Threshold Shear Stress (Pa)
Nevaril et al. (1968) [61]	Human	-	Concentric cylinder	120	300
Forstrom (1969) [62]	Goat	4.2	Jet Nozzle	-	420
Leverett et al. (1972) [63]	Human	3.63	Concentric cylinder	120	150
Paul et al. (2003) [64]	Porcine	5	Concentric cylinder	0.62	400
Lee et al. (2004) [65]	Human	3.1	Concentric cylinder	120	300
Kameneva et al. (2004) [66]	Bovine	6.3	Capillary tube	1	300
Zhao et al. (2006) [67]	Bovine	30	Microfluidic channel	0.002	5170
Boehning et al. (2014) [68]	Porcine	5	Concentric cylinder	0.873	600

The value of the threshold shear stress is reported for different conditions in several references (Table 3). These studies were typically done under specific conditions that were supposed to represent real blood-contacting devices. Generally, the threshold shear stress is measured between 150 and 400, except for two reports with low exposure times (Zhao et al. (2006) [67] and Boehning et al. (2014) [68]).

None of the above equations (equations 1 and 2) can predict the amount of the hemolysis index quantitatively and only explain conditions for the onset of this phenomenon. Consequently, a mathematical model was needed to predict the hemolysis index; Hereafter, several models were provided to do so [15,16]. Hemolysis models can be divided into two general categories, stress-based (semi-empirical) and strain-based (advanced), according to how they relate to flow quantities (Figure 10). The model is stress-based if the hemolysis index is directly calculated with the fluid stress field and is expressed as an explicit function of the flow quantities. On the other hand, strain-based modeling is performed by defining the intermediate equations between the fluid flow field and the deformation quantities of red blood cells. Strain-based models have a higher potential for representing the phenomenon in terms of the physical basis. Of course, this causes more complexity for these models in numerical simulation [20].

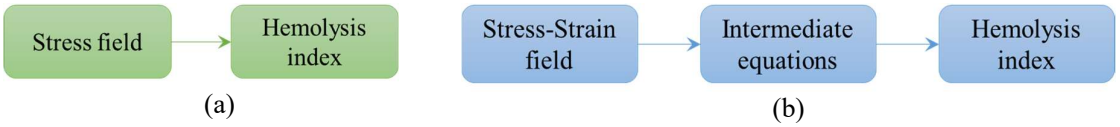

Figure 10. Solution procedure of hemolysis models [19]. a) stress-based models and b) strain-based models.

Laugel et al. (1983) proposed the first model to predict hemolysis quantitatively and locally by focusing on a fully-developed laminar flow in capillary tubes [69]. Measurements were performed for a condition with small shear stress values ($\tau < 30\ Pa$):

$$D_{LB} = k_{LB}\dot{\gamma}^{n} \tag{3}$$

Where, D_{LB} is non-dimensional damage and represents relative free hemoglobin in the blood. Moreover, k_{LB} is a constant parameter that depends on the tube's length and n is an experimental fitness coefficient.

In 2004, Arvand et al. [70] provided a semi-experimental equation to predict hemolysis in rotary blood pumps (equation 4). This formula predicts the hemolysis index as a function of flow parameters: Averaged shear stress ($\bar{\tau}$), Averaged exposure time ($\bar{t}$), blood pump's volume to the total loop volume (V), and the pump's generated pressure (ΔP). They approved that equation 4 is sufficiently reliable to predict hemolysis index for different configurations and operating conditions of the MicroDiagonal Pump (MDP).

$$H = 3.8\bar{\tau}^{-1.9}(\bar{t} \times 10)^{1.5}V^{0.25}\Delta \mathrm{P}^{1.4} \tag{4}$$

Equation 5 is the most conventional reference for hemolysis modeling [19]. The power-law model was proposed by Giersiepen et al. (1990) [15] and obtained from fitting measurement data discussed in

[71,72]. In this equation, H refers to the ratio of released hemoglobin to total hemoglobin within the RBC (usually noted as $\frac{\Delta Hb}{Hb}$). There are three empirical dimensionless constants in this equation: C, α, and β, which have been investigated through experimental studies with certain conditions and geometries [15–18].

$$H = C\tau^{\alpha}t^{\beta} \tag{5}$$

Of course, the use of the power-law model has always faced unanswered questions and shortcomings [73,74]. For instance, Faghih and Sharp (2017) [73] noted that the experimental data of hemolytic levels of fluid stresses exist only for certain conditions (Laminar flows), and they cannot be used for more complex flows.

Despite its shortcomings, the power-law model has been the leading source for the numerical simulation of hemolysis over the years. Over the last two decades, other aspects of numerical simulation with this model have been investigated to improve the performance of numerical methods in predicting Hemolysis phenomena in blood pumps. Some of them examined the general approach to solving the problem, i.e., the respective benefits of the Lagrangian or Eulerian methods. The Eulerian approach has always been more popular due to its more straightforward framework for numerical discretization [75–77]. On the other side, the Lagrangian approach seems to be more complicated as it considers several path lines of the blood flow in space and time [78,79]. Therefore, this type of Hemolysis modeling is more applicable to time-dependent flow regimes. This approach has been reported to provide poor Hemolysis predictions [19]. For instance, Taskin et al. [80] evaluated both approaches for two different test cases: a centrifugal and an axial blood pump. They concluded that the Eulerian method could predict the phenomena with a higher correlation coefficient compared with the Lagrangian one. They also suggested that the Eulerian approach can be used to give relative comparisons of hemolysis in different devices. Considering that this model is used as the basis of simulations in the current research, it is explained in detail in section 1.3.2.

1.3. Governing Equations

Compared with conventional fluids in nature, like water and air, simulating blood flows with sufficient accuracy and precision is indeed a complex task. Actually, it is required to solve physiological models (e.g. hemolysis power-law model) and general fluid equations (e.g. Navier-Stokes equations) simultaneously. For hemolysis modeling, specifically, the predicted hemolysis index is directly dependent on the flow field parameters (e.g., stress). Therefore, all the processes of modeling including verification and validation should be conducted for both aspects. In this section, two sorts of governing equations are discussed: conventional hemodynamic equations and physiological hemolysis models.

1.3.1. Hemodynamic Models

In this study, three-dimensional incompressible Reynolds-averaged Navier-Stokes (RANS) equations are used to solve the problem of steady or unsteady turbulent flows inside each test case. The general form of mass and momentum equations for laminar and turbulent flow are similar. The tensorial form of these equations for Newtonian fluid, assuming constant physical properties (such as viscosity and density), are:

Continuity equation:

$$\frac{\partial \rho}{\partial t} + \frac{\partial}{\partial x_j}\left(\rho u_j\right) = 0 \tag{6}$$

Momentum equation:

$$\frac{\partial}{\partial t}(\rho u_i) + \frac{\partial}{\partial x_j}\left(\rho u_j u_i\right) = -\frac{\partial p}{\partial x} + \frac{\partial}{\partial x_j}(\mu \frac{\partial u_i}{\partial x_j}) \tag{7}$$

where ρ, μ, and k_T represent the density, dynamic viscosity, and heat transfer coefficient of the fluid, respectively. If the flow is laminar, these equations can be easily solved using numerical methods. However, in turbulent flow, the computational cost of solving these equations is too high that it becomes almost impossible to solve. In such cases, the time-averaged forms are applied instead as:

Continuity equation:

$$\frac{\partial \bar{\rho}}{\partial t} + \frac{\partial}{\partial x_j}\left(\bar{\rho}\tilde{u}_j\right) = 0 \tag{8}$$

Momentum equation:

$$\frac{\partial}{\partial t}(\bar{\rho}\tilde{u}_i) + \frac{\partial}{\partial x_j}\left(\tilde{u}_i \bar{\rho}\tilde{u}_j\right) = -\frac{\partial \bar{p}}{\partial x} + \frac{\partial}{\partial x_j}\left(\tilde{\mu}\left(\frac{\partial \tilde{u}_i}{\partial x_j} + \frac{\partial \tilde{u}_j}{\partial x_i} - \frac{2}{3}\frac{\partial \tilde{u}_k}{\partial x_k}\delta_{ij}\right)\right) - \frac{\partial \bar{R}_{ij}}{\partial x_j} \tag{9}$$

It should be noted that "$\sim$" and "$-$" represent the density-weighted average and the filtered part, respectively, where for the quantity f: $\tilde{f} = \frac{\overline{\rho f}}{\bar{\rho}}$ and $f = \bar{f} + f'$. Thus, in the flow governing equations, a second-order unknown tensor ($\bar{R}_{ij} = \bar{\rho}\widetilde{u_i'' u_j''}$) is added to the equations. Due to the addition of unknown parameters to the problem and the constant number of equations, the current system of equations is not closed. Therefore, it is necessary to approximate this unknown stress tensor by different methods called turbulence modeling. In this study, k–ω Shear Stress Transport (SST) model has been implemented to simulate the turbulence model in blood pumps. In the k-ω SST model, which was proposed by Menter et al. (1994) [81], Reynolds stresses are related to the velocity gradient using the eddy viscosity hypothesis (Boussinesq) and are calculated as:

$$\widetilde{u_i'' u_j''} = -\nu_t \left(\frac{\partial \tilde{u}_i}{\partial x_j} + \frac{\partial \tilde{u}_j}{\partial x_i} \right) + \frac{2}{3} k \delta_{ij} \tag{10}$$

where ν_t is the Eddy viscosity and is obtained through the formula:

$$\nu_t = \frac{a_1 k}{\max(a_1 \omega, S F_2)} \tag{11}$$

The flow turbulence kinetic energy k and the specific rate of dissipation ω can be calculated through the two differential equations (transport equations):

$$\frac{\partial}{\partial x_j}(\tilde{u}_j k) = \frac{\partial}{\partial x_j}\left[(\nu + \sigma_k \nu_t) \frac{\partial k}{\partial x_j} \right] + \tilde{P}_k - \beta^* k \omega \tag{12}$$

$$\frac{\partial}{\partial x_j}(\tilde{u}_j \omega) = \frac{\partial}{\partial x_j}\left[(\nu + \sigma_k \nu_t) \frac{\partial \omega}{\partial x_j} \right] + \alpha S^2 - \beta \omega^2 + 2(1 - F_1)\sigma_{\omega 2} \frac{1}{\omega} \frac{\partial k}{\partial x_j} \frac{\partial \omega}{\partial x_j} \tag{13}$$

where the blending function F_1 is:

$$F_1 = \tanh\left(\left(\min\left[\max\left(\frac{\sqrt{k}}{\beta^* \omega y}, \frac{500\nu}{y^2 \omega} \right), \frac{4\rho \sigma_{\omega^2} k}{C D_{k\omega} y^2} \right] \right)^4 \right) \tag{14}$$

In the above equation, y is the distance from the wall and F_1 is determined in such a way that it is equal to 1 near the wall ($k - \omega$ model) and 0 away from the wall ($k - \varepsilon$ model). The term S in the turbulence viscosity equation is the strain tensor, and the second blending function F2 is defined as:

$$F_2 = \tanh\left(\left[\max\left(\frac{2\sqrt{k}}{\beta^* \omega y}, \frac{500\nu}{y^2 \omega} \right) \right]^2 \right) \tag{15}$$

It should be noted that the turbulence generation term is limited to ensure turbulence not to be generated in the stagnation area by the production limiter:

$$\tilde{P}_k = -\widetilde{u_i'' u_j''} \frac{\partial \tilde{u}_i}{\partial x_j} \tag{16}$$

where the rate of turbulence kinetic energy production (P_k) is calculated from the formula:

$$\tilde{P}_k = -\widetilde{u_i'' u_j''} \frac{\partial \tilde{u}_i}{\partial x_j} \quad (17)$$

All coefficients of this model are produced by combining $k-\varepsilon$ and $k-\omega$ models considering $\alpha = \alpha_1 F + \alpha_2 (1-F)$. The coefficients of this model are presented in Table 4.

Table 4. Coefficients of k-ω SST Model provided by Menter et al. (1994) [81].

σ_{k1}	σ_{k2}	$\sigma_{\omega 1}$	$\sigma_{\omega 2}$	β^*	β_1	β_2	α_1	α_2
0.85	1.0	0.5	0.856	0.09	3.40	0.0828	5.9	0.44

1.3.2. Hemolysis Model

As mentioned in section 1.2.2, the power-law model introduced by Giersiepen et al. [15] was the first to predict this phenomenon. In the proposed equation (Equation 18), the Hemolysis index H is calculated as a function of flow field stress (τ (Pa)) and exposure time (t (s)).

$$H = C\tau^{\alpha} t^{\beta} \quad (18)$$

Where C, α, and β are empirical dimensionless constants equal to $3.62 \times 10^{-7}, 2.416, and\ 0.785$, respectively. After this first publication, more experimental studies were conducted by other researchers to optimize the constants. Haeuser and Optiz [16] provided new values of constants by applying shear stress to a Couette viscometer for a short time $(C, \alpha, \beta) = (1.8 \times 10^{-6}, 1.991, 0.765)$. In 2011, Zhang et al. [17] repeated the experimental procedure with two novel Couette viscometers. The idea was to perform some tests with two devices that were close to real LVAD systems. Consequently, this group delivered new constants for the power-law model $(C, \alpha, \beta) = (1.228 \times 10^{-7}, 1.9918, 0.6606)$. The most recent study from Ding et al. [18] is the most comprehensive one in this field. The authors suggested that the Hemolysis index obtained in similar conditions is not equal for different species. So, they repeated Zhang's experiment, which was for Ovine's blood, for three other species: Porcine, Human, and Bovine.

Table 5 indicates the details of the power-law model coefficients based on these different experimental studies.

In Giersiepen model, stress (τ) was generally considered as the shear components of the stress tensor. But later it was accepted that it is required to define an equivalent stress to use all the components of the stress tensor in calculations [82]. Moreover, exposure time (t) is the period of time while each particle of RBCs facing specific ranges of stress.

Table 5. Power law model coefficients based on different experimental studies.

References	**Species**	$C(\times 10^{-7})$	α	β
Giersiepen et al. [15]	Human	3.62	2.416	0.785
Heuser and Opitz [16]	Porcine	18.00	1.991	0.765
Zhang et al. [17]	Ovine	1.228	1.9918	0.6606

Ding et al. [18]	Human	0.3458	2.0639	0.2777
Ding et al. [18]	Porcine	67.01	1.098	0.2778
Ding et al. [18]	Bovine	9.772	1.444	0.2076

In the Eulerian approach, the general form of the power-law model is based on a standard transport equation 19:

$$\frac{\partial H_L}{\partial t} + v.\nabla H_L = C^{\frac{1}{\beta}}\tau^{\frac{\alpha}{\beta}} \tag{19}$$

Where $H_L = H^{\frac{1}{\beta}}$. In addition, τ is a scalar parameter that has the unit of equivalent stress. Faghih and Sharp (2019) demonstrated that equation 19 should be used only for uniaxial flows with constant velocities along streamlines [74]. Despite knowing this shortcoming, we have decided to use equation 22 as the equilibrium to calculate Hemolysis. Based on that, the main challenge is to select the equivalent shear stress to be used in the power-law model. More specifically, the question is how to extract a scalar shear stress expression from the stress tensor (Equation 20) to use it in the Hemolysis model.

$$\tau = \begin{bmatrix} \tau_{xx} & \tau_{xy} & \tau_{xz} \\ \tau_{yx} & \tau_{yy} & \tau_{yz} \\ \tau_{zx} & \tau_{zy} & \tau_{zz} \end{bmatrix} \tag{20}$$

Many researchers have proposed different methods for calculating this equivalent stress (Table 6). Most of these methods try to find a maximum value for the stress in different ways. For example, Bludszuweit et al. [82], inspired by the Von Mises model in solid mechanics, proposed equation (21:

$$\tau_b = \left(\frac{1}{2}\left[\left(\tau_{xx} - \tau_{yy}\right)^2 + (\tau_{xx} - \tau_{zz})^2 + \left(\tau_{yy} - \tau_{zz}\right)^2 + 6\left(\tau_{xy}^2 + \tau_{xz}^2 + \tau_{yz}^2\right)\right]\right)^{\frac{1}{2}} \tag{21}$$

However, the usage of this equivalent stress in conjunction with the Power-Law remains questionable [83]. Faghih and Sharp (2016) explained that the Power-Law model was developed for a steady, pure shear flow. Therefore, its application for flows with more than one component of stress is inconsistent with its origin. They proposed another equivalent stress, also derived from the Von Mises stress. They showed that using equation 21, the equivalent stress would be $\tau_b = \sqrt{3}\tau_{xy}$. Therefore, they have modified the Von Mises stress by a factor of $3^{-\frac{1}{2}}$ ($\tau_s = \tau_b/\sqrt{3}$):

$$\tau_s = \left(\frac{1}{3}\left(\tau_{xx}^2 + \tau_{yy}^2 + \tau_{zz}^2 - \tau_{xx}\tau_{yy} - \tau_{xx}\tau_{zz} - \tau_{yy}\tau_{zz}\right) + \left(\tau_{xy}^2 + \tau_{xz}^2 + \tau_{yz}^2\right)\right)^{\frac{1}{2}} \tag{22}$$

Faghih and Sharp also provided another equivalent stress based on the energy dissipation rate [20]. Comparing equations 21 and 22, two differences can be noticed. Firstly, the weight of the normal stress components is different ($\frac{1}{3}$ versus $\frac{1}{2}$). Secondly, equation (23 lacks the normal stress cross products.

$$\tau_e = \left(\frac{1}{2}\left(\tau_{xx}^2 + \tau_{yy}^2 + \tau_{zz}^2\right) + \left(\tau_{xy}^2 + \tau_{xz}^2 + \tau_{yz}^2\right)\right)^{\frac{1}{2}} \quad (23)$$

One of the latest versions of equivalent stress is the one proposed by Faghih and Sharp (2020) [84]. In this paper, the authors try to study the impact of different components of stress on the Hemolysis phenomenon. They applied extensional and shear stresses using two separate test cases. In conclusion, they found that Hemolysis is more dependent on extensional stress components. Consequently, they provided a new expression of the equivalent shear stress, which is based on a new parameter C_n:

$$\tau_n = \left(C_n^2\left(\tau_{xx}^2 + \tau_{yy}^2 + \tau_{zz}^2 - \tau_{xx}\tau_{yy} - \tau_{xx}\tau_{zz} - \tau_{yy}\tau_{zz}\right) + \left(\tau_{xy}^2 + \tau_{xz}^2 + \tau_{yz}^2\right)\right)^{\frac{1}{2}} \quad (24)$$

Where C_n defines the weight of the different types of stresses. Considering the experimental data, $\sqrt{3}C_n = 33.69$ is announced as the optimal value for this parameter. Of course, this value is obtained for human blood, which is different from other species. This issue will be investigated in the present work.

Table 6. Summary table of the proposed expressions for the equivalent stress.

Expression	Reference
$\tau_b = \left(\frac{1}{2}\left[\left(\tau_{xx} - \tau_{yy}\right)^2 + (\tau_{xx} - \tau_{zz})^2 + \left(\tau_{yy} - \tau_{zz}\right)^2 + 6\left(\tau_{xy}^2 + \tau_{xz}^2 + \tau_{yz}^2\right)\right]\right)^{\frac{1}{2}}$	[82]
$\tau_s = \left(\frac{1}{3}\left(\tau_{xx}^2 + \tau_{yy}^2 + \tau_{zz}^2 - \tau_{xx}\tau_{yy} - \tau_{xx}\tau_{zz} - \tau_{yy}\tau_{zz}\right) + \left(\tau_{xy}^2 + \tau_{xz}^2 + \tau_{yz}^2\right)\right)^{\frac{1}{2}}$	[83]
$\tau_e = \left(\frac{1}{2}\left(\tau_{xx}^2 + \tau_{yy}^2 + \tau_{zz}^2\right) + \left(\tau_{xy}^2 + \tau_{xz}^2 + \tau_{yz}^2\right)\right)^{\frac{1}{2}}$	[20]
$\tau_n = \left(C_n^2\left(\tau_{xx}^2 + \tau_{yy}^2 + \tau_{zz}^2 - \tau_{xx}\tau_{yy} - \tau_{xx}\tau_{zz} - \tau_{yy}\tau_{zz}\right) + \left(\tau_{xy}^2 + \tau_{xz}^2 + \tau_{yz}^2\right)\right)^{\frac{1}{2}}$	[84]

By solving equation 19, H values are calculated across the domain. Consequently, The Hemolysis index (HI) of the domain can be calculated using equation 25 [19]. It should be noted that the main hypothesis here is zero Hemolysis at the Inlet.

$$HI = \frac{\sum_{Outlet} H_L^{\beta}\, \dot{m}_{cell}}{\sum_{Outlet} \dot{m}_{cell}} \quad (25)$$

Where, $\dot{m}_{cell}$ is the mass flow rate through each cell's adjacent face to the outlet. To compare the results with the experimental data reported in [85], The MIH (Modified Index of Hemolysis) parameter should be calculated based on equation 26 [86].

$$MIH = HI \times 10^6 \quad (26)$$

In order to quantify the hemolysis phenomena, some parameters are defined to be used both in numerical and experimental tests (Table 7). *HI* represents the ratio of released hemoglobin to total hemoglobin within the RBC ($\Delta fHb/fHb$). To account for variations in the test, the measured *fHb* is normalized by calculating the normalized index of hemolysis (*NIH*). Finally, the modified index of hemolysis
(*MIH*) can be derived from the *NIH* and accounts for the total hemoglobin concentration in the blood ($MIH = NIH \times \frac{10^6}{fHb}$).

Table 7. Definitions of hemolysis parameters being used to quantify the phenomena in numerical and experimental frameworks.

Parameter	Definition	Unit
HI	The ratio of released hemoglobin to total hemoglobin within the RBC	-
NIH	Normalized index of hemolysis	0.765
MIH	Modified Index of hemolysis	0.6606

This thesis investigates the effect of a new expression of the equivalent stress (τ_n in equation 24) on Hemolysis simulation results. For this purpose, simulations were first performed (for the FDA nozzle benchmark, section 2.2) using the three different equivalent stresses τ_s, τ_e, and τ_n, knowing that $\sqrt{3}C_n = 33.69$ was derived from experimental data obtained with human blood. In addition, the impact of C_n on the calculated hemolysis is studied as well for two FDA benchmarks.

1.4. Test Cases

In this work, numerical simulations were performed for three test cases: FDA[4] Nozzle benchmark [87], FDA pump benchmark [88], and FineHeart blood pump [89]. The first two cases are standard benchmarks provided by FDA to evaluate the simulation methodology. While the FineHeart blood pump is a novel LVAD system that is passing the clinical tests at the moment. Figure 11 indicates the order of hemodynamic and hemolysis studies for the three test cases. The FDA benchmarks are implemented to validate and verify the CFD method in predicting hemodynamics and hemolysis. However, the main objective of the thesis is to improve the performance of the FineHeart blood pump in terms of hemolysis. This section provides a comprehensive explanation of each test case, the geometry, testing procedures, and accessible data.

Figure 11. Order of the hemolysis studies in this thesis for the three test cases.

1.4.1. FDA Nozzle Benchmark

The Nozzle benchmark project (Figure 12) was the first part of the evaluation of the CFD tools for simulations of LVADs. Some comparisons with experimental data obtained by various teams, based on PIV[5] measurements, were published in 2011 [87]. Experimental data include velocity and pressure measurements in several cross-sections of the nozzle. This study also established a standard operating procedure and a list of PIV best practices to ensure a certain uniformity in the measurement procedures and the boundary conditions, while reducing PIV measurement errors.

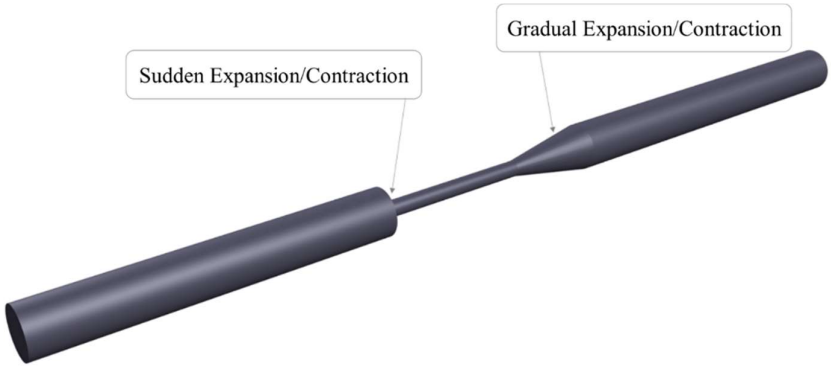

Figure 12. FDA nozzle benchmark geometry and the location of important regions of it.

Several numerical studies were conducted to predict blood flow hemodynamics and hemolysis for the first test case [86,90–94]. Each of them investigated the impact of different methodologies on the

[4] FDA: Food and Drug Administration of the United States
[5] PIV: Particle Image Velocimetry

accuracy and precision of the estimations. For example, Stewart et al. (2012) [91] and Stewart et al. (2013) [92] studied the impact of different RANS turbulent models on the accuracy of the numerical hemodynamic predictions inside the nozzle (see Figure 13). They found that some of the RANS models (e.g., $K-\Omega\,SST$) are significantly accurate in predicting velocity and pressure distribution along the nozzle.

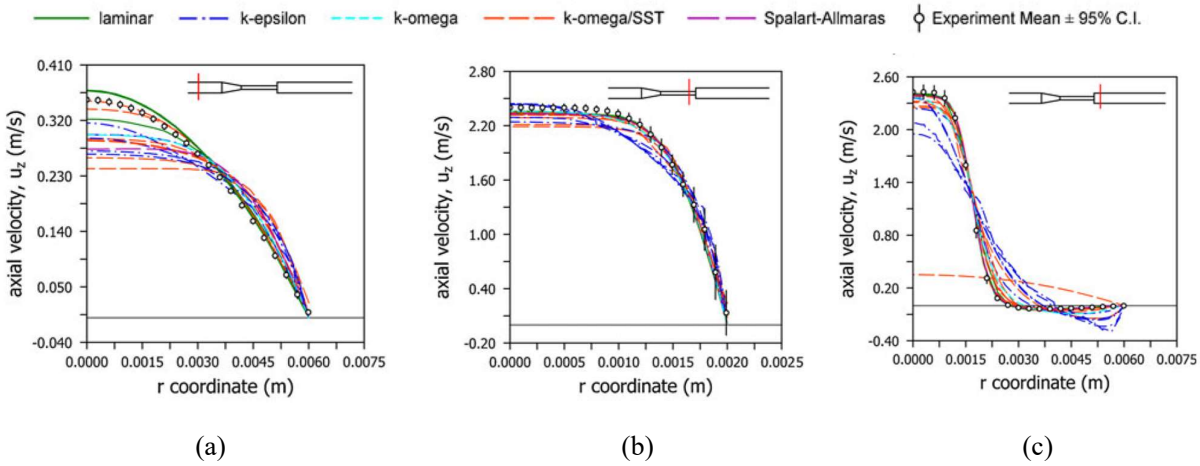

Figure 13. Axial velocity profiles for three cross-sections of the nozzle. Comparison between FDA experimental measurements [87] and CFD predictions with different turbulent models provided by Stewart et al. (2012) [91]: a) z=-0.088m; b) z=-0.008 m; c) z=0.008 m.

The second step of the FDA project was focused on the shear-induced hemolysis in the nozzle [85]. This article investigates the impact of several fluid flow properties and blood properties on this phenomenon. The nozzle model contains regions of sudden and gradual changes in cross-sectional area, similar to many actual blood-contacting medical devices. The maximum and minimum diameters of this model are 12 mm and 4 mm, respectively. Other geometrical specifications of this test case are shown in Figure 14.

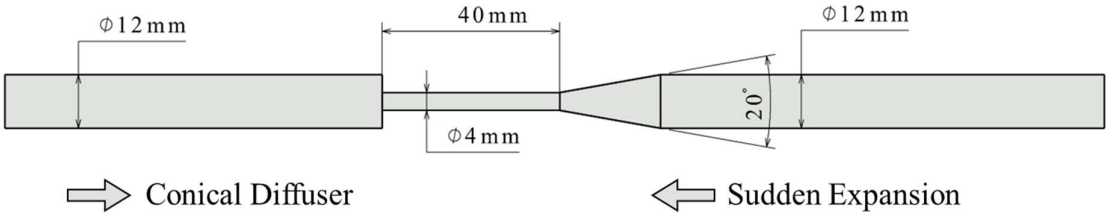

Figure 14. FDA nozzle model and two opposite configurations of it: Conical Diffuser and Sudden Expansion [87].

The nozzle was positioned with both the flow coming from left to right and from right to left, to test the two following configurations: a) Sudden Expansion (SE). b) Conical Diffuser (CD). (see Figure 14). These two configurations represent some critical regions that exist inside artificial cardiovascular devices. Three independent laboratories performed a total of 36 tests for configuration (a) and 27 for (b). Authors have reported that these amounts of tests were sufficient to ensure experimental repeatability and also neglect the effect of blood aging between successive days of a test [87]. Figure 15

demonstrates a schematic of the FDA's recirculating test loop. As shown, a centrifugal pump is used to ensure the blood flow circulation inside the test loop. In addition, a heat exchanger system is employed to impose a constant temperature during the tests.

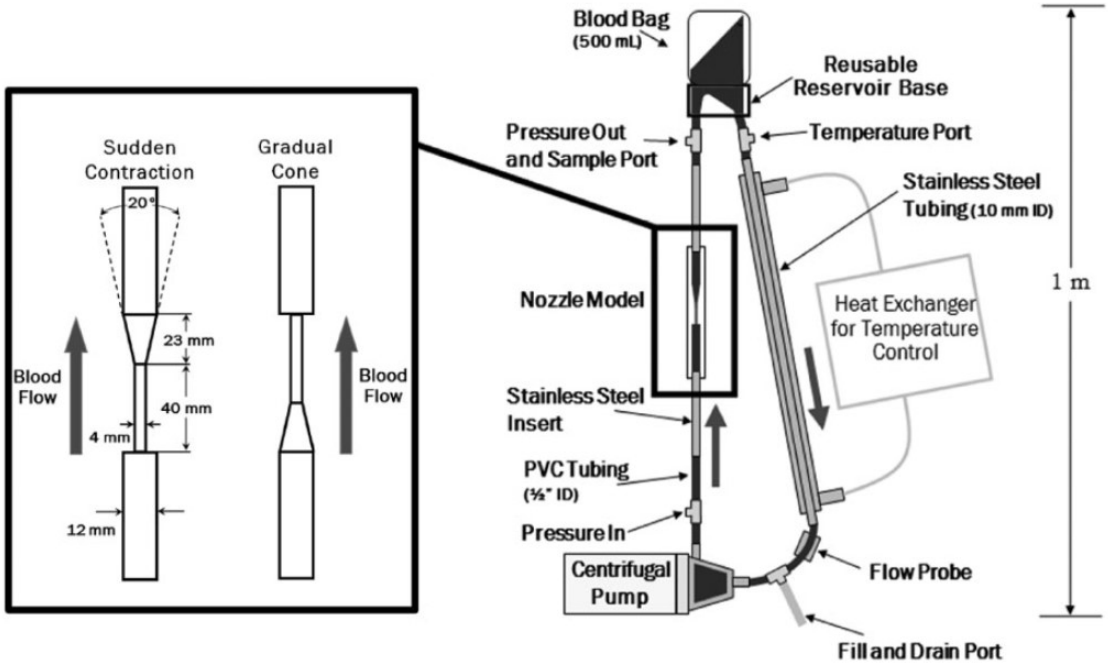

Figure 15. Schematic of the FDA nozzle recirculating blood damage test loop [85].

In addition, blood from two different animals was used in the experiments: Bovine and Porcine. To avoid any influence of the blood properties on the tests, they were adjusted using specific biological equipment (see Table 8).

Table 8. Blood properties that have been used for FDA Nozzle Hemodynamic and Hemolysis tests [85,87].

Condition		**Experiment Values**		**CFD Values**	
Test Objective	Material	Density ($\frac{g}{mL}$)	Viscosity (cP)	Density ($\frac{g}{mL}$)	Viscosity (cP)
Hemodynamic	Sodium iodide [85]	$1.68 - 1.72$	6.74 - 7.60	1.7	7
Hemolysis	Bovine blood [87]	1.04 ± 0.01	4.21 ± 0.32	1.04	4.2

One of the objectives of this paper was to generate some data to validate CFD-based predictions of hemolysis. Actually, the FDA nozzle was the first accessible hemolysis benchmark that was investigated through several papers [86,95,96]. For instance, Tobin and Manning (2020) [86] used the nozzle test case to propose a novel analytical and numerical framework for the simulation of flow-induced hemolysis based on the LES turbulent modeling. To implement such a turbulent model, they generated a 3D grid with 6.7 million cells. Firstly, they demonstrated that how the LES turbulent models are

applicable to predict velocity and stress profiles inside the nozzle. In the second step, they tried to tune the hemolysis models with the nozzle benchmark. By comparing numerical and experimental data (see Figure 16), they proposed a new set for the power-law coefficients which is different from what was found by experimental measurements [15–18]: $(C, \alpha, \beta) = (2.7 \times 10^{-9}, 2.5, 0.264)$.

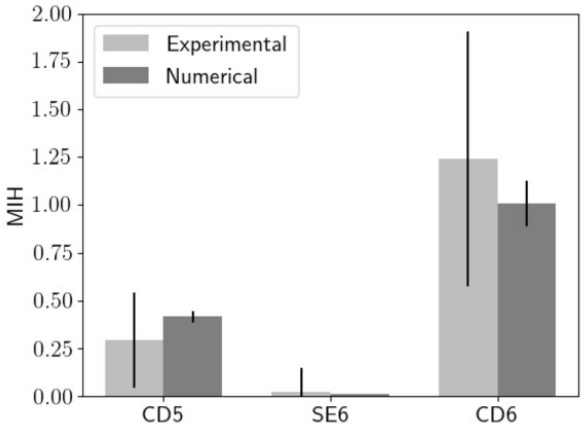

Figure 16. FDA Experimental against CFD-predicted MIH values with $(C, \alpha, \beta) = (2.7 \times 10^{-9}, 2.5, 0.264)$ provided by Tobin and Manning (2020) [86] for different configurations of the test: CD5: Conical diffuser with 5 lpm of flow rate. CD6: Conical diffuser with 6 lpm. SE6) Sudden expansion with 6 lpm.

In this work, the FDA nozzle benchmark was used as a primary test case to evaluate the CFD simulation methodology. Details of numerical modeling and results of this model have been reported in section 2.2.

1.4.2. FDA Pump Benchmark

The FDA's second benchmark is a centrifugal blood pump with four simple radial blades [88] (Figure 17). This test case aimed to conduct hemolysis analysis in a more realistic geometry, considering conventional blood pumps. Before the experimental results were published, the FDA project asked researchers to provide their calculated hemolysis index over specific operating conditions. By comparing the results, they found meaningful discrepancies between numerical and experimental outputs [88]. In addition, differences between the numerical results themselves cast doubt on using these methods to predict the absolute value of the hemolysis index. They deduced that numerical simulations are not significantly reliable in quantitative hemolysis outcomes. Nevertheless, the FDA project noted that these methods could be implemented as a comparison tool [88].

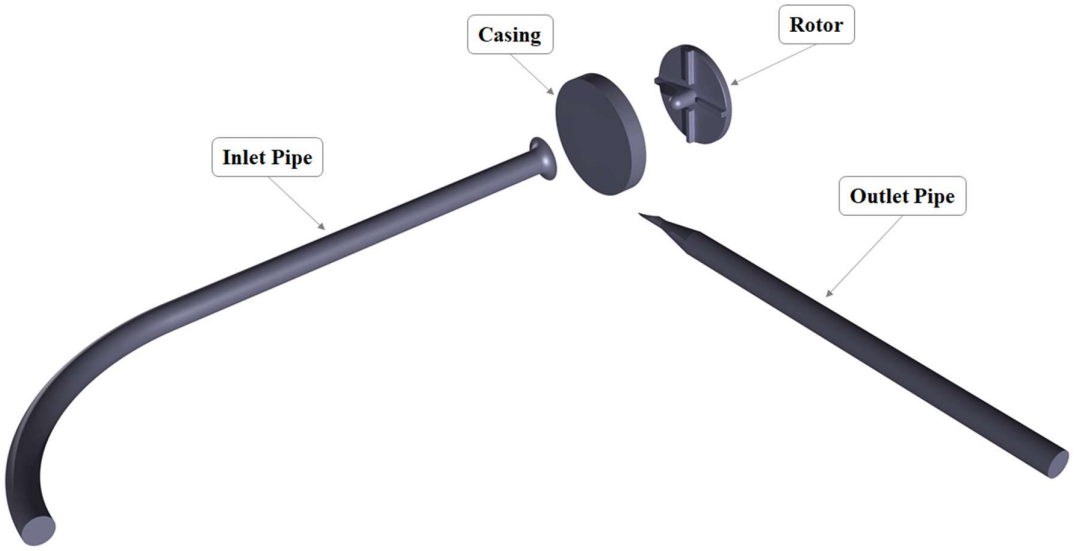

Figure 17. FDA Pump benchmark's components provided by Malinuskas et al. (2017) [88].

The FDA pump benchmark consists of an impeller with four simple radial blades, a housing, an inlet pipe, and an outlet pipe (Figure 18 and Figure 19). Figure 18 indicates an external view with the dimensioning of this test case. As it shows, blood flow enters the impeller domain after a 90-degree blended inlet pipe with an inner diameter of 120 mm. Inside the impeller, the flow is pressurized due to the blade's rotational speed. Then it exits to the outlet pipe, which starts with a conical diffuser. The outlet pipe finally expands to a straight pipe with an inner diameter of 12 mm.

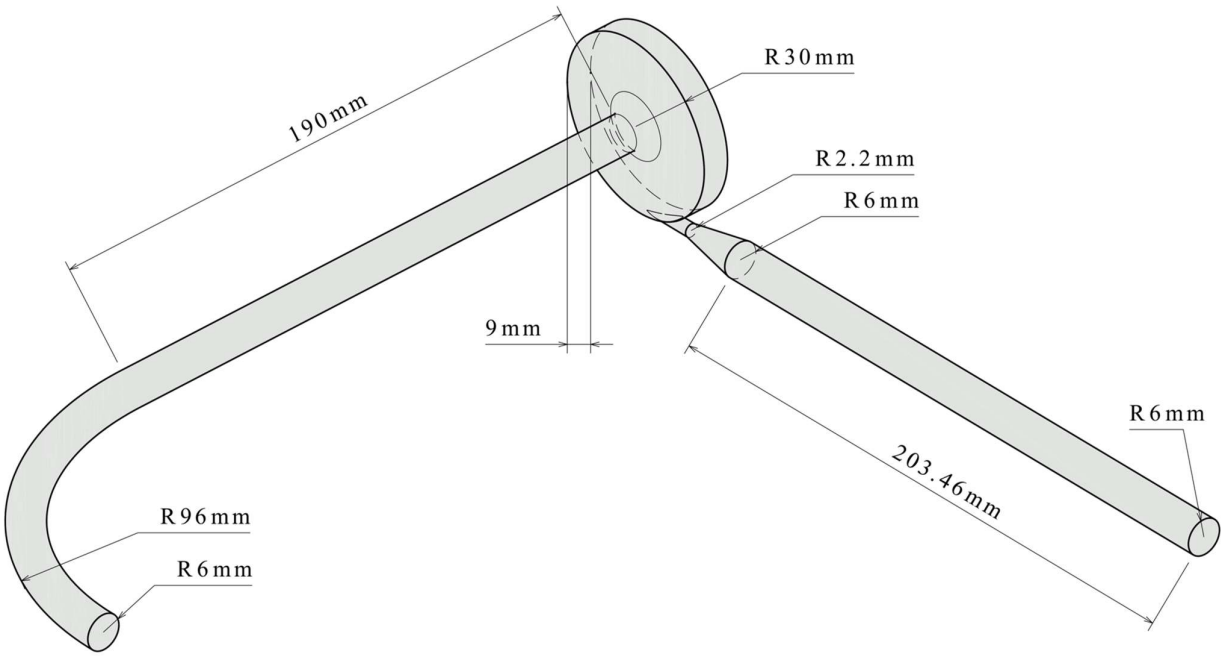

Figure 18 Dimensioning of the FDA pump benchmark: casing, inlet pipe, and outlet pipe [88].

Figure 19 demonstrates the dimensioning for the rotor of the FDA pump. As mentioned, the impeller consists of four radial blades. The thickness, height, and length of these blades are 3, 3, and 18.5 mm,

respectively. They have been installed on a cylindrical rotor with a diameter of 52 mm and a thickness of 4 mm. To our knowledge, the size of the FDA pump benchmark is bigger than all conventional blood pumps.

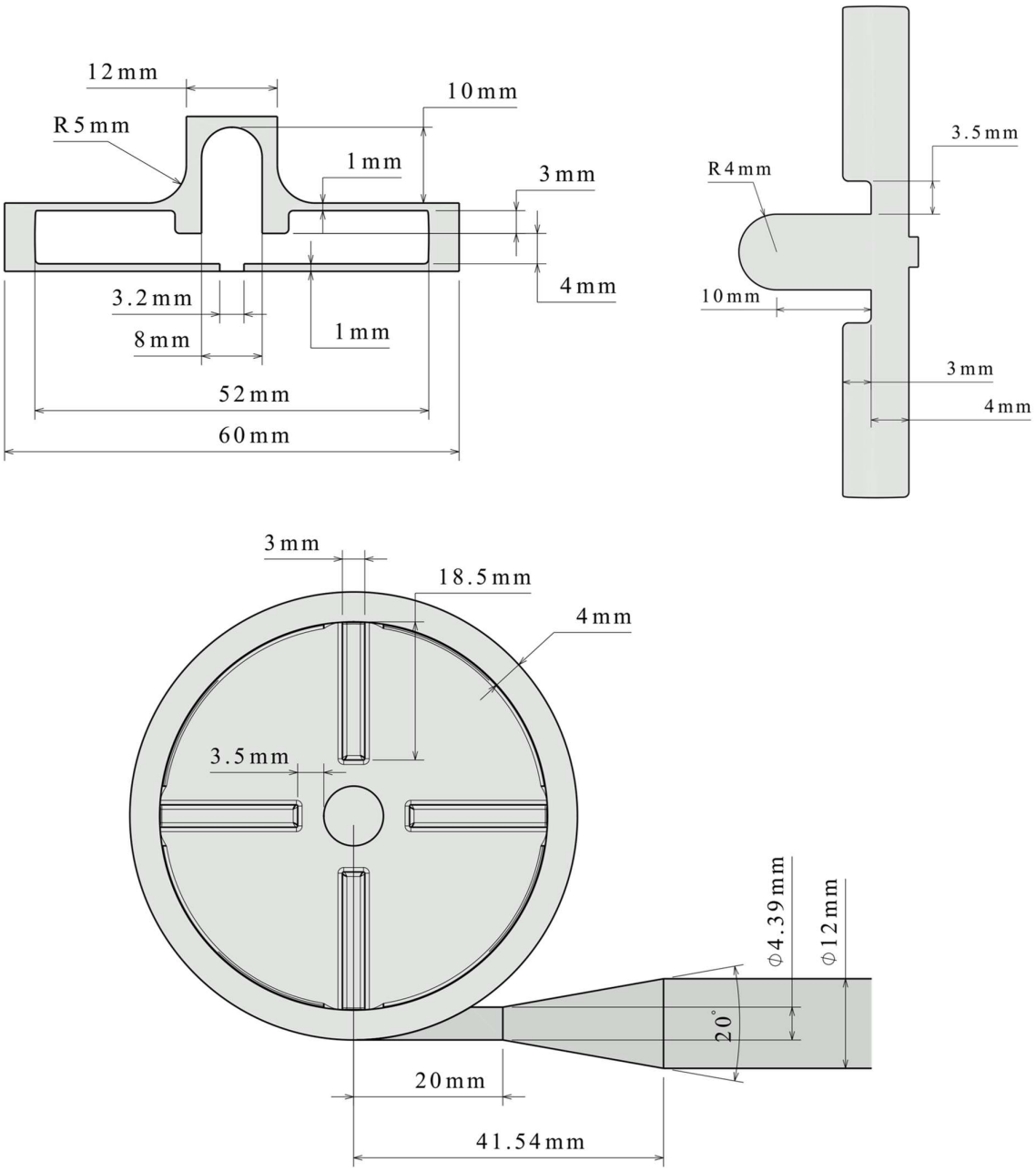

Figure 19 Dimensioning of the rotor of the FDA pump benchmark model [88].

Similar to the nozzle benchmark, the FDA team conducted this project with two separate testing strategies. In the first step, fluid flow's hemodynamics were analyzed through PIV tools. Measurements were carried out for six operating conditions (see Figure 20). Secondly, hemolysis tests were done with porcine blood in the same configurations of the flow. In the following, a brief explanation of each test bench is explained.

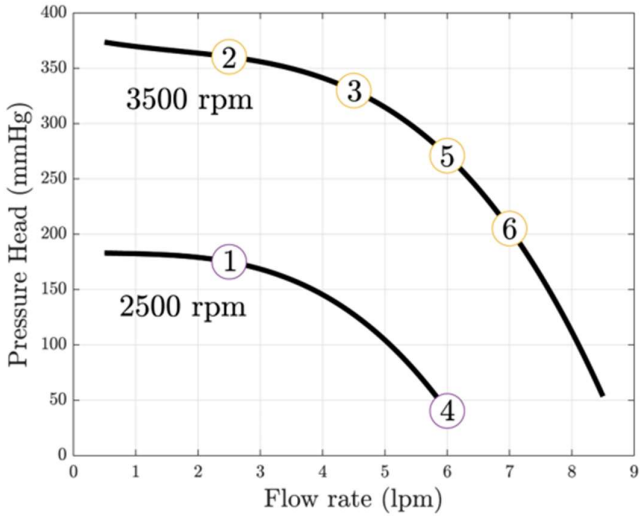

Figure 20. In the FDA pump project, hemodynamic and hemolysis measurements were conducted for six operating conditions [88].

- Particle image velocimetry within three laboratories: the objective of this test was to measure the velocity components inside the pump. A Newtonian fluid composed of 50–53% saturated aqueous sodium iodide solution, 16–17% glycerin, and 31–33% water, by weight, was used to represent the hemodynamic behavior of the blood. The time-averaged 2D velocity field was obtained by averaging the cross-correlation results of 500–2500 pairs of images captured at the same rotor position (with a perpendicular position of one of the blades to the outlet pipe). Figure 21 shows a contour of PIV two-dimensional velocity magnitude in a cross-sectional plane located 1.2mm from the top surface of the impeller blades [88].

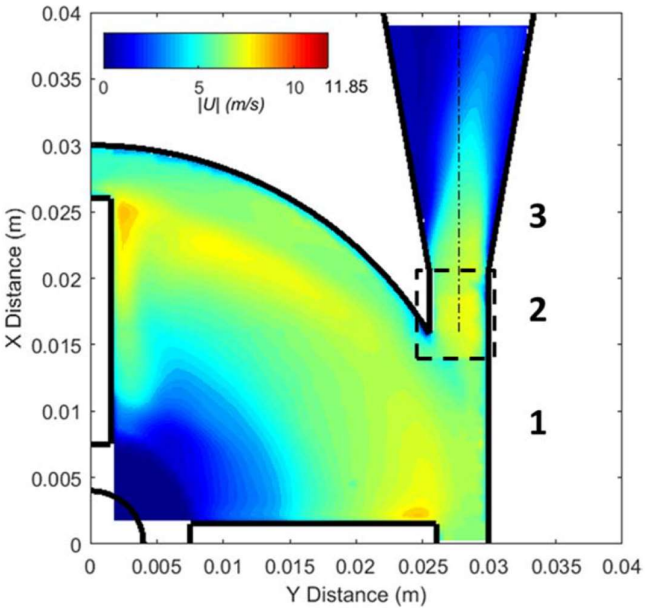

Figure 21. A sample contour of PIV two-dimensional velocity magnitude on a cross-section upper-blade plane within the pump for a specific operating condition of the pump (n=3500 rpm and Q=6 lpm) [88].

- Hemolysis tests with the porcine's blood in one laboratory: the objective of the second test was to quantify the hemolysis in the pump within each operating condition. Figure 22-a indicates a schematic of the test loop. The hemolysis test loop contains the following components: FDA blood pump model, flow probe, pressure (P) transducer, clamp to control the backpressure, blood temperature thermistor, tank, heat exchanger to adjust a constant temperature at 25°C, and pre-pump pressure and blood sampling port. Eight separate porcine blood pools were used to conduct sixteen replicates for the blood pump model. Each experiment has been performed for a total of 120 minutes, and samples were drawn every 40 minutes. Figure 22-b demonstrates the measurement of free hemoglobin variations for each of the operating points [88]. A meaningful uncertainty range can be observed in the results, which is one of the challenging points in the numerical modeling of hemolysis.

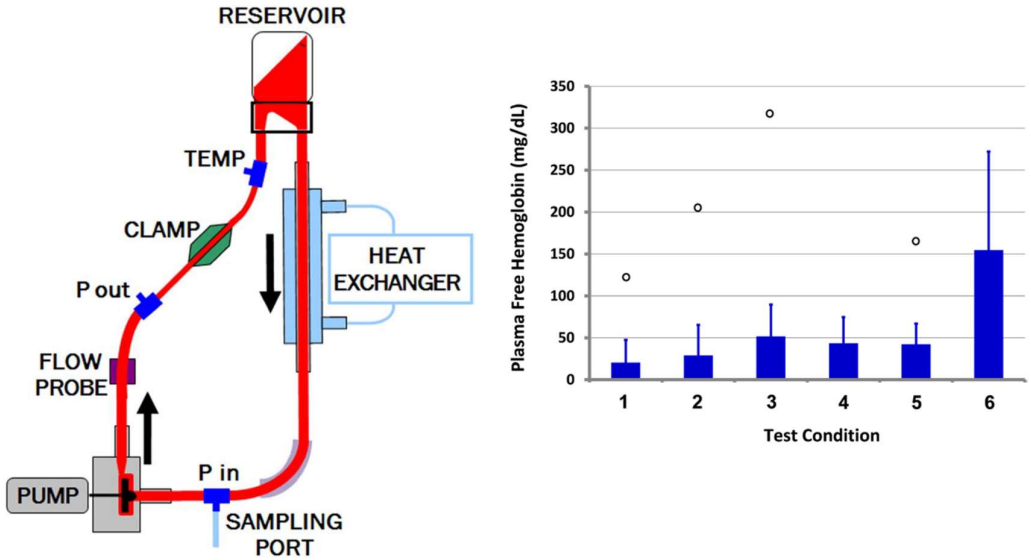

(a) (b)

Figure 22. a) Schematic of the hemolysis test loop. b) In vitro hemolysis results for the blood pump model at the six operating points [88].

1.4.3. FineHeart Blood Pump (ICOMS)

FineHeart Blood pump is a new type of propelling cardiac pump that ejects blood during the systolic phase [89]. The pump has been named Implantable Cardiac Output Management System (ICOMS). This original type of pump (ICOMS, FineHeart®, Pessac, FR) is inserted into the left ventricular apex (see Figure 23). The pump and its casing are equipped with a membrane connected to the wall of the heart. The ICOMS outlet is adjusted in a way as to lead discharge blood flow through the aortic valve toward the aorta. However, the pump outlet remains under the aortic valve and then strictly inside the left ventricle. In addition, a standard pacemaker lead (red cable in Figure 23) is connected to the controller, which imposes the pump to be synchronized with the native ejection and filling phases of the ventricle. The main goal is to preserve the physiological heart function and adjust the pump's rotational speed

according to the native ejected blood volume assessed by echocardiography (periodical measurements ensured by the physician). Accordingly, the ICOMS can run in continuous mode, similar to conventional blood pumps, or a pulsatile synchronous mode, respecting the ventricular contractility status assessed by the physician.

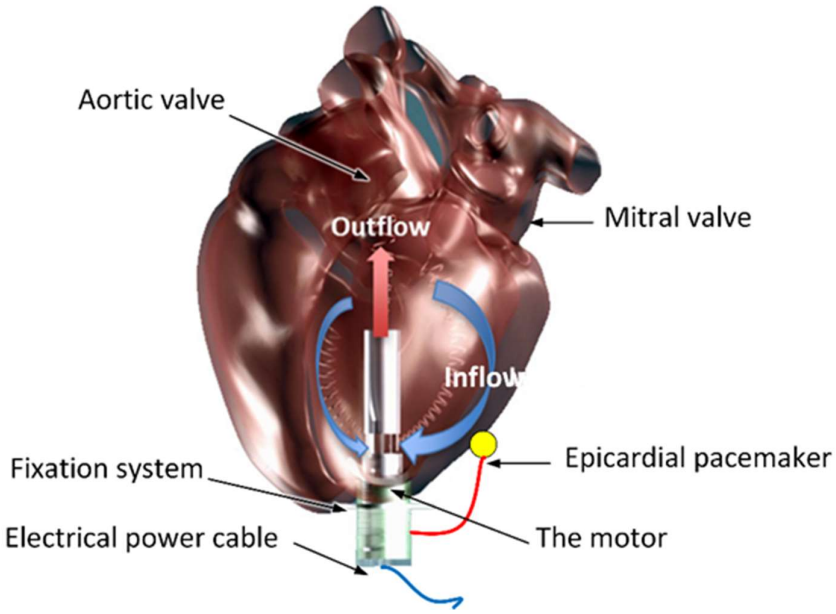

Figure 23. Positioning of the FineHeart blood pump (ICOMS) inside the left ventricle.

Figure 23 indicates how the ICOMS would be implanted within the left ventricle using a specifically designed fixation system. The inlet is located within the apical left ventricular area, while the outlet is located 1 cm under the aortic valve (the distance can be manually adjusted during the surgical procedure). A pacemaker lead is screwed to the epicardial tissue and connected to the motor. Just before ventricular contraction, the tissue is electrically activated, which is sensed by the pacemaker lead. The delay between the electrical activation and contraction is calculated via common trans-thoracic echocardiography, and the value is entered into the ICOMS programming system via telemetry. Once the systolic phase is well identified, the pump rotational speed increases up to a high rotational speed during the isovolumic contraction phase (adjustable parameter depending on the patient's need). The ejection time duration has also been calculated by echocardiography and the value entered into the program; the blood is drawn up via the inlet and ejected through the outlet and through the spontaneously opened aortic valve. The end of this period corresponds to the aortic valve closure; the filling period can start while the pump rotational speed decreases down to diastolic low speed during the relaxation phase (adjustable by the physician) with no blood ejection through the aortic valve. The pump functioning thus remains physiological since both ventricular filling and ejection are respected (see Figure 24).

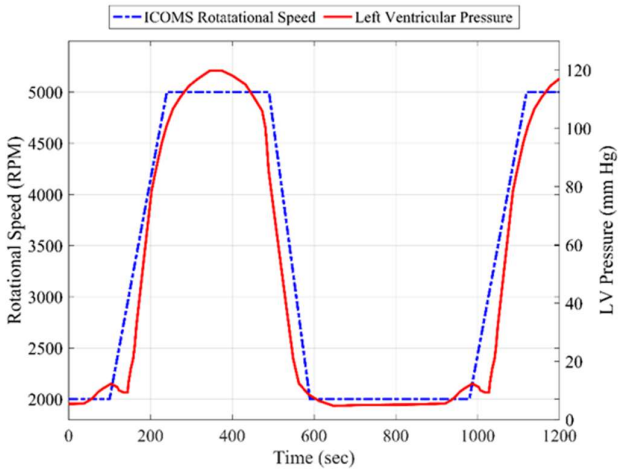

Figure 24. The ICOMS rotational speed and the left ventricle pressure versus time for one cycle of systole and diastole.

Figure 25 shows the different components of the ICOMS blood pump. The ICOMS consists of six main parts; a magnetic motor, which provides the required energy; the main impeller, an inducer, a diffuser, a straightener, and a coupling part which ensures a good connection between the magnetic motor and rotating parts. The role of the inducer is to reduce blood turbulences and make the flow more laminar while entering the impeller. This function results in a more efficient way of transforming energy in the impeller. The impeller has to increase blood kinetic energy, which is the pump's main goal. The impeller substantially accelerates the speed flow up to 3 m/sec. Then, the diffuser transforms an important part of the flow kinetic energy into potential energy (pressure) by reducing the flow speed (down to 1.2 - 2.0 m/sec, depending on the rotational speed). Finally, there is a straightener that focuses the blood flow jet and ejects blood through the aortic valve 1 cm underneath. The presence of this component is essential because it prevents turbulences and vortices just above the pump outlet.

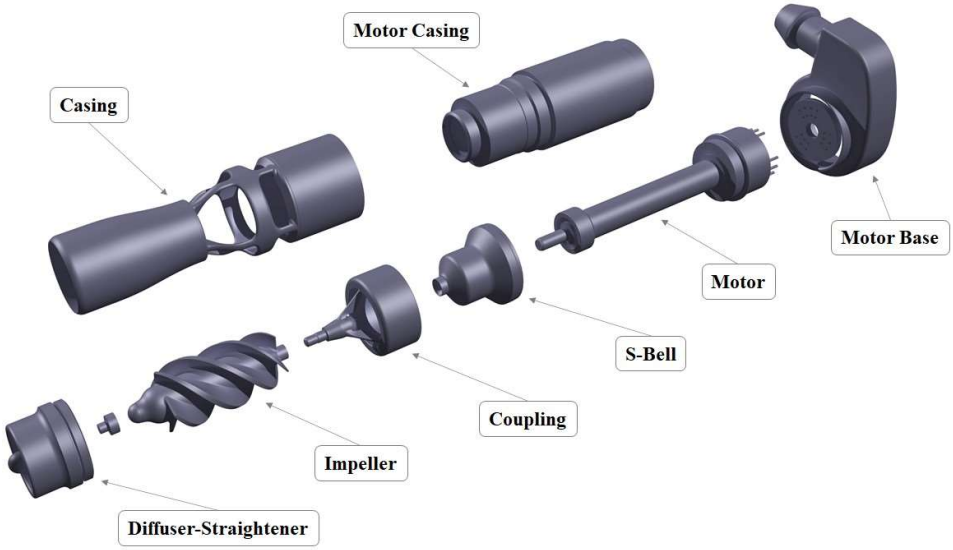

Figure 25. Different components of the ICOMS blood pump.

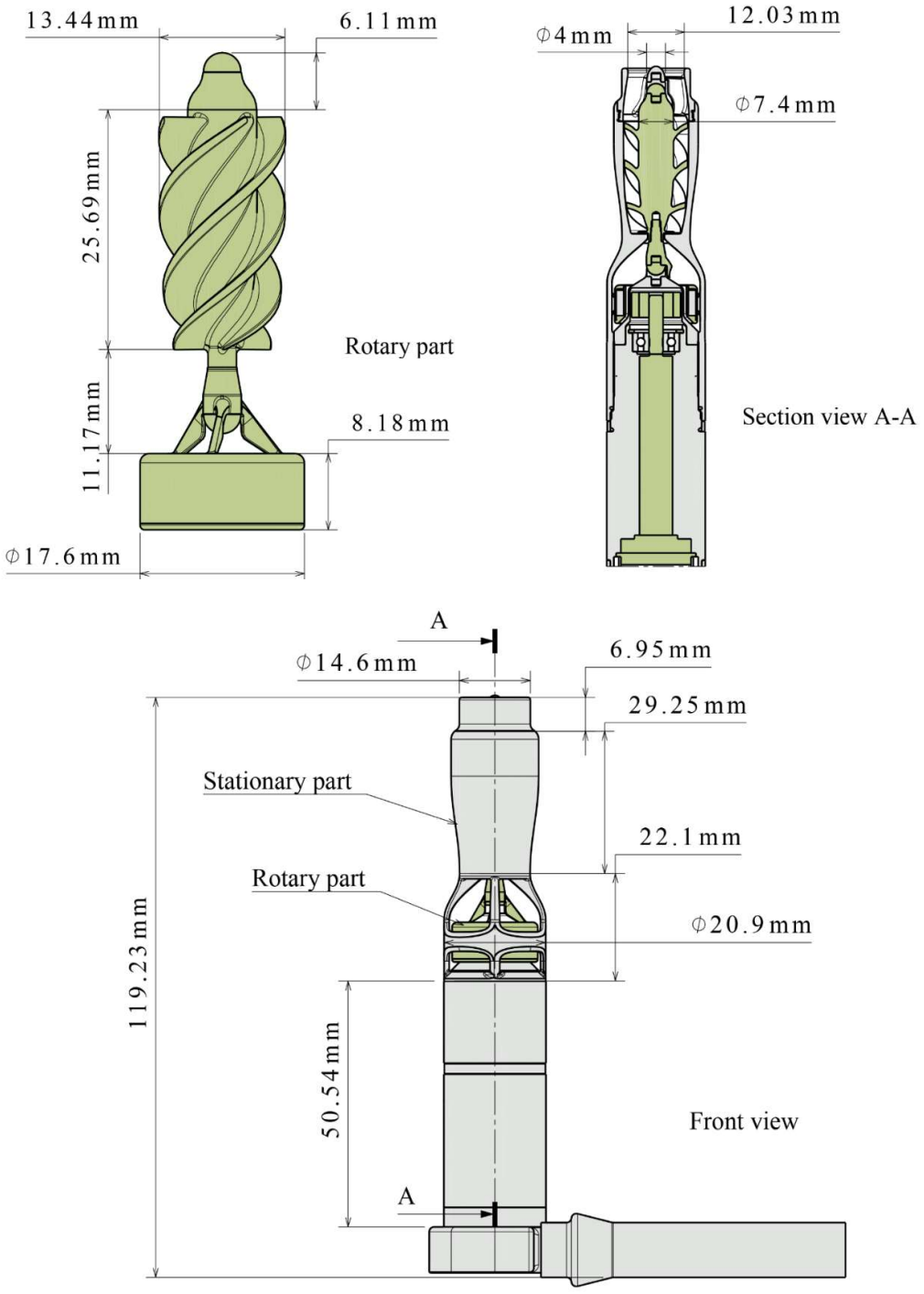

Figure 26. Dimensioning of the rotor of the FineHeart blood pump.

Thanks to FineHeart's collaboration we have had access to all the needed information from experiments. Three sets of data exist that could be used to validate CFD computations in terms of hemodynamic and hemolysis of the ICOMS: a) Correlation loop (characteristic curves). b) PIV measurements. c) Hemolysis tests. The correlation loop setup was used to validate the hemodynamics of the flow inside and outside of the ICOMS. Figure 27-a indicates the correlation loop testing schematic

that has been developed to obtain characteristic curves of the pump. The setup consists of different components: a heating tank that provides the liquid with the desired temperature ($37\,^{o}C$) and a solid box that includes the ICOMS pump (Figure 27-b). Two pressure (OMEGA CO UK, model: PXM319-0.35G10V) sensors and a Flowmeter (IFM Electronic, model: SM6000) quantify the flow properties at the inlet and outlet of the box. In addition, a computer-based system controls the rotational speed of the pump (MAXON, model: ESCOM Module 50/5). The ICOMS pump power is provided by a Maxon driver (model: ECXSP16LBLKLASTEC 48V). Tests were carried out for a liquid that is composed of 62% demineralized water and 38% of glycerol to reproduce the degree of blood viscosity. FineHeart provided experimental data of this setup for a wide range of flow rates (0.5 to 7 lpm) and rotational speeds (1000 to 7000 rpm).

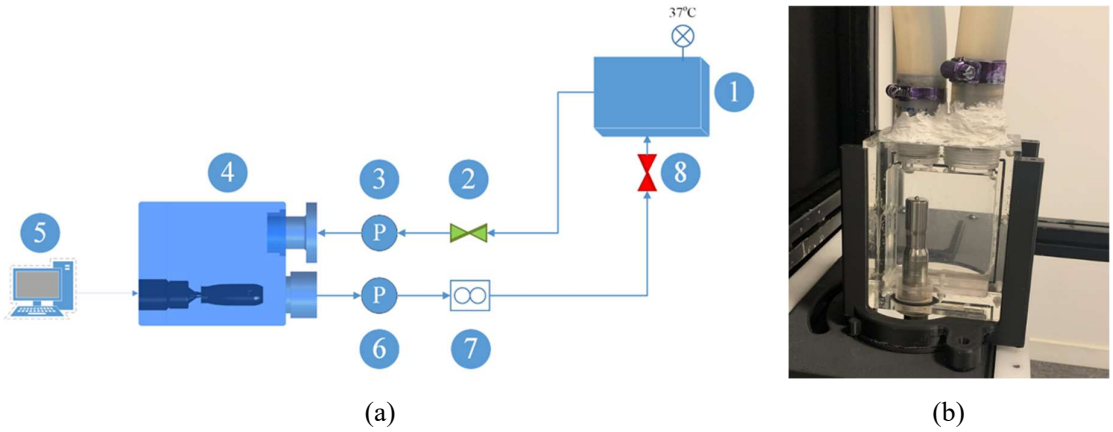

(a) (b)

Figure 27. a) Flow measurement setup to obtain performance curves of the ICOMS. 1. Heating reservoir. 2. Gate valve for security. 3. Pressure sensor at the inlet of the box. 4. Box. 5. Control system. 6. Pressure sensor at the outlet of the box. 7. Flowmeter. b) the ICOMS positioning inside the testing box.

Moreover, PIV measurements have been conducted to quantify the flow pattern as the pump operates inside the same testing chamber (Figure 27-b). The objective of this test rig is to mimic the functionality of the ICOMS within the left ventricle, knowing that there are several discrepancies between the left ventricle (LV) condition and the testing box. The loop is filled with water and reflective particles and the pump is positioned vertically at 12 mm of the outlet of the plexiglass box (Figure 28), respecting its usual direction in the heart (see Figure 23). Figure 29 demonstrates the PIV test set up which consists of different components: 1. DANTEC 2. CAMERA 3. The ICOMS adjusted inside the testing chamber 4. The Control system. The flow loop is connected through pipes to a tank above the box. The difference between the water level of the tank and the inlet of the box is 80 cm. This ensures a static pressure of 60 mm Hg at the inlet, considering the pressure condition in the left ventricle.

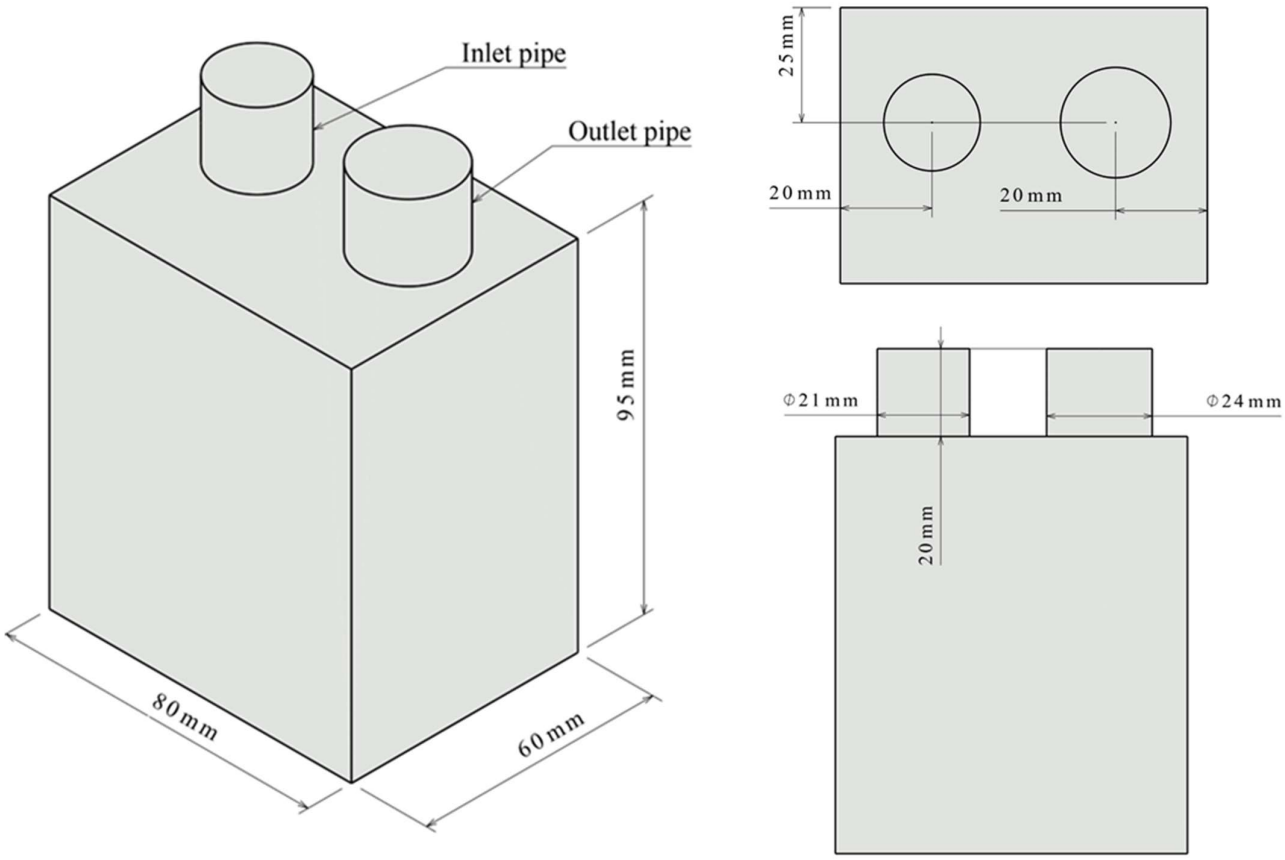

Figure 28. Dimensions of the PIV testing chamber.

(a) (b)

Figure 29. PIV test setup contains 1. DANTEC 2. CAMERA 3. The ICOMS adjusted inside the testing chamber 4. The Control system.

FineHeart also provided hemolysis test data of the ICOMS. The hemolysis tests were conducted in consideration of the ASTM F1841-19E1 standard practice for assessment of hemolysis in continuous flow blood pumps. The ICOMS were tested in the mock circulation loop (see Figure 30) using porcine blood. The FineHeart hemolysis test setup consists of the ICOMS, blood reservoir (Huenersdorff GmbH, DE, model: Reservoir 10L Wide-Mouth Jerrycan), rigid test chamber, flow meter (Transonic Systems Inc. US, model: TS410), pressure sensors (CODAN PVB Critical Care GmbH, DE, model: PVB DPT-

6100), sampling port, tubing, and connectors. The temperature was measured by a thermocouple (National Instruments Corporation, US, model: NI-9212) probe located in the blood reservoir and was maintained by a water bath. The temperature of the water bath was regulated to ensure a constant temperature of the blood flow using a heating unit (CHAL-TECH GmbH, DE, model: Quickstick SVD3). Over the testing duration, the plasma hemoglobin concentration (PFH), platelet count (PLT), and white blood cell (WBC) count were recorded using a specific hematology analyzer tool (IDEXX Laboratories, Inc., US, model: Procyte DX).

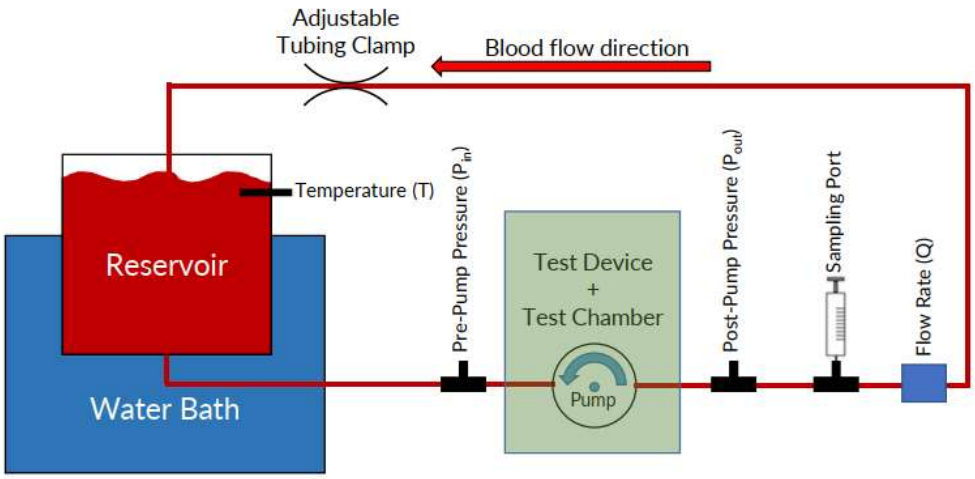

Figure 30. Schematic of the hemolysis test conducted by FineHeart.

1.5. Objectives of the Work

In section 1.1, the importance and application of ventricular assist devices in the recovery of cardiac patients were explained. In addition, the use of numerical methods in optimizing these devices, both in terms of hemodynamics and hemolysis, was investigated. It was mentioned that due to the uncertainties in the hemolysis phenomenon, no accurate numerical model has been found for it so far.

In this thesis, a new methodology has been used to simulate the hemolysis phenomenon. This model was first presented by Faghih and Sharp (2020) [84] based on experimental measurements, and in that extensional stresses are considered the primary source of the phenomenon. The main objective of this work is to evaluate the new expression using the numerical tool within different geometries. Three test cases are considered to examine the method: FDA nozzle benchmark [87], FDA pump benchmark [88], and FineHeart blood pump. Simulations were planned and carried out for three models in order (Figure 31). For the first two cases, standard models provided by FDA, the objective is to validate the numerical methodology. While for a more realistic test case, the FineHeart blood pump, the final goal is to provide some advice to reduce the hemolysis index.

In this regard, the objectives of the thesis can be stated in the following format:

- Validation of the conventional RANS models to simulate the hemodynamics of the blood flow in medical devices
- Evaluation of a novel methodology to simulate the hemolysis phenomenon in blood-contacting devices
- Parametric study of the weighting coefficient in the new method between normal stresses and shear ones
- Comparison between hemolysis index in humans and animals for the same operating conditions of devices
- Providing solutions to reduce the hemolysis index in FineHeart pump

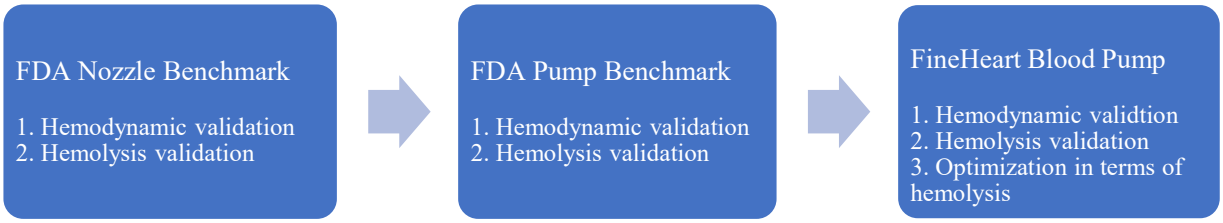

Figure 31. Three test cases in this thesis, as well as the order of simulations.

Last but not least, an advanced simulation methodology for the hemolysis phenomenon, which could be probably validated by competent institutions like the FDA, would help us to decrease the number of sacrificed animals for the R&D phase of the next generations of blood pumps.

2. Numerical Modeling

In this research, numerical modeling is used as a fundamental tool in predicting the phenomenon of hemolysis. As with any other research tool, applying computational methods requires a scientific and integrated approach. The unprincipled application of this method leads to unrealistic results. In this section, the full details of the numerical modeling of the hemolysis phenomenon in the three studied cases are discussed separately. For each case, the geometry generation process and computational grid are discussed. In addition, the details of the numerical method used and the related settings of the solver are described.

This section also includes the results of each model, along with an interpretation of the obtained results. To begin with, the accuracy and precision of the simulation results are evaluated and validated from a hemodynamic perspective, by comparing them with experimental measurements. The next step involves a similar process for the hemolysis parameters, where the accuracy of different hemolysis simulation methods is compared. Finally, specific conclusions are drawn for each case that was studied.

The approach to analyzing the results differs for the FineHeart blood pump when compared to the two FDA benchmarks. The objective of examining the results for the two FDA benchmarks is to validate the numerical methodology used in predicting hemolysis. On the other hand, the primary goal of studying the ICOMS is to investigate the local sources of hemolysis production. However, this requires initial validation of the methods through experimental measurements.

2.1. Software and Hardware

In this thesis, different software have been used to conduct each step of the simulations including geometry preparation, grid generation, CFD solving, and post-processing (Figure 32). Generally, Ansys software v2020 R2 (ANSYS, Inc., Canonsburg, PA) was implemented as the main platform of the work.

Firstly, the geometry of each test case was created using Ansys SpaceClaim or Catia. In the next step, grids were generated using Ansys ICEM, Ansys Meshing, or Ansys Turbogrid. Each of these Ansys modules can generate meshes for a specific type of geometry. For example, Ansys Turbogrid is a meshing module specialized in turbomachinery geometries (e.g., pumps, fans, and turbines). It can provide high-quality structured grids for such cases, but for the other types of geometries, it is useless.

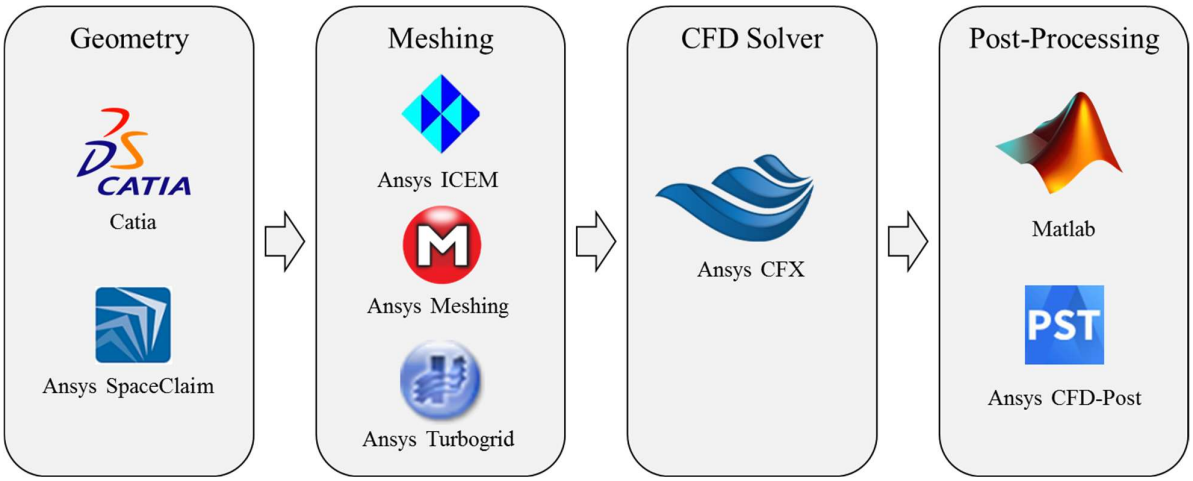

Figure 32. For each step of the numerical simulation, a specific software has been used.

Finally, numerical simulations have been carried out using the ANSYS CFX. This code is reportedly robust to estimate the behavior of complex flows in rotating devices [97,98]. CFX is a node-oriented solver (storing information in network nodes) which is based on the finite volume method [99]. This solver uses a fully-coupled algorithm to solve the flow equations on a co-located network simultaneously. In discrete solution strategies (such as the SIMPLE algorithm), momentum equations are calculated based on a guess for the solved pressure field and velocity components. Next, using the resulting velocity field, the pressure is corrected and the cycle is repeated. The nature of guesswork and correction in such algorithms makes them requires many iterations to reach a suitable output. This is while in the coupled algorithm, all equations are discretized in a fully implicit way and are solved in the form of a single equation system. As a result, the relationship between the pressure field and the flow velocity is established directly and it is expected that the convergence will be achieved in fewer iterations.

Considering the nature of the simulations, in which two sets of equations are solved at the same time, we had to use high-performance computations. For the FDA nozzle benchmark and FineHeart blood pump, calculations were performed in parallel processing on a computer with 32 computing cores (AMD Ryzen™ Threadripper™ 1950WX) with a processing frequency of 3.6 GHz and a temporary memory of 36 GB. While for the FDA pump benchmark, the ARC supercomputer facilities were implemented with the capacity of 1024 computing cores. Of course, we have only used 32 cores out of it. Simulation

time varied between several hours (for the nozzle) and several days (for the FineHeart pump). Detailed specifications regarding the simulation facilities and calculation times are provided in Table 9.

Table 9. Detailed specifications regarding the simulation facilities and calculation times for each test case.

Test Case	Simulation Type	Number of processors	Equipment source	Calculation time (hrs.)
FDA Nozzle Benchmark	Hemodynamic	32	Medrik DT (AMD Ryzen™ Threadripper™ 1950WX)	4
	Hemolysis	32		12
FDA Pump Benchmark	Hemodynamic	64	ARC (x16 nodes of Intel Xeon Platinum 9242)	48
	Hemolysis	64		220
FineHeart Blood Pump	Hemodynamic (Correlation loop)	32	Medrik DT (AMD Ryzen™ Threadripper™ 1950WX)	7
	Hemodynamic (PIV)	32		70
	Hemolysis	32		450

2.2. FDA Nozzle Benchmark

As mentioned in section 1.4.1, the nozzle benchmark was the first test case provided by the FDA in 2011 to evaluate the use of numerical simulation in developing LVADs. The simple geometry of this model makes its simulation process more straightforward. For example, due to the cylindrical geometry of the nozzle, it is possible to use a structured meshing strategy. In this section, the numerical methodology, the grid generation process, and simulation results for the FDA nozzle model are presented.

2.2.1. Methodology

To simulate hemodynamic aspects of the FDA nozzle benchmark in steady state form, the three-dimensional Reynolds-Averaged Navier-Stokes (RANS) equations are solved in conjunction with the k-ε, the k-ω, or the k-ω SST turbulence models in isothermal condition. In addition, the second order of approximations is used for the discretization of the nonlinear convection terms in all transport equations. As stated in section 1.1.1, the approximation of blood in large arteries as a homogeneous Newtonian fluid is a common assumption [100], which is applied to the present study. So, the dynamic viscosity and density have been set to constant values consistent with the experimental conditions (see Table 8). For the hemodynamic and hemolysis simulations, Sodium iodide and Bovine's blood properties were applied as material properties in the solver.

In addition, the convergence criteria are specified as RMS residuals of 10^{-6}. It has been observed that the residuals of all equations reach this level of convergency. At this point, the impact of convergency levels on the results of hemolysis was investigated. The results demonstrated that convergence criteria with smaller residuals do not induce any significant change in MIH value.

Finally, the inlet and the outlet boundary conditions are applied to be consistent with the experimental conditions [87]. A relative static pressure of $0\ mm\ Hg$ is set at the outlet, and a mass flow rate derived from the experimental Reynolds number is imposed at the inlet. Equation (31) defines the Reynolds number used here [95], which is based on the diameter of the nozzle in the throat region (d_t).

$$Re = \frac{4\rho Q}{\pi d_t \mu} \tag{27}$$

Where ρ, Q, d_t, and μ are the density, the flow rate, the throat diameter, and the dynamic viscosity, respectively. Table 10 gives fluid flow properties to be used in simulations respecting the experimental condition of Herbertson et al. (2011) [85] and Hariharan et al. (2015) [87] for both orientations of the nozzle (sudden expansion and conical diffuser).

Table 10. Fluid flow properties to investigate the Hemodynamic and the Hemolysis aspects of the Nozzle benchmark. "SE" and "CD" stand for Sudden Expansion and Conical Diffuser, respectively (see Figure 14 in section 1.4.1).

Parameter	**Hemodynamic**		**Hemolysis**		
Position	SE	CD	CD	CD	SE
Fluid	Sodium Iodide		Bovine's blood		
$\boldsymbol{Re}$	6500	6500	6568	7882	7882
$\boldsymbol{\rho}\ (\frac{\boldsymbol{g}}{\boldsymbol{ml}})$	1.7	1.7	1.04	1.04	1.04
$\boldsymbol{\mu}\ (\boldsymbol{cP})$	7	7	4.2	4.2	4.2
$\boldsymbol{Q}\ (\boldsymbol{lpm})$	8.25	8.25	5	6	6
$\boldsymbol{d_t}\ (\boldsymbol{mm})$	4	4	4	4	4

2.2.2. Grid Generation

For the FDA Nozzle benchmark, a structured grid was generated by Ansys ICEM. Considering the importance of the throat region in hemodynamic and also Hemolysis predictions [85,86,91,92], the mesh is strongly refined in this area. Figure 33 shows the wall surface mesh distributions and a cross-section at the throat entrance. As shown in Figure 33-b, a boundary layer mesh has been applied at the walls with a first layer thickness of $10^{-6}\ m$. This setup results in a reasonable maximum value of y^+ ($y^+ < 2$) for simulations with $Re = 6500$. In addition, no wall function has been applied in near-wall regions.

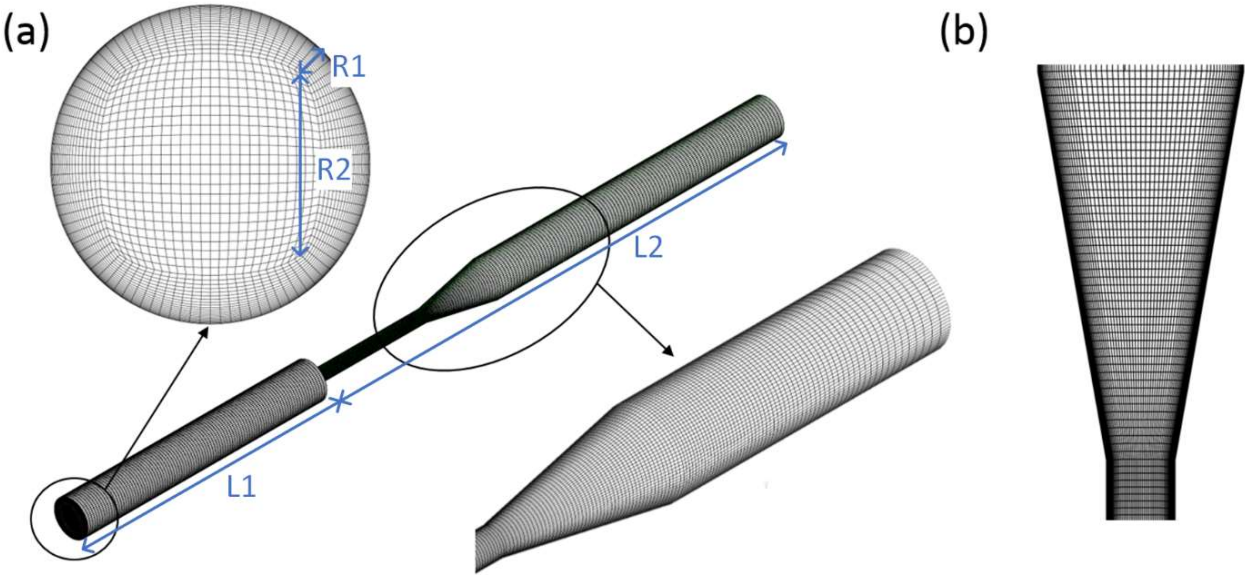

Figure 33. a) Mesh distribution in the nozzle. b) Cross section at the throat entrance.

To check the influence of the mesh on the results, calculations have been performed with four different meshes, using between 0.5 to 2 million cells. Each mesh has different elements numbers on four edges: R1, R2, L1, and L2 (see Figure 33). R1 and R2 adjust the elements numbers for two important edges of the cross-section along the main axis of the domain. On the other side, L1 and L2 define the elements number for the domain's length. Table 11 gives the different values of the 4 meshes.

Table 11. Properties of the 4 different meshes.

Number of cells ($\times 10^6$)	**Number of cells on the edges**				**Calculated y^+**
	R1	**R2**	**L1**	**L2**	
0.5	20	25	60	150	3.24
1	23	30	80	200	2.51
1.5	25	35	100	250	1.89
2	27	38	110	280	1.36

As noted in section 1.3.2, MIH can be obtained both in the numerical simulations and the experimental data, so it is used hereafter to discuss the mesh influence on the results. It is important to note that these preliminary simulations were conducted for a specific operating condition of the conical diffuser with 6 lpm which would be denoted hereafter CD6 (see Table 12 in section 2.2.3.b)).

Figure 34 displays the values of MIH for the different meshes and the error of calculation considering the finest mesh as the reference. It can be seen that MIH is significantly impacted by the increase from 0.5 to 1.5 million cells, while it is nearly the same for the two most refined meshes. Figure 35 indicates the impact of the different meshes on the calculated velocity on the centerline (see Figure 37-a). As shown in this figure, increasing the cell number from 1.5 million to 2 million doesn't result in a sensible accuracy in the results. Consequently, the 1.5 million cells grid is used in the rest of this study.

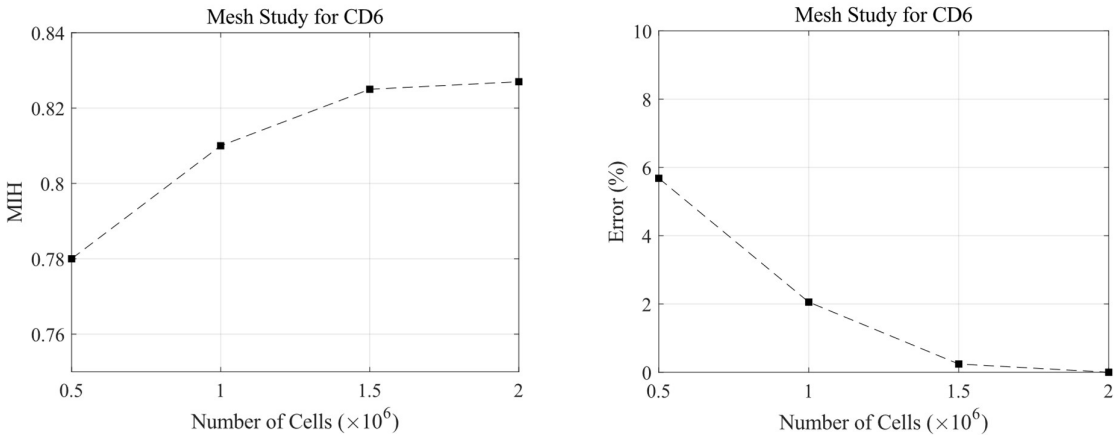

Figure 34. Left: Values of MIH for the four different meshes (condition SC6). Right: Error of calculated MIH considering the MIH value of the finest mesh as the reference.

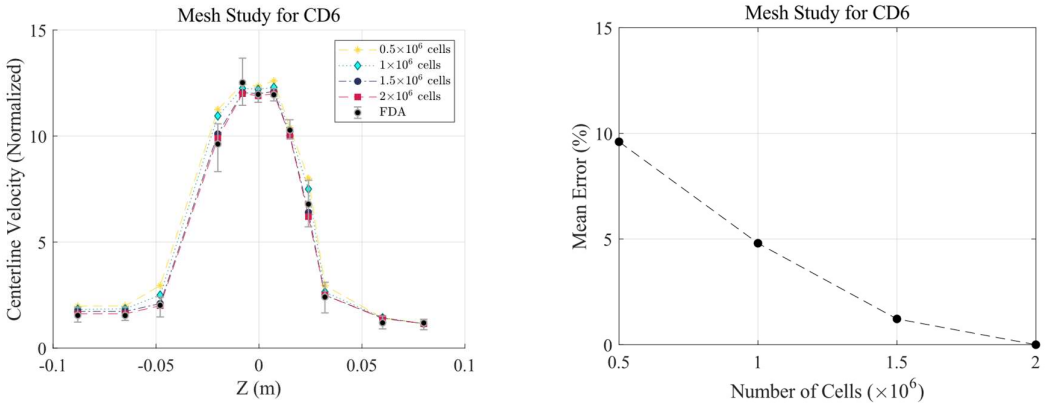

Figure 35 Left: Values of the normalized centerline velocity for the four different meshes (condition CD6). Right: Mean error of calculated centerline velocity considering the experimental data as the reference.

2.2.3. Results

The FDA nozzle benchmark, its geometry, the experimental procedures, and other specifications were described in section 1.4.1. In addition, the numerical methodology to simulate hemodynamics and hemolysis, in this case, was presented in section 2.2.1. In this section, the results of the numerical study, and the verification and validation process are presented.

a) Hemodynamics

The first step in performing a hemolysis simulation is to check hemodynamic results. For this purpose, the results of the CFD simulations are compared to the experimental data of the FDA [87] for both nozzle orientations (sudden expansion and conical diffuser). In the following comparisons, the experimental data have been derived by digitizing from Stewart et al. [91,92].

The comparison is based on the normalized axial velocity, which is based on the axial velocity U_z and the inlet mean velocity $\overline{U_z}$:

$$U_z^* = \frac{U_z}{\overline{U_z}} \tag{32}$$

The comparison has been performed at four different stations, as indicated in Figure 36, for both orientations of the nozzle. These four stations correspond to 4 critical regions: the cylindrical inlet position, the cone position, the throat position, and the cylindrical outlet position.

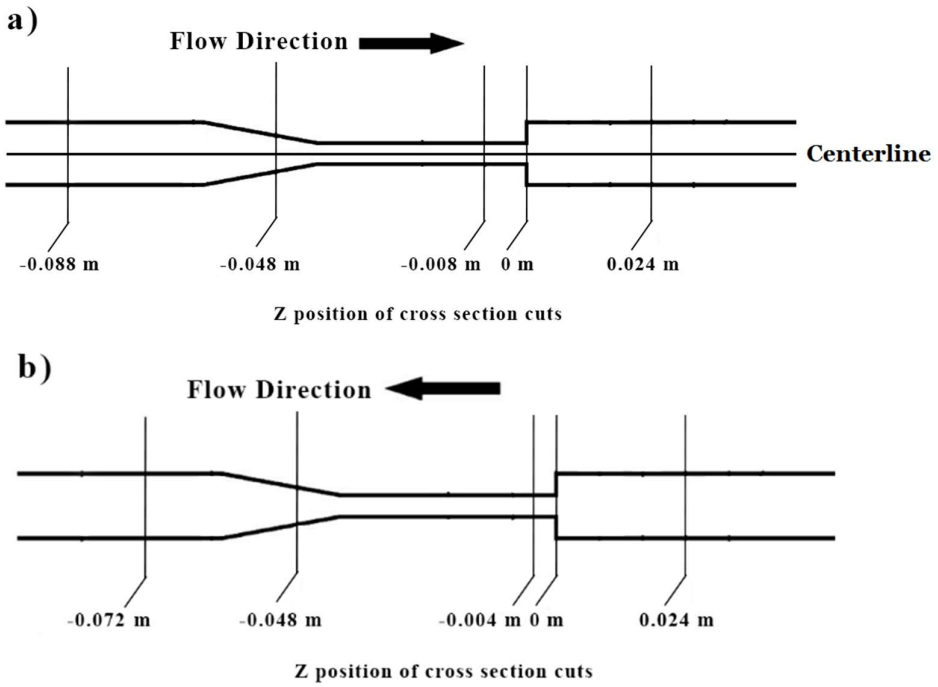

Figure 36. Stations, where comparisons are performed: a) Sudden Expansion (SE) b) Conical Diffuser (CD).

Figure 37-a shows the normalized axial velocity distribution inside the nozzle in the case of the sudden expansion with Re=6500. The large velocity gradient in the cone, as well as the boundary layer expansion at the walls of the throat, can be observed. In the sudden expansion region, the flow exits the throat with a jet-like behavior, which generates a reverse flow in the two corners downstream from the throat (see the streamlines in Figure 37-a).

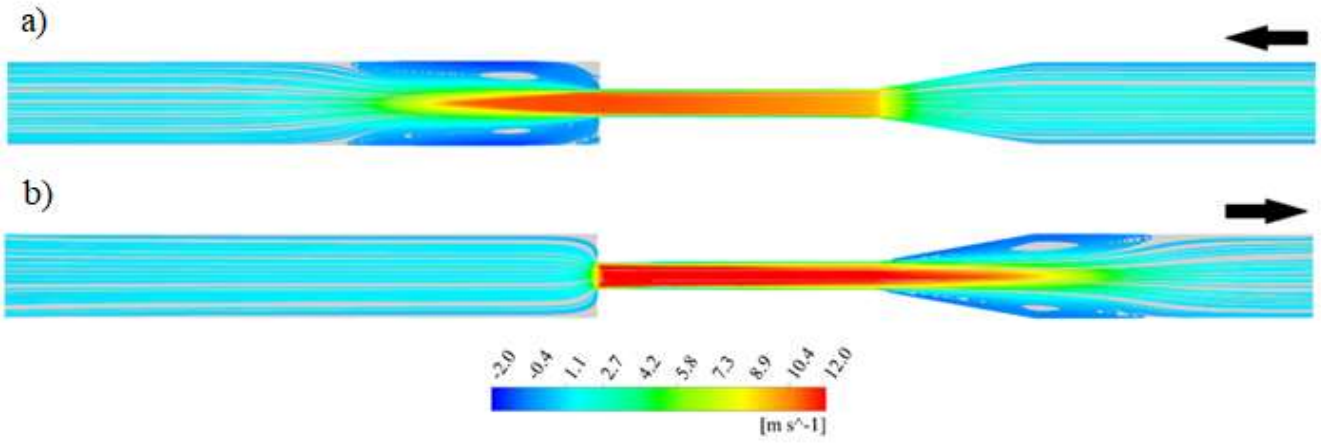

Figure 37. Normalized axial velocity contour and 2D vectors of it inside the Nozzle with Re=6500 for a) Sudden expansion and b) Conical diffuser.

Figure 37-b shows the streamlines for conical diffuser configuration with Re=6500. As for the first case, there is a reverse flow area after the throat, but it's smaller in size. In comparison with the sudden expansion case, it is clear that the velocity gradient at the inlet of the throat is much higher. This might

result in higher local stresses and consequently a larger Hemolysis index for this configuration, which will be discussed in section 2.2.3.b.

Figure 38 shows a comparison of the normalized axial velocity between the numerical results and the experimental data in the case of sudden expansion, in the four cross-sections marked in Figure 36-a. Results obtained with the three tested turbulence models are plotted here. Generally, the largest velocity gradients are obtained in the boundary layers inside the throat (Figure 38-b and Figure 38-c) and downstream in the area of recirculating flow (Figure 38-d). These are the areas of high stress, which should contribute the most to the Hemolysis index. Both the k-ω and k-ω SST models predict velocity profiles in good agreement with the experimental measurements, while higher discrepancies can be observed with the k-ε model, especially downstream from the nozzle. This was expected, as the k-epsilon model is well-known to generate poor results in separated flow areas.

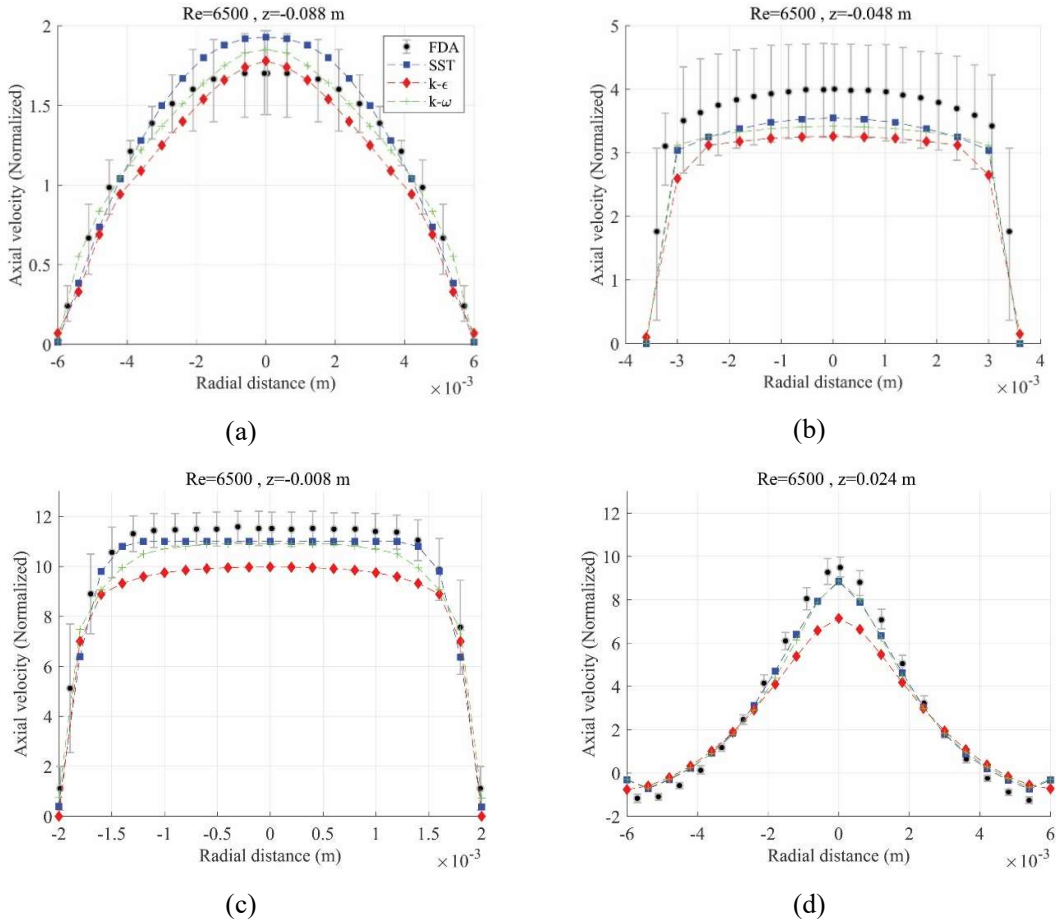

Figure 38. Comparison between experimental and numerical results: axial velocities at Re=6500 for the sudden expansion test case at stations a) z=-0.088 b) z=-0.048 c) z=-0.008 d) z=0.024.

Figure 39 shows the same comparison in the case of the conical diffuser in the cross sections shown in Figure 36-b. Again, the largest velocity gradients are observed inside the throat and in the divergent downstream (Figure 39-b,c). In this test case, the k-ω SST turbulent model best fits the experimental data. Considering the results obtained with the two flow directions, it can be concluded that the results

obtained with the k-ω SST model are the closest to the experiments, especially in the sections submitted to flow recirculation.

The same conclusions were drawn previously by Stewart et al. [91,92]. Some articles in the literature report the use of LES turbulent models to predict the small-scale turbulent structures inside the Nozzle ([90,94,101]). While this approach certainly better resolves the interaction between the boundary layer and the main flow, it is much more time-consuming, which makes it questionable for practical applications. Therefore, the present study is focused on RANS models only. The present results confirm that a nice agreement is obtained with the experiments, which might be sufficient to generate efficient predictions of the hemolysis level. Therefore, hereafter, the k-ω SST model will be used for the hemolysis simulations.

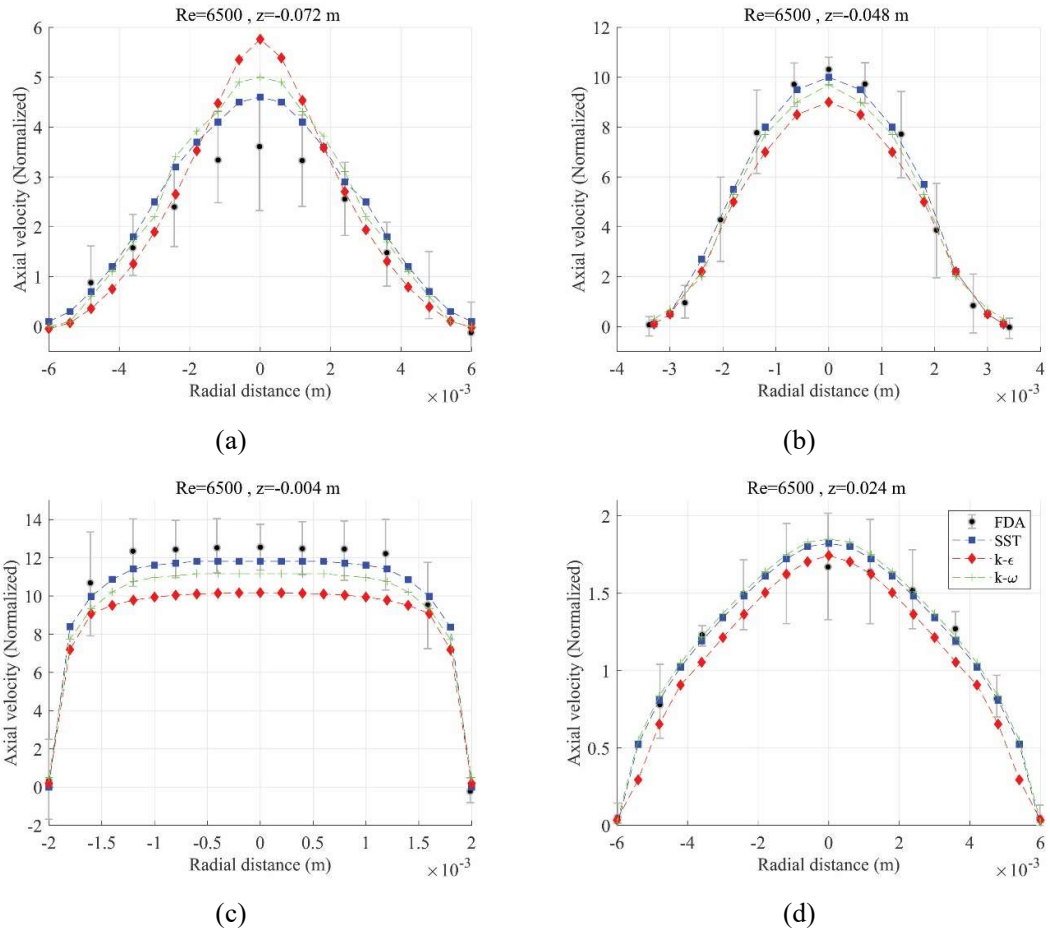

Figure 39. Comparison between experimental and numerical results: axial velocities at Re=6500 for the conical diffuser test case at stations a) z=-0.072 b) z=-0.048 c) z=-0.004 d) z=0.024.

b) Hemolysis

The main objective of this part is to compare various expressions of equivalent shear stress to be used in the Power-law model (equation 5). Hemolysis calculations solving equation 23 in addition to the Navier-Stokes equations were performed, using the three equivalent shear stresses (τ_s, τ_e, τ_n) for three different operating conditions of the nozzle, as indicated in Table 12). Unfortunately, there is no available data for hemodynamic comparison in these specific conditions, but the validation performed previously in several similar flow conditions (see section 2.2.3.a and section 4.2) suggests that the

model generally performs well in the range of Reynolds number investigated here. To be consistent with the experimental condition, the constants of the hemolysis model were selected as Bovine ($C = 9.772 \times 10^{-7}$, $\alpha = 1.444$, $\beta = 0.2076$) (see Table 5). These constants have been provided based on experimental measurements by Ding et al. [18].

Table 12. Flow conditions of the hemolysis tests reported in [85].

Index	Position	Flow rate (lpm)	Re_{FDA}
CD5	Conical Diffuser	5	6650
CD6	Conical Diffuser	6	7860
SE6	Sudden Expansion	6	8020

Hereafter, the present CFD results are compared to both the experimental data and the previous CFD results provided by Tobin and Manning (2020) [86]. In this paper, the flow inside the Nozzle is calculated using a LES turbulent model, in conjunction with the modified model's constants of Ding et al. [18] ($\beta = 0.1$ instead of $\beta = 0.2076$).

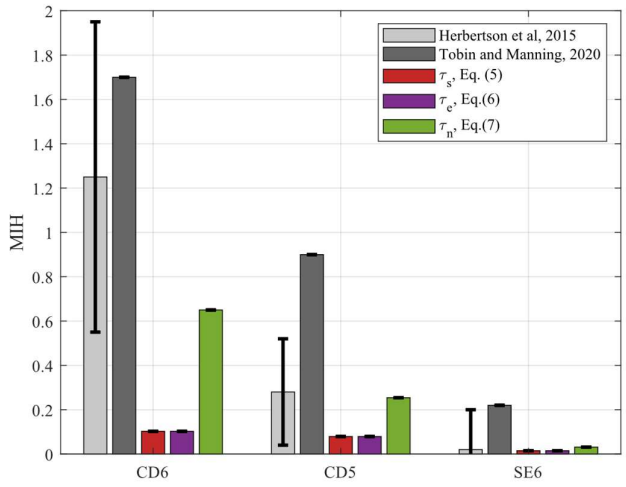

Figure 40. Hemolysis index: comparison between the present results (with 3 different expressions of the equivalent shear stress), the FDA experimental data [85], and numerical results of Tobin and Manning [86].

Figure 40 shows the comparison between the present results, the experimental data reported in [19], and these previous CFD calculations [20], for the 3 flow conditions. It can be observed that the expression of the shear stress has a large impact on the results. More specifically the MIH value obtained with τ_s and τ_e are much lower than the ones obtained with τ_n. As a consequence, for operating point CD6, both τ_s and τ_e result in an underestimation of MIH. On the other hand, τ_n with the default value of C_n ($\sqrt{3}C_n = 33.69$), results in correct ranges of MIH values for all operating conditions. However, it must be emphasized that the value of C_n used here was originally adjusted for human blood, not bovine.

Therefore, an additional study is conducted to investigate the impact of C_n on the calculated MIH for different species.

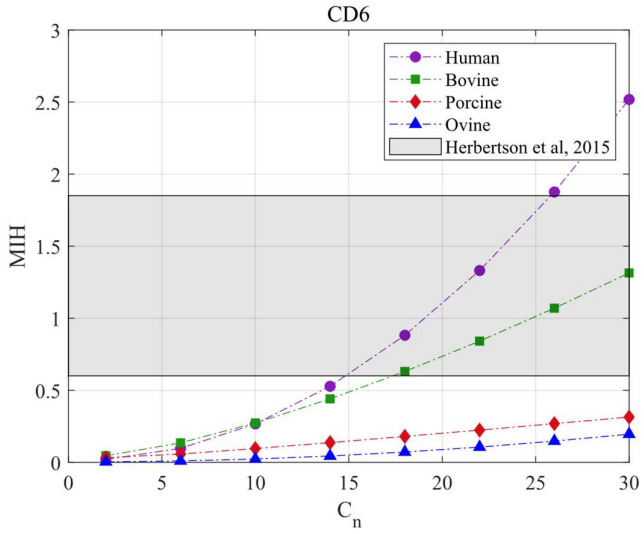

Figure 41. Impact of C_n parameter on the hemolysis index for different species and comparison with the FDA experimental data [85] for the "CD6" flow conditions, using the model constants proposed by Ding et al. [18].

Figure 41 displays the impact of C_n on MIH for different species, in the "CD6" flow conditions, using the model constants proposed by Ding et al. [18]. C_n has a strong effect on MIH, especially for human and bovine blood. In addition, as C_n increases, the difference between the MIH values obtained for different species becomes larger. From a mathematical point of view, this is a direct consequence of using different values of α coefficients for the different species. At this point, we have to reconsider

Table 5 to have a better understanding of the behavior of the curves. For example, the human blood curve is under the Bovine's one for low values of C_n, while it increases at a much higher rate and thus goes well above it for larger values of C_n. Indeed, the Bovine's curve increases semi-linearly ($\alpha = 1.444$) while the Human blood curve has an exponential behavior ($\alpha = 2.0639$). So, generally, we can expect that the behavior of a species is dependent on the α coefficient. In this case, Ovine's curve is not consistent with others as we expect it to be greater than Porcine and Bovine but lower than Human ($\alpha_{Human} > \alpha_{Ovine} > \alpha_{Bovine} > \alpha_{Porcine}$). In this case the impact of two other constants C and β result in a different behavior of the MIH curve of the Ovine.

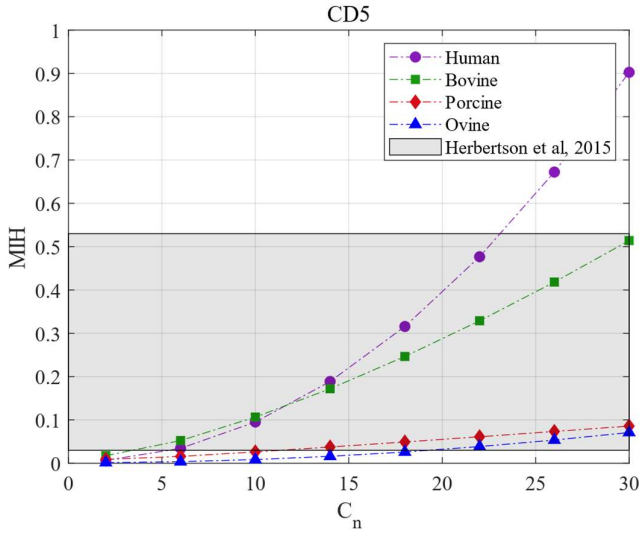

Figure 42. Impact of C_n on hemolysis for different species and comparison with the FDA experimental data [85] in the "SC5" condition, using the model constants proposed by Ding et al. [18].

Based on the Bovine curve, it can be concluded that $C_n > 18$ leads to an appropriate range of MIH in the calculations. Figure 42 and Figure 43 show the same result for the "CD5" and "SE6" operating conditions. Although the large uncertainty in the experimental data makes it challenging to find an optimized C_n value, it can be generally observed that a value larger than 18 and lower than 30 systematically results in MIH values within the experimental range of uncertainty. Values larger than 30 will likely lead to overestimations of MIH. More accurate experimental measurements might enable to come up with a reduced range of appropriate values for C_n in the future, but the present results suggest that using $30 > C_n > 18$ enables to predict a correct equivalent stress and, consequently, a realistic Hemolysis index.

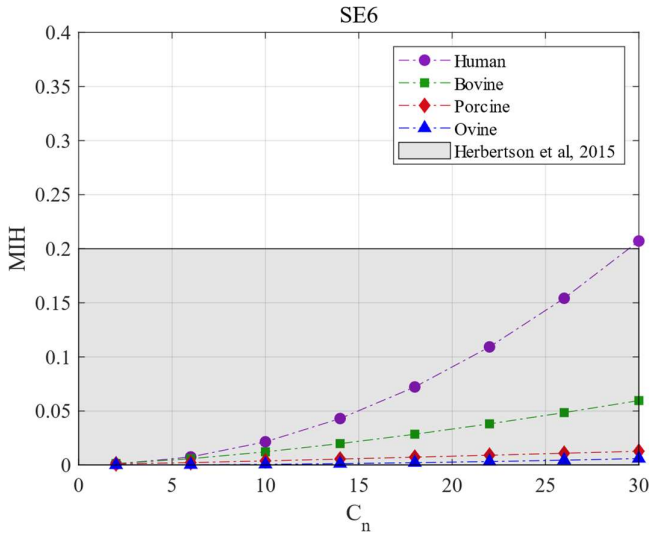

Figure 43. Impact of C_n on hemolysis for different species and comparison with the FDA experimental data [85] in the "SE6" flow condition, using the model constants proposed by Ding et al. [18].

2.2.4. Conclusion

In this section of the thesis, numerical simulation results were presented for the FDA nozzle benchmark. First, the flow field predicted by the model has been validated by comparing it to the FDA experimental measurements for two different operating conditions, one with a sudden expansion upstream from the nozzle, and one with a conical diffuser, for a Reynolds number $Re = 6500$. Three different turbulent models were tested and the k-ω SST model was found to generate reliable results for both configurations.

Based on this approach, the hemolysis index was calculated. Simulations were carried out using two conventional expressions of the equivalent shear stress (τ_s and τ_e) and a more recent one (τ_n). Comparisons with experimental data in three operating conditions have shown that the latter provides the best results. Despite the large uncertainty of the experimental data, the good agreement obtained in the 3 test cases, which generate very different levels of shear stress and thus hemolysis, is quite convincing.

In the last part of the study, the impact of the C_n constant used in the $\tau_n$expression was investigated for different species. Generally, C_n has a large effect on hemolysis, especially for the types of blood where the α coefficient in the model is the largest, i.e. the bovine and human bloods. By comparing the curve obtained with the Bovine blood with the experimental range of MIH at three different operating conditions it could be concluded that an appropriate range for the constant is $18 < C_n < 30$. Additional experimental data in the future might enable us to reduce this range and further improve the quality of the simulations.

In the next section, a similar approach is followed to study the hemodynamic and hemolysis aspects of the second FDA benchmark.

2.3. FDA Pump Benchmark

As mentioned in section 1.4.2, the FDA pump is the second benchmark presented under the Round Robin project[6]; And the purpose of researching this non-commercial pump is to investigate the ability of numerical tools to predict the hemolysis phenomenon. FDA researchers, by comparing the simulation results of several groups with the laboratory results, concluded that the numerical models have shortcomings in predicting this phenomenon [88]. They believe that the present CFD hemolysis techniques ought to be restricted to serving as a means of comparison, rather than making absolute predictions. In this part of the thesis, by comparing the numerical and laboratory results of hemodynamics and hemolysis, we investigate whether the new mathematical models of hemolysis have an improvement in the numerical predictions for this benchmark or not.

2.3.1. Methodology

For the FDA pump benchmark, Reynolds-Averaged Navier-Stokes (RANS) are solved in transient state, using the k-ω SST turbulence model, to simulate the hemodynamic of the blood flow in isothermal condition. The k-ω SST turbulence model was previously reported as the most reliable RANS turbulence model for the simulation of the FDA pump [75,97,98,102]. A second-order scheme is applied to the discretization of the nonlinear convection terms in all transport equations. For hemolysis simulations, the standard transport form of the power-law model (equation 2) is coupled to the RANS equations. The time step used in the simulations is calculated based on the rotor speed n, to have 2^o of rotation per time step (i.e. 0.13 ms for n=2500 rpm and 0.095 ms for n=3500 rpm), and simulations were conducted during 24 rotations. In all simulations, the convergence criteria based on the RMS residuals were set to 10^{-5}, with a maximum of 25 inner iterations allowed at each time step. These values were found to be the best compromise accuracy/time of simulation after a thorough study of their impact on the results was conducted (Figure 44).

Regarding the fluid properties, it is assumed that the blood flow in large arteries (inside the pipes) can be treated as a homogeneous Newtonian fluid [100]. In addition, the shear rates inside the impeller is calculated to be much higher than 100 1/s; and based on the review provide by section 1.1.1 it can be considered as Newtonian fluid as well. So, for the hemodynamic simulations, the dynamic viscosity and the density were adjusted as 4 cP and 1.7 g/ml. On the other side, in hemolysis simulations, they have been set at 3.4 cP and 1.03 g/ml, respectively. The values of the dynamic viscosity and density are selected respecting the FDA's experiment conditions [88].

Malinauskas et Al. (2017) [88] define the Reynolds number for this test case as $Re = \rho n D^2/\mu$. Where, ρ, n, D, and μ are the density in kg/m^3, rotational speed in rad/sec, rotor diameter in m, and

[6] https://fdacfd.nci.nih.gov/

dynamic viscosity in Pa.s, respectively. They reported that the Reynolds number for n=3500 rpm and n=2500 rpm is almost 290,000 and 210,000. Therefore, it is expected to observe turbulent flow inside the impeller for all the operating conditions (Table 13).

Table 13. Flow conditions corresponding to the three analyzed operating points.

Name	Rotational Speed (rpm)	Flow rate (lpm)	Reynolds Number
Operating Point 1	2500	2.5	210,000
Operating Point 2	3500	2.5	210,000
Operating Point 5	3500	6	290,000

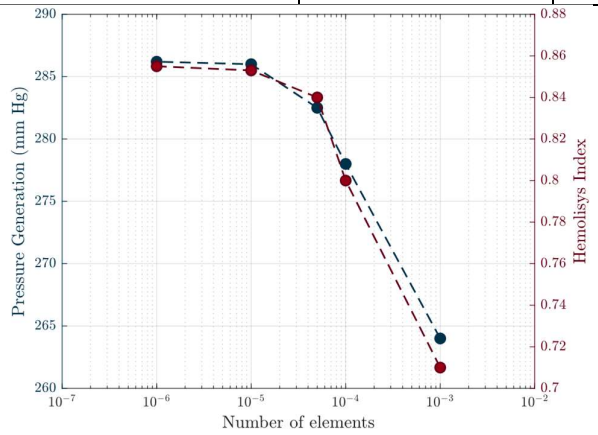

Figure 44. Values of the pressure increase and the MIH for the five different convergence criteria (Operating point 5).

In this test case, the computational domain is separated into three subdomains (see Figure 45): The inlet pipe (green part), The impeller region (pink part), and the outlet pipe (purple part). The inlet and outlet pipes are considered stationary subdomains, while the impeller region is a rotating subdomain. The rotational speed of the impeller is selected according to the operational conditions provided by the FDA (Figure 20). The primary approach for considering the impeller region as a rotating domain is the Multiple Reference Frames (MRF) methodology. The Multiple Reference Frame (MRF) approach applies the rotation effect as an additional source term in the momentum equations, meaning that it is not necessary to physically rotate the mesh. So, at interfaces 1 and 2 the flow data are transferred from stationary to rotating parts and vice versa.

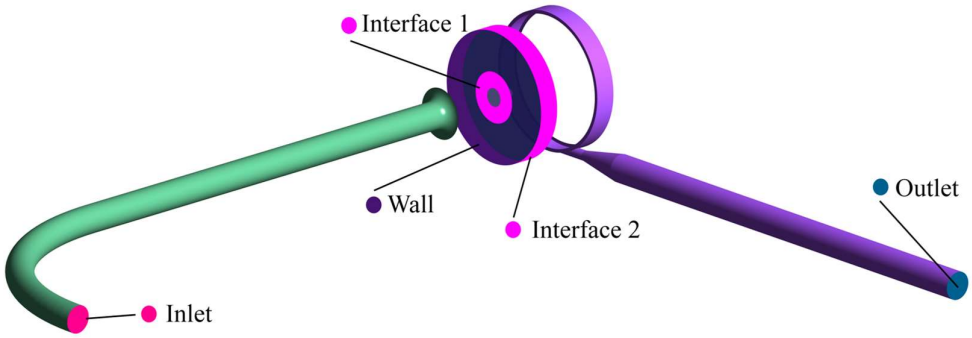

Figure 45. Location of different boundary conditions imposed on FDA pump.

As for the boundary conditions, a relative static pressure of $0\ mm\ Hg$ is set at the inlet, and a flow rate is imposed at the outlet, according to the experimental flow conditions (see Figure 20). In addition, a constant rotational speed is applied to the rotating subdomain ($2500\ or\ 3500\ rpm$ depending on the operating point). Two side-by-side walls in the impeller subdomain are applied as counter-rotating walls, and a no-slip boundary condition is applied to all solid surfaces.

2.3.2. Grid Generation

In this work, unstructured grids were used. Ansys Meshing module creates meshes for such complex geometries by taking global and local properties as inputs. Figure 46 shows different views of the generated grid. As shown in this figure, the tetrahedral meshing methodology is applied with more concentration at the tip of the blades and in the rotor, which are expected to be important areas for correct hemolysis prediction. In addition, boundary layer meshing is applied to the inlet pipe, the outlet pipe, the impeller blades, and the casing with a specified first layer thickness and growing ratio (Table 14).

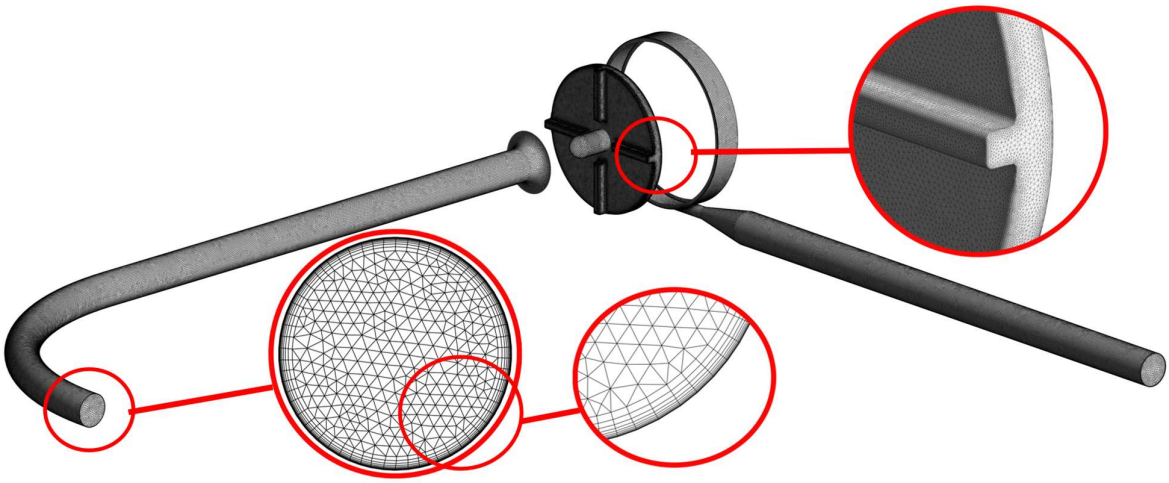

Figure 46. Generated mesh for the FDA pump benchmark.

The impact of the mesh refinement on the results was tested. For that purpose, five different sizes of mesh were compared by monitoring the pressure increase in the pump (ΔP) and the modified index of the hemolysis (MIH). Details about the five meshes are provided in Table 14. The maximum size of the tetrahedrons, the thickness of the first layer at the walls, and the boundary layer expansion ratio were changed to refine the mesh from M1 (2.1 million cells) to M5 (16.2 million cells).

Simulations were performed for operating point 5 (see Figure 20), using the five meshes. Figure 47 shows the values of the calculated ΔP and MIH in the five cases. It can be observed that both ΔP and MIH converge to specific values as the number of cells increases. The convergence can be better appreciated by focusing on the differences between mesh 5 and each other mesh (Figure 47, Right). It can be concluded that increasing the number of cells by over 9.6 million (M4) does not significantly impact the results, so all simulations performed hereafter have been carried out using mesh M4.

Table 14. Properties of the five different meshes for the FDA pump benchmark.

Index	Parameter	Subdomain	Value				
			M1	M2	M3	M4	M5
P1	Max Tet size (mm)	Inlet Pipe	1.5	1.2	1.0	0.6	0.4
P2	First layer thickness (mm)		0.10	0.08	0.05	0.025	0.01
P3	Boundary layer growing ratio		1.30	1.20	1.10	1.07	1.05
P4	Max Tet size (mm)	Impeller	0.8	0.6	0.4	0.2	0.1
P5	First layer thickness (mm)		0.050	0.025	0.010	0.005	0.001
P6	Boundary layer growing ratio		1.20	1.15	1.10	1.07	1.05
P7	Max Tet size (mm)	Outlet Pipe	1.5	1.2	1.0	0.6	0.4
P8	First layer thickness (mm)		0.100	0.080	0.050	0.025	0.010
P9	Boundary layer growing ratio		1.30	1.20	1.10	1.07	1.05
The number of cells (Approx.)		All domains ($\times 10^6$)	2.1	4.0	6.5	9.6	16.2

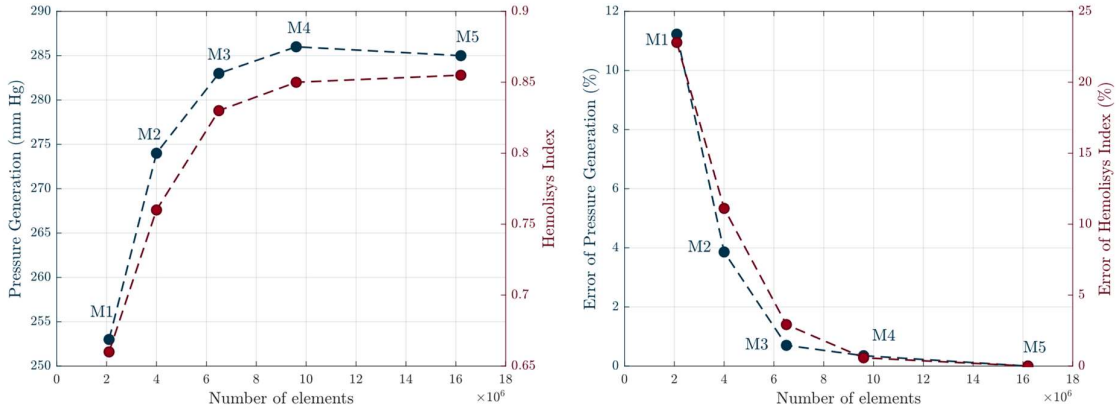

Figure 47. Left: Values of the pressure increase and the hemolysis index (MIH) for the five different meshes (Operating point 5). Right: Difference between the results obtained with mesh 5 and each other mesh.

2.3.3. Results

a) Hemodynamic

An accurate prediction of the hemolysis index requires a correct estimation of the shear stress in the flow, which in turn requires an accurate prediction of the velocity gradients, and thus a good simulation of the flow field in general. Therefore, this section is focused on the comparison of the hemodynamic parameters (e.g., pressure and velocity) with previous experimental measurements [88]. Qualitative and quantitative comparisons were performed in both the impeller and the diffuser. These are reportedly the most critical areas in the FDA pump test case [103]. Transient simulations were performed for three operational conditions (operating points 1, 2, and 5). In each case, the rotational speed and the flow rate boundary conditions were adjusted to be consistent with the experiments (see Figure 20).

Firstly, a qualitative comparison between experimental and numerical data is shown by plotting velocity contours in a cross-sectional plane located 1.2 mm from the top surface of the impeller blades (see Figure 48). In the FDA PIV measurements, the velocity field was obtained by averaging results of 500-2500 pairs of images captured at a given rotor speed (with a constant position of one of the blades, in regards to the outlet pipe) [88]. Similarly, numerical data were averaged over the latest 10-timesteps calculated with one blade in the same position.

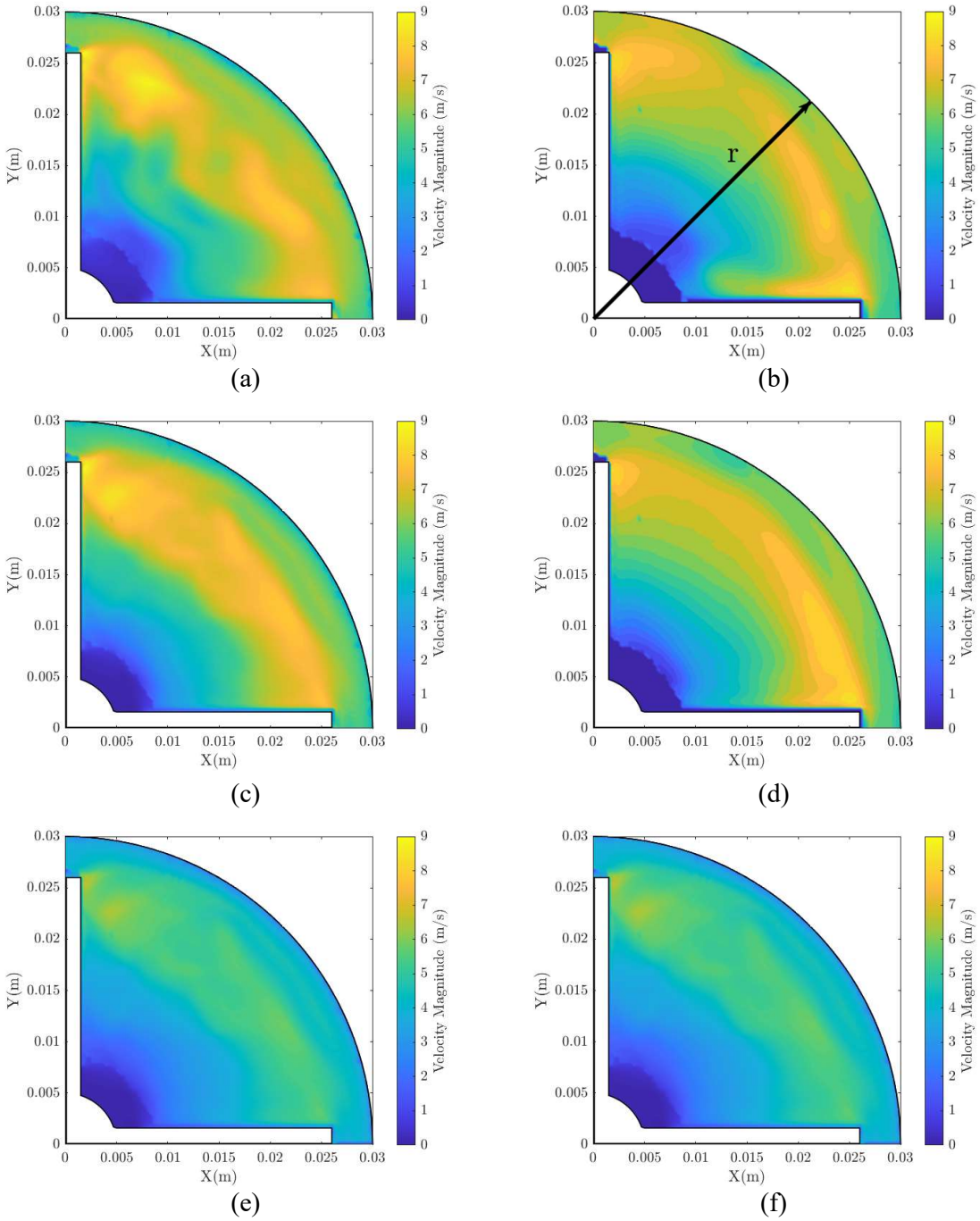

Figure 48. Distributions of velocity magnitude in a cross-sectional plane in the impeller and comparison between FDA PIV measurements [88] (b, d, and f) and numerical predictions (a, c, e) for three operating conditions: 1. operating point 5 (a and b). 2. operating point 2 (c and d). 3. operating point 1 (e and f).

As shown in Figure 48, the velocity magnitude distribution inside the impeller depends significantly on the radial distance from the center. The highest velocity values can be observed at the tip of the blades, while the central regions are characterized by low speeds in all cases. So, the tip region is expected to be the primary source of hemolysis in the impeller due to the resulting stresses.

It is also found that the rotational speed does significantly affect the velocity distribution inside the impeller, while the flow rate does not (see the comparison between operating point 2 and operating points 1 and 5, respectively). By comparing the plots in Figure 48, a fair agreement between the experiments and the simulations can be generally observed. Quantitative comparisons are also performed hereafter.

Figure 49-a displays the velocity magnitude evolution along a diagonal line at 45° (line 'r' shown in Figure 48-b) in the same cross-section. The numerical results are compared again to the data obtained previously by PIV by two different laboratories and denoted ‘lab1’ and ‘lab2’. Despite some deviation at the blade's tips, it shows that the CFD is in close agreement with the experiments., The relative error between the calculated velocity and the one obtained by PIV (Lab 2, $e=|V_{PIV}-V_{CFD}|/ V_{PIV}$) is plotted through the same radial line in Figure 49-b. It can be seen that it is always lower than 10%, which confirms the good accuracy of the numerical simulation within the impeller.

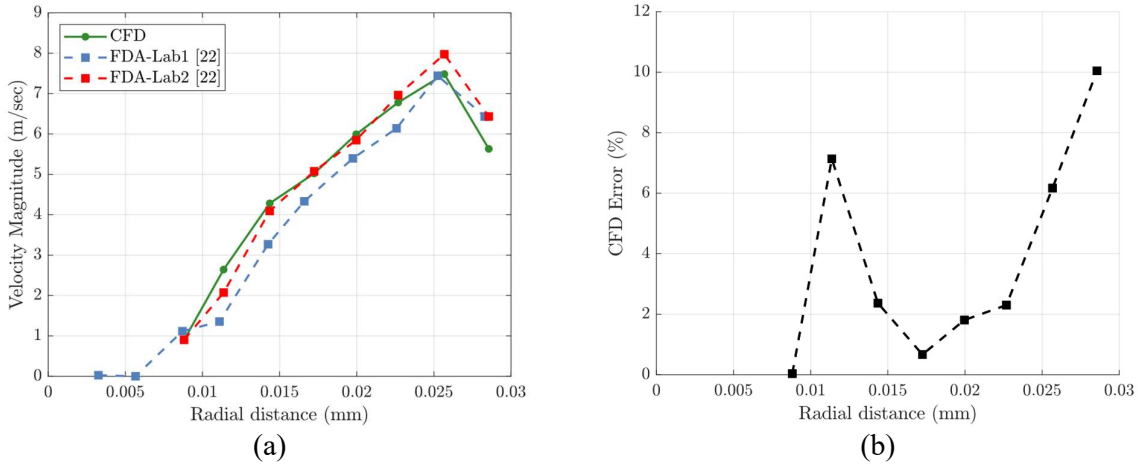

Figure 49. a) Comparison between numerical and experimental profiles of the velocity magnitude against the radial distance from the center of rotation. b) Error between the CFD calculated velocity and the PIV measurements (Lab 2).

A similar comparison was performed in the conical diffuser. In this region, the flow has a stochastic behavior, as reported by other papers [88,103–105]. Here, the flow forms a jet inside the diffuser, and the jet direction fluctuates according to time, so the time-averaged data used here might be quite sensitive to the amount of data used to calculate them, both in CFD and PIV.

Firstly, a qualitative comparison has been performed between the numerical predictions and the PIV data, based on the velocity field (Figure 50). As shown in Figure 50, the velocity magnitude and direction depend on both the flow rate and the rotational speed. For example, for operating condition 5, the flow

tends to deviate to the right, while for the two other conditions, it leans to the left side of the pipe. Nevertheless, the velocity distribution becomes uniform for all operating points as the cross-section area increases along the diffuser.

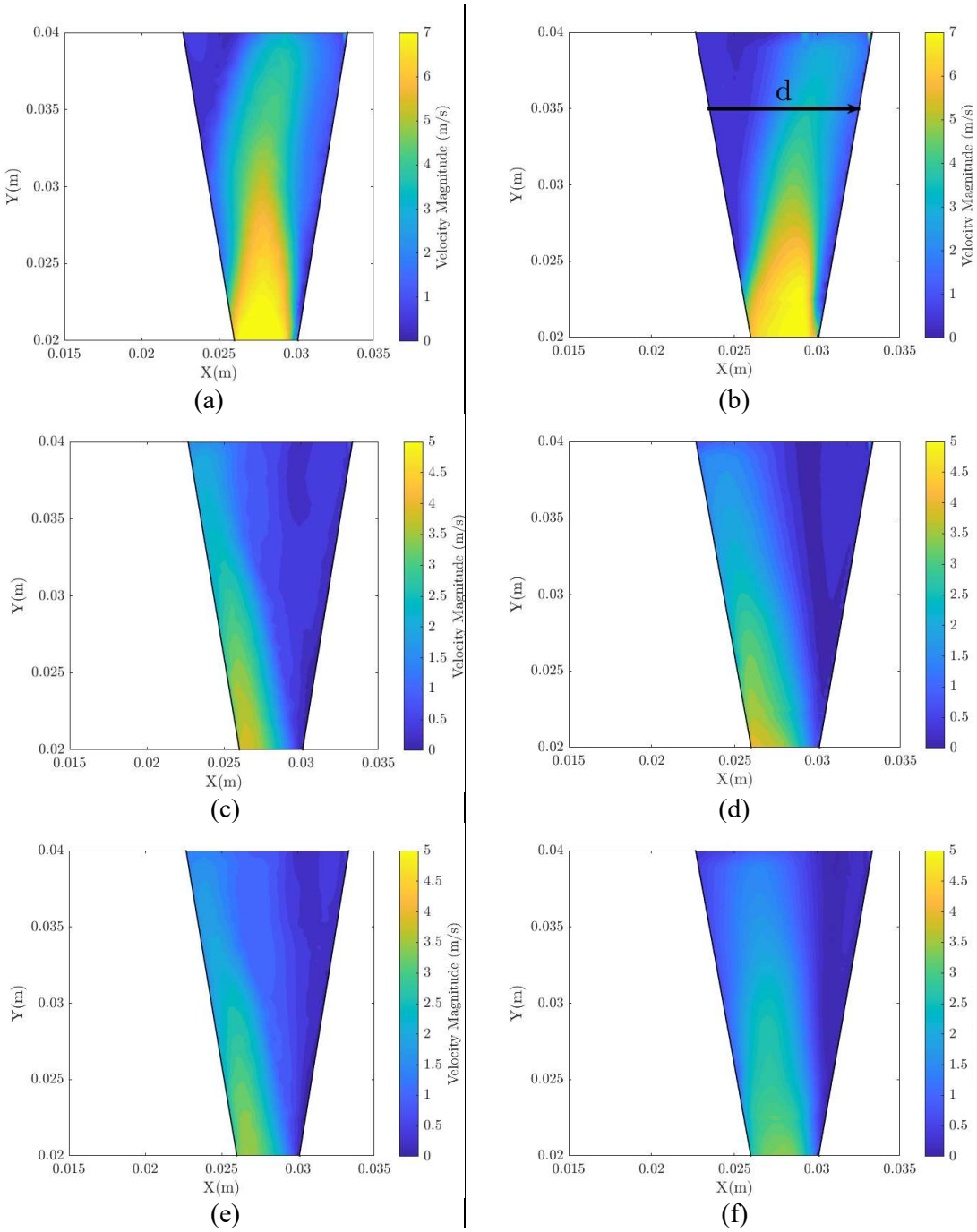

Figure 50. Velocity contours plotted on a cross-sectional plane in the diffuser region and comparison between FDA PIV measurements [88] (b, d, and f) and numerical predictions (a, c, e) for three operating conditions: 1. operating point 5 (a and b). 2. operating point 2 (c and d). 3. operating point 1 (e and f).

Figure 50-a,b and Figure 50-e,f display the comparison between the CFD and FDA results for point 5 and point 1, respectively. In these two cases, the CFD tool can precisely predict the velocity magnitude

across the diffuser but some discrepancy in the jet direction can be observed. On the other side, both the magnitude and the jet direction are very well predicted for operating point 2 (Figure 50-c,d). It confirms that larger samples of data on both sides would be needed to account for the intense fluttering of the jet in the diffuser and improve this comparison.

For quantitative comparisons, the velocity profiles are plotted over a horizontal line across the diffuser (line 'd', see Figure 50-b) for operating point 5. Figure 51-a shows some instantaneous velocity profiles at different successive timesteps with the rotor always in the same position (with one of the blades positioned 90° to the outlet). It confirms that the jet is highly unstable, with a position of the maximum-velocity that fluctuates along the x-axis through time. Figure 51-b shows the comparison between the two FDA measurements and the numerical results, using different strategies for time-averaging. It is clear that the numerical velocity profiles tend to converge to a fixed curve by extending periods of time-averaging. In addition, discrepancies can be observed between PIV measurements in the two laboratories as well. This could be a consequence of uncertainties in blood properties and testing equipment. Anyway, the comparison between numerical predictions (with the biggest averaging period) and PIV measurements of Lab 1 indicates the convincing reliability of the hemodynamic method.

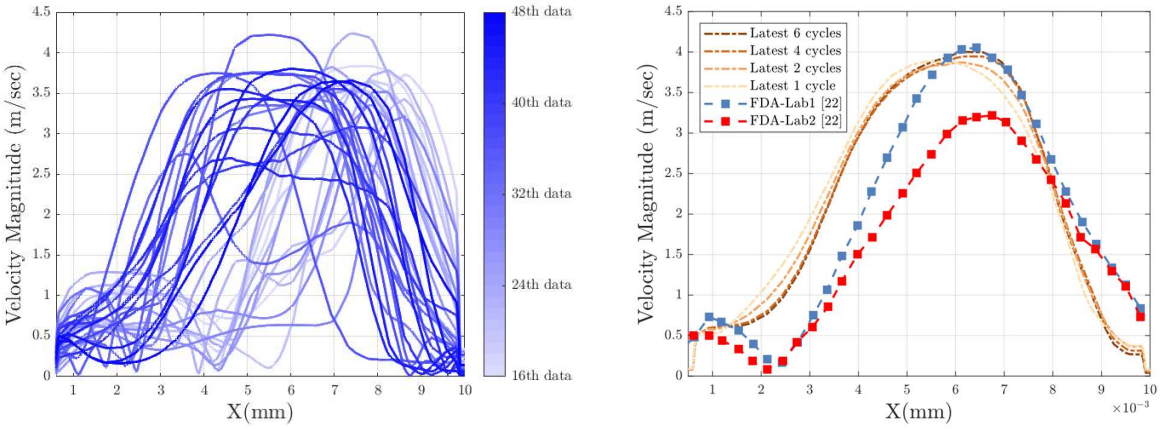

(a) (b)

Figure 51. a) Instantaneous velocity magnitude against distance from the wall for different simulation timesteps. b) Comparison between numerical and experimental profiles of the velocity magnitude against the distance from the wall.

The pressure elevation in the FDA pump is another checkpoint for hemodynamic validation. The difference between the total pressure at the inlet and the outlet was calculated for each case ($\Delta P = P_{Tot,Out} - P_{Tot,in}$). Experimental data exist for two operating fluids: Sodium iodide used for PIV measurements and porcine blood used for hemolysis tests. On the other hand, CFD simulations were conducted with the fluid properties of the FDA hemodynamic experiments (see section 2.3.1). Figure 52 shows the comparison between the experimental and numerical values of the pressure elevation. CFD predictions are in fair agreement with the experiments: the values always fall within the range of uncertainty of the experiments, and the discrepancies are generally lower than 10%. It confirms that the

flow field is quite correctly predicted by CFD, regarding both global aspects and the local flow properties, so the proposed numerical framework can be used to perform hemolysis calculations.

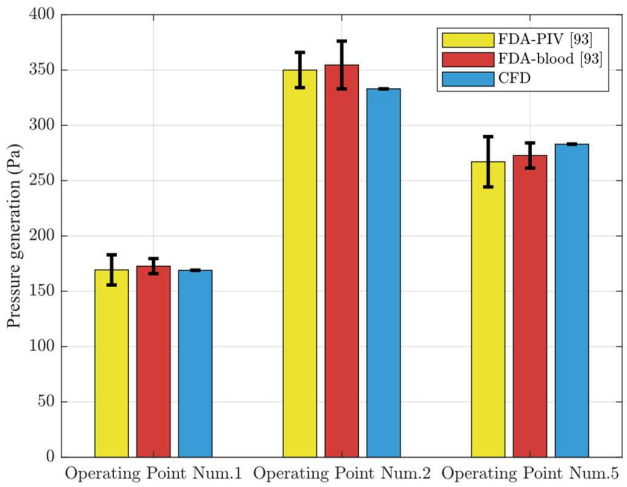

Figure 52. Pressure elevation in the pump for three operating conditions. Yellow: FDA PIV measurements, Red: FDA with blood in the hemolysis tests, and Blue: CFD simulation results with FDA PIV material properties (see section 2.3.1).

After validating the simulation from the hemodynamic point of view, it is now possible to present the visualizations of the flow field inside the FDA pump. These observations help us understand the sources of the hemolysis phenomenon.

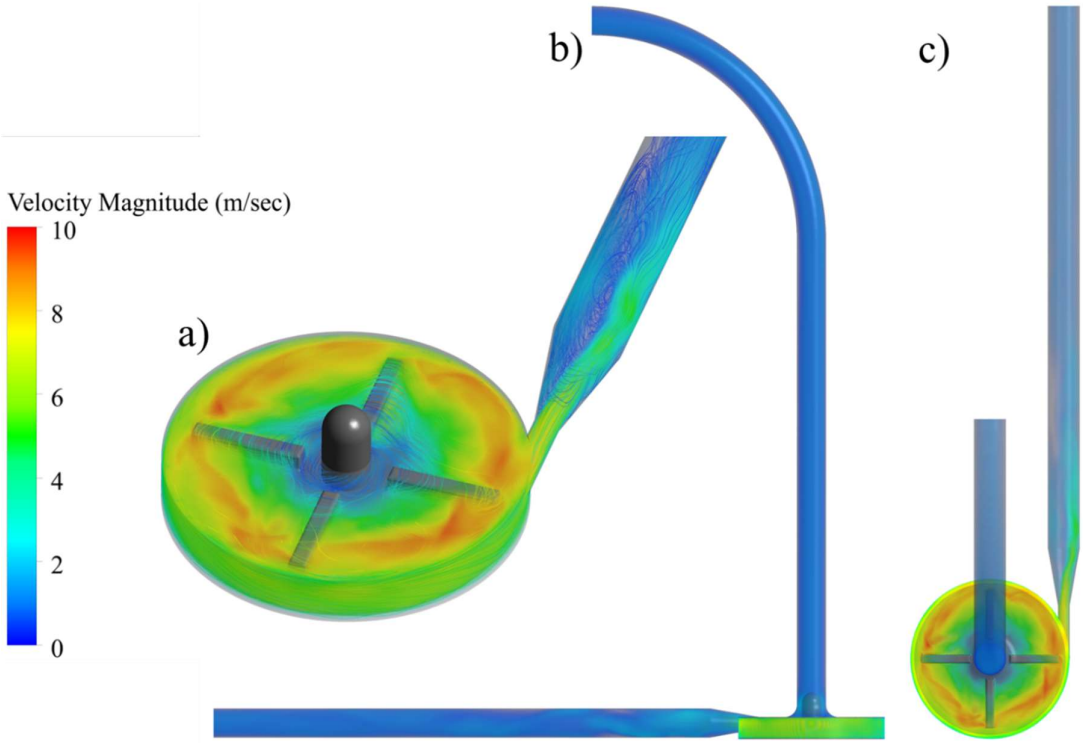

Figure 53. Volume rendering and streamlines of the velocity magnitude for the FDA pump benchmark operating in Point 5. a) isometric view of the impeller and the outlet pipe. b) Side view of the results. c) top view of the results.

Figure 53 shows the volume rendering of the velocity magnitude as well as the 3D streamlines for the operating point 5 from different angles. The flow enters the pump from the top inlet pipe. Inside the pump, the velocity of the fluid flow increases due to the high rotational speed of the rotor (n=3500 rpm). Then, it exits from the conical diffuser region, where a vortex regime starts to appear. This area is reported to be the most questionable point in terms of simulation results [79,88]. Inside the impeller, the velocity magnitude is more dependent on the radius, as expected. Higher velocities can be seen at the tip of the blades, while, for the inner side of them, a flow stagnation area is noticeable. Considering this figure, it is expected to probe higher values of hemolysis index at the tip of the blades. This fact should be followed up by the next section of the thesis.

b) Hemolysis

In the next step, the standard transport equation of the power-law model was coupled to the fluid equations in the simulation. At this point, the main objective is to evaluate the efficiency of a new expression for the equivalent stress provided by Faghih and Sharp [84] (equation 28). For that purpose, numerical predictions of the hemolysis index are compared to the experimental measurements [88] for three operating conditions. To respect the original definition [84], the C_n parameter is set equal to 19.45 knowing that the experimental tests were held for the human blood and not for the porcine. Figure 60 demonstrates the comparison between the CFD predicted MIH and the experimental measurements. It is clear that the CFD values are inside the experimental uncertainty range for all operating points. However, all calculated MIH values are lower than the mean values of the measured hemolysis index. This observation has motivated us to investigate the impact of the C_n parameter on the CFD predictions.

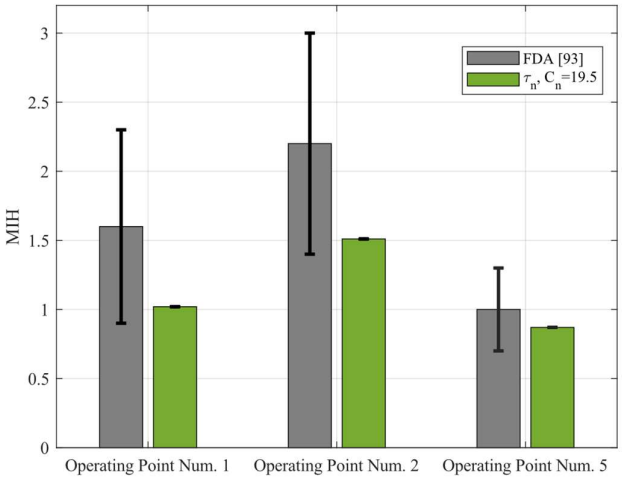

Figure 54. Calculated MIH based on the novel definition of the equivalent stress defined by Faghih and Sharp [84] ($C_n = 19.45$) for three operating points of the FDA pump.

Figure 55 shows the volume rendering of the calculated MIH in the impeller region for the three operating points. The maximum values of the MIH parameter can be observed at the tip of the blades,

for both sides of them. Moreover, the maximum values of the MIH are located in the regions with the highest velocity gradients (see Figure 48). By comparing the three figures, the MIH distribution inside the impeller is highly affected by the operating condition of the pump. For example, MIH values for operating condition 5 are higher than those in operating point 1. It clearly indicates that the MIH values are directly related to the velocity and its gradients. In other words, the hemolytic levels of the blood pumps are dependent on the rotational speed and the flow rate. These are the two parameters that impose the velocity magnitudes inside the blood pump.

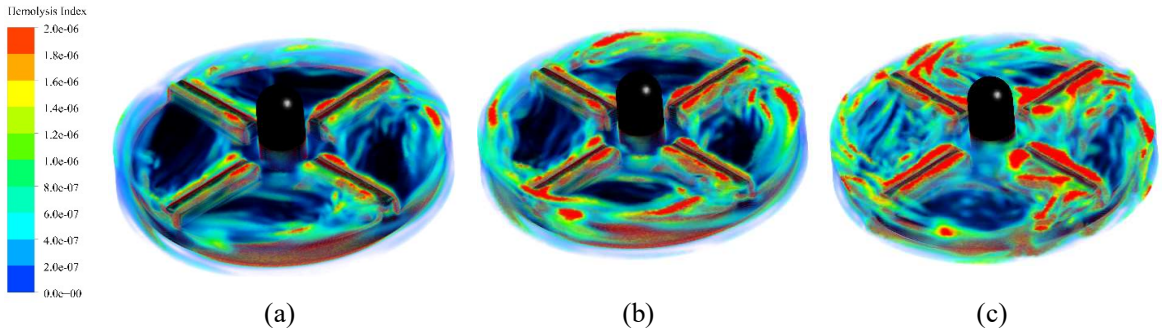

Figure 55. Volume rendering of the calculated MIH in the impeller based on the novel definition of the equivalent stress defined by Faghih and Sharp [84] ($C_n = 19.45$) for three operating points of the FDA pump. a) Operating point 1. b) Operating point 2. c) Operating point 5.

Simulations were thus conducted for a wide range of the C_n parameter ($2<C_n<30$ with an interval of 4). In addition, they were repeated for different species to investigate the influence of the C_n parameter and the blood properties simultaneously. Figure 56 shows the results for operating point 1. The MIH values were plotted against the C_n parameter with a logarithmic scale. Considering this graph, it is clear that increasing the C_n parameter results in an exponential increase in the MIH. So, adjusting a reliable value for it can efficiently improve the accuracy of the simulations.

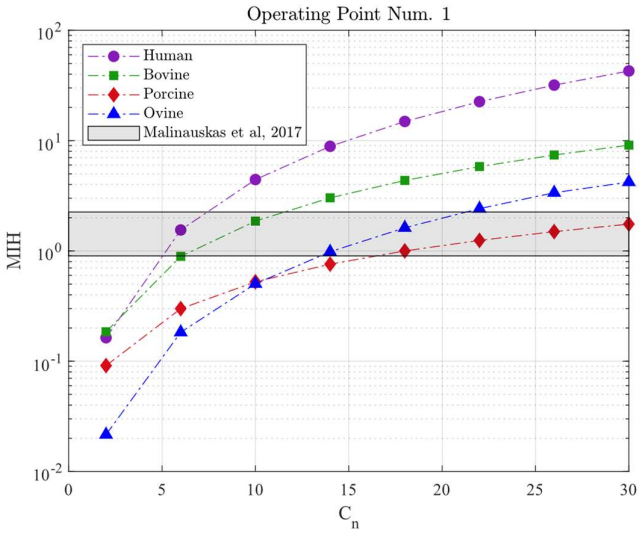

Figure 56. MIH against C_n for different species and its comparison with experimental data for the operating point 1.

By comparing porcine's curve with the experimental uncertainty range [88], it can be claimed that for 18<C_n<30, CFD predictions are the closest to the experiments. The conclusion has to be tested for other operating points, too. In addition, we can also conclude that human blood has the most significant response to the C_n parameter among all species. As the C_n increases, the discrepancies between the curve of the human blood and others become more evident, which is a consequence of the higher α value (see

Table 5).

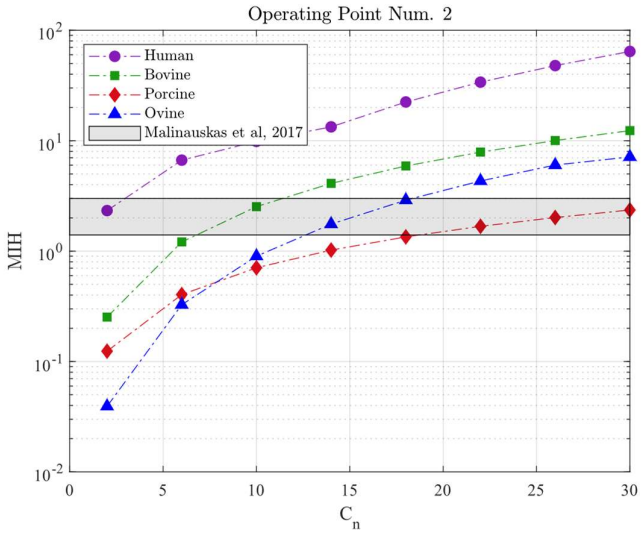

(a)

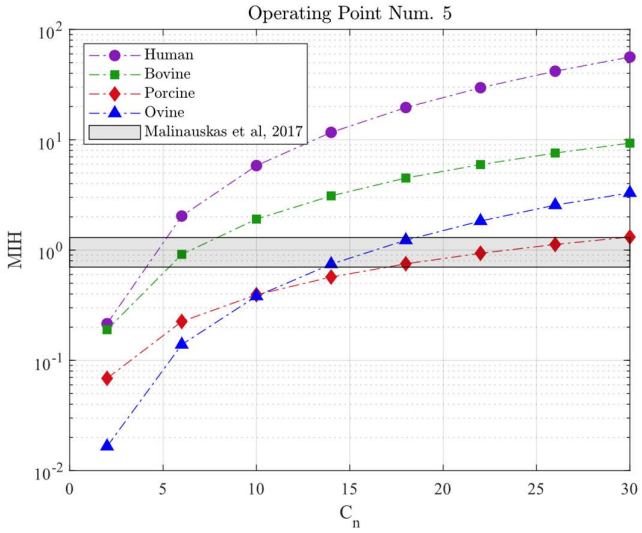

(b)

Figure 57. MIH against C_n for different species and its comparison with experimental data for a) Operating point 2. b) Operating point 5.

Figure 57 shows a similar comparison for operating points 2 and 5. Generally, similar conclusions can be drawn: the curve of the human blood is on top of the others, even for low values of C_n. and the range of appropriate values for C_n is C_n≥18, for operating point 2 and 15<C_n<27 for operating point 5.

As a result of this study, it is found that the intersection of these three ranges obtained for the three operating points is $18<C_n<27$: For C_n selected in this range, numerical modeling can predict the hemolysis index inside the experimental uncertainty range provided by the FDA [88]. Based on this test case, the most appropriate values for C_n, which provide results in reliable agreement with the measurements for all operating points, would be the center of this range, i.e. 22 to 23.

Figure 58 demonstrates the volume rendering of the calculated MIH inside the impeller for the operating point 5 of the FDA pump with different C_n values. As expected, the calculated MIH using equation 28 is highly affected by changing the C_n parameter. For the lowest value of C_n, critical regions of the hemolysis are predicted to occur at the tip of the blades within a very narrow region. On the other side, for $C_n = 27$, the maximum values of the MIH are located at the same region but with a larger size. In addition, critical regions can be observed in the area between the impellers as well.

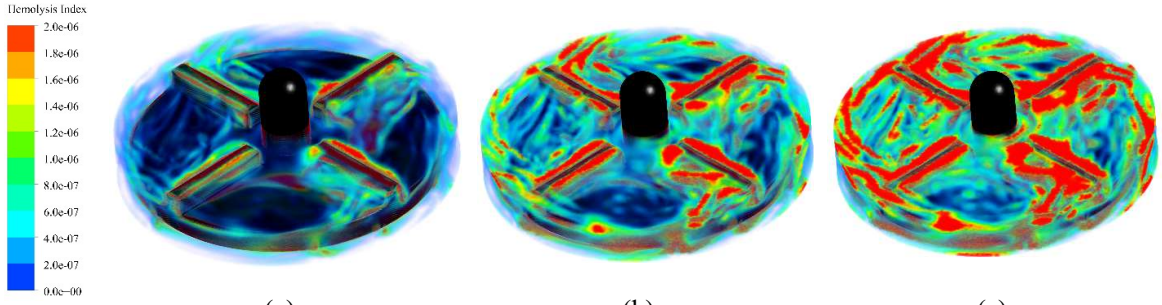

Figure 58. Volume rendering of the calculated MIH in the impeller based on the novel definition of the equivalent stress defined by Faghih and Sharp [84] for the operating point 5 of the FDA pump with different C_n values. a) $C_n = 9$. b) $C_n = 18$. c) $C_n = 27$.

2.3.4. Conclusion

In the present study, numerical simulations were carried out to predict hemodynamic and hemolysis of the blood flow inside the FDA pump benchmark. The Power-law model with an eulerian approach was applied, and a new expression of the equivalent shear stress proposed in the literature was tested.

Firstly, numerical predictions over the flow field, based on a RANS approach, were validated by comparing our CFD results to the FDA experimental measurements for three operational conditions. Velocity distributions and pressure elevation inside the pump were compared to the experiments, and a nice agreement was obtained regarding both the global aspects and the local flow variations.

Then, the hemolysis index was calculated by coupling the additional standard transport equation of the power-law model to the RANS equations. Simulations were carried out using a new definition for the equivalent stress τ_n. Comparisons with experimental data at three operating conditions have shown that the new methodology provides accurate results. Despite a non-negligible uncertainty on the experimental data, a good agreement was obtained for the three operating points, which confirms the ability of this framework to predict the hemolysis index in various configurations.

In the last section of the thesis, the impact of the C_n constant used in the τ_n expression was studied for different species. Generally, C_n has a significant effect on hemolysis, especially for the species where the α coefficient in the model is the largest, for example, the human blood. By comparing the curve obtained with the Bovine blood with the experimental range of MIH at three different operating conditions, it could be concluded that an appropriate range for the constant is $18<C_n<27$, with an optimal value around 22 - 23. Additional experimental data in the future might enable us to reduce this range and further improve the quality of the simulations.

2.4. FineHeart Blood Pump

As mentioned in section 1.4.3, the ICOMS is a novel blood pump that was first invented by FineHeart in 2011 and developed since that time. Through the development process of the innovation, several experimental tools were used (e.g., correlation loop, PIV setup). In this thesis, numerical simulations have been performed in the same experimental conditions, in order to further validate the numerical approach and also analyse the mechanisms of hemolysis generation, from a fluid mechanics point of view.

2.4.1. Numerical Methodology

a) Correlation loop tests

As mentioned in section 1.4.3, the objective of the correlation test loop was to evaluate the performance of the pump and the operation of its sub-components (Inducer, Impeller, and Diffuser). To complement this approach, a CFD method was developed to calculate the flow field in these three sets of blades. The three parts of the hydraulic system were modeled and meshed separately (see Figure 59). Generated grids were finally coupled within the CFD solver.

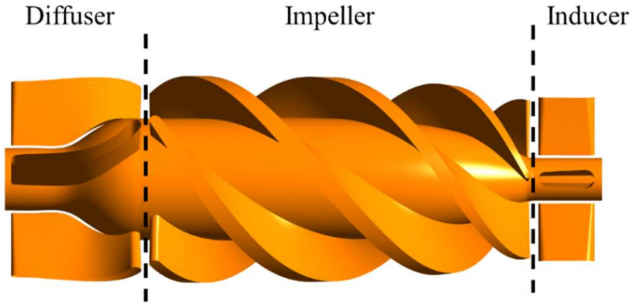

Figure 59. Each part of the ICOMS hydraulic system (Inducer, Impeller, and Diffuser) was modeled and meshed separately.

In terms of numerical simulation, steady calculations were carried out with the Reynolds-Averaged Navier-Stokes (RANS) framework in isothermal condition, using the k-ω SST turbulence model, based on our conclusions with the FDA benchmarks. In addition, the Newtonian viscosity model is applied, since the shear rates inside the pump is much higher than the criteria provided by section 1.1.1: the blood density and viscosity are set to 1050 kg/m^3 and 4 cP, respectively, which is consistent with the experimental conditions. The second-order discretization scheme are used for the approximation of nonlinear convection terms in all transport equations, and the convergence criteria are offset to 10^{-5} for all residuals. In addition, the set of governing equations is discretized in time with the 2nd order backward Eulerian approach.

Figure 60 shows the boundary conditions for the ICOMS correlation loop simulations. According to the operational conditions of the ICOMS, variable static pressure and mass flow rate are adjusted

according to the inlet (the green plane) and outlet (the purple plane) of the domain, respectively. As described in section 1.4.3, there are three separate computational sub-domains. In this study, the sub-domains for the inducer and the diffuser are considered as stationary regions. On the other hand, the impeller is set as a rotating region. It should be noted that the frozen rotor model is selected for the interface between stationary and rotating sub-domains (the red and the blue planes). A no-slip boundary condition is applied to all solid surfaces.

Table 15. Considered boundary conditions for numerical simulation of the ICOMS correlation loop.

Boundary	Type	Value	Unit
Inlet	Static pressure	60	mm Hg
Outlet	Flow rate	0-6	l/min
Impeller	Rotating domain	2000-7000	rpm
Inducer and Diffuser	Stationary domain	-	-
Interface 1 & 2	Interface	Frozen rotor	-

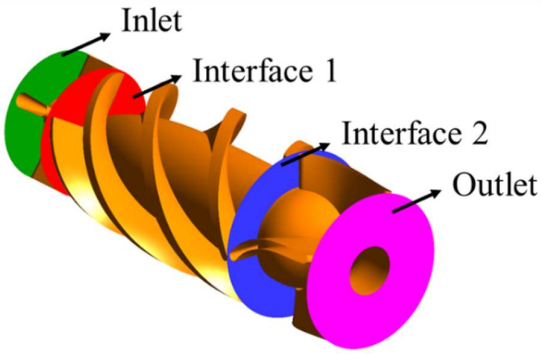

Figure 60. Boundary conditions of the ICOMS correlation loop simulations.

Table 15 contains detailed specifications about the numerical methodology and boundary conditions for this type of simulation. As mentioned in this table, the rotational speed and the flow rate are adjusted for each operating condition. The experimental H-Q curves (see Figure 61) will be used hereafter to perform some quantative comparisons of the pressure elevation in the pump.

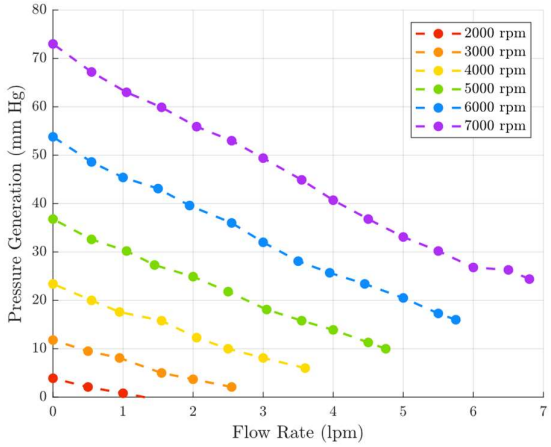

Figure 61. Pressure generation against flow rate for different rotational speeds of the ICOMS measured by the correlation loop test bench.

Considering the same expression defined by the FDA, the Reynolds number ($Re = \rho n D^2/\mu$) of this test case is about 11000 and 49000 for n=2000 rpm and n=7000 rpm, respectively.

b) Comparisons with Particle Image Velocimetry (PIV)

The pump operation was significantly different in the experiments where the PIV measurements were performed, so for comparisons with these specific data, the numerical framework had to be adjusted. In this case, the ICOMS is positioned inside the PIV box vertically (Figure 62), with the outlet of the pump located at a certain distance from the box outlet. The rotation axis of the pump is aligned with the axis of the outlet pipe, and the distance between the pump outlet and the box wall is set at 16 mm. Inside the box, the fluid flow is sucked into the pump and pushed through the outlet pipe. As mentioned in section 1.4.3, the objective of the PIV measurements was to visualize the flow pattern outside from the pump.

.

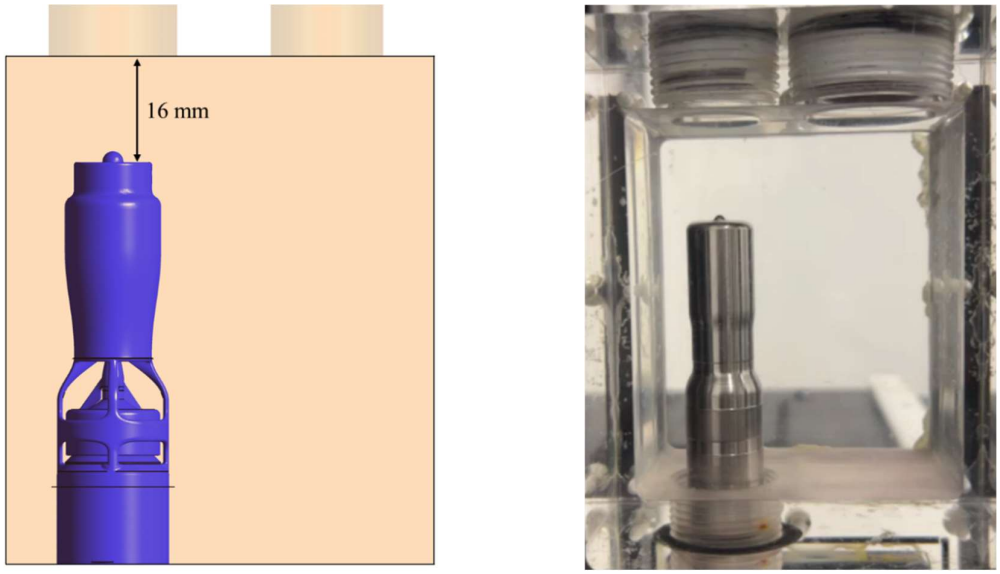

(a) (b)

Figure 62. a) Positioning of the pump inside the PIV box for the CFD simulations. b) Actual position of the pump inside the PIV box in the experiments.

Generally, the numerical framework is very similar to what was explained in the previous subsection (RANS wth K-ω SST model). However, here unsteady simulations are performed, since the steady ones were found to be inaccurate in predicting details of the flow (e.g., the secondary outlet of the pump). The time step was adjusted to the different rotor speeds to obtain a 2° rotation of the blades per time step. The simulations were run during 40 complete rotations of the pump, so the flow has sufficient time to converge all around the box. The fact was studied by monitoring the time-averaged velocity magnitudes of the flow at the outlet of the pump for different periods of the simulation (see Figure 63-a). Considering this figure, the profiles of the 40th and 50th rotations are almost equal. So, the flow tends

to be a constant behavior after the 40th rotation. The same approach was followed to find the optimum value for the maximum iterations per time step (see Figure 63-b). In this study, the velocity magnitudes on the same line were probed at the end of the 40th rotation. The results demonstrate that the optimum value for this parameter is 30. In all simulations, the convergence criteria were offset to 10^{-5} for all residuals, the same as our studies for the FDA pump benchmark.

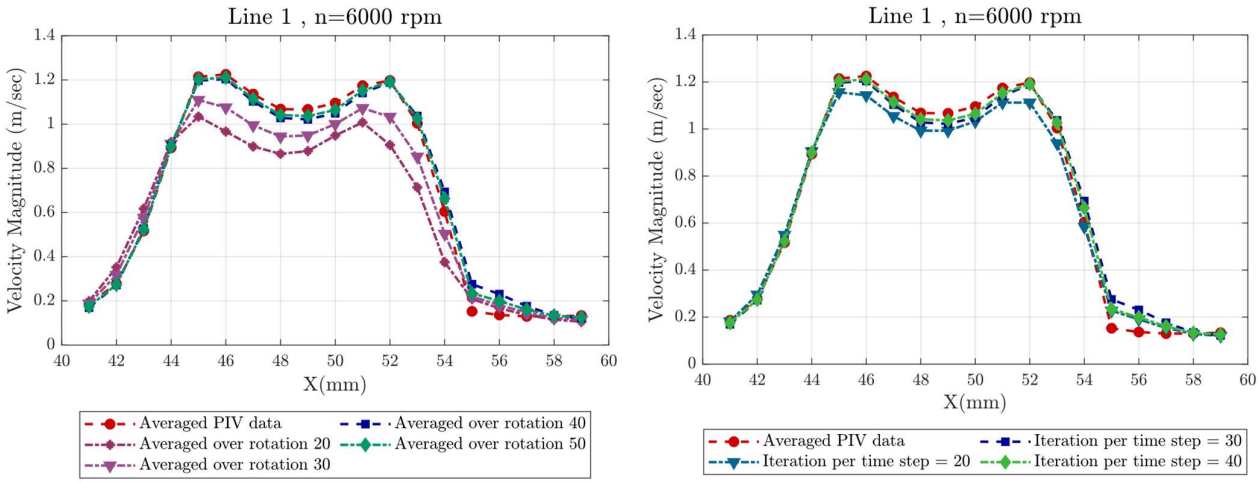

(a) (b)

Figure 63. a) Velocity magnitude is probed on Line 1, positioned at the outlet of the pump (see Figure 76), for a specific operating condition (n=6000 rpm) of the pump using the time-averaged data through different periods of the ICOMS rotation. b) Same profiles are calculated over the 40th iteration to find the optimum value for the iteration number per time step.

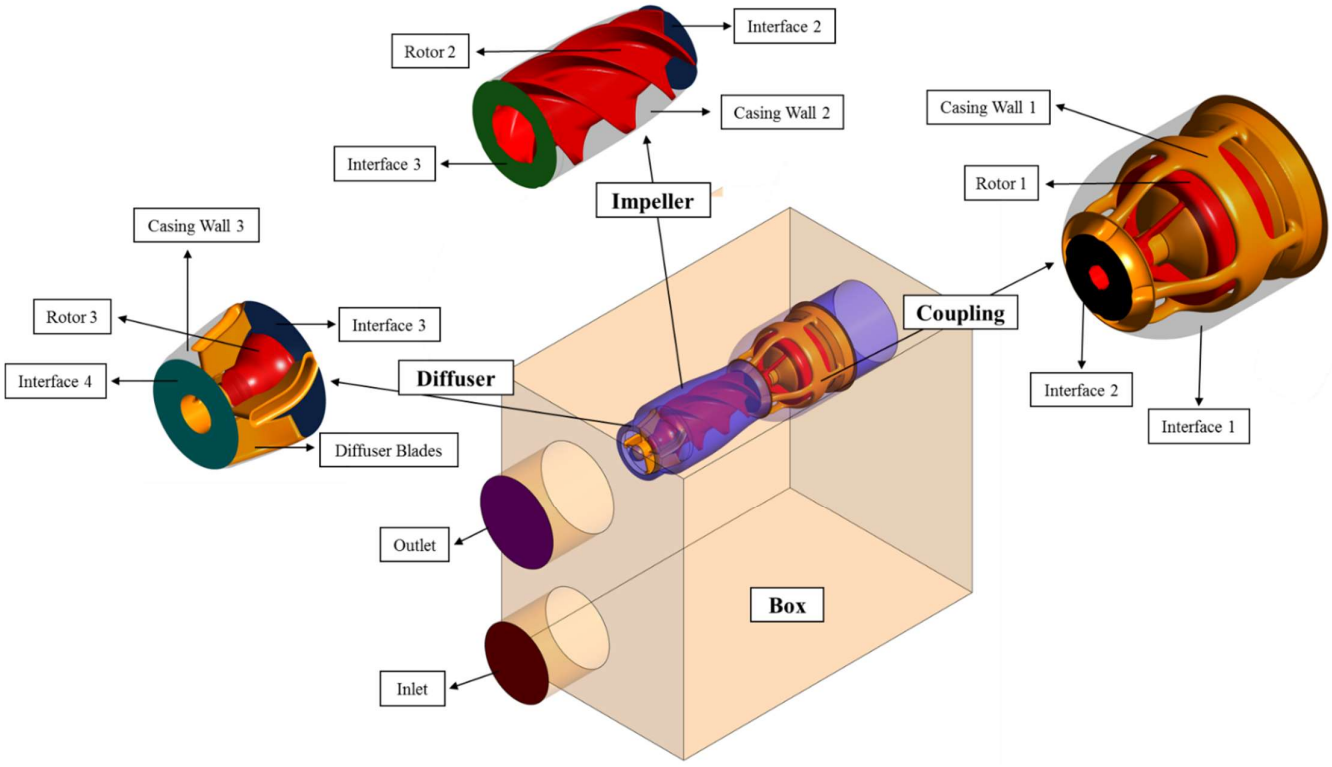

Figure 64. Boundary conditions for the PIV simulations of the FineHeart blood pump.

For these simulations, the geometry of the ICOMS inside the box is separated into four subdomains: The box, the coupling, the impeller, and the diffuser (see Figure 64). Three subdomains (The box, the coupling, and the diffuser) are considered stationary parts; While the impeller subdomain is set to be a rotating one equal to the rotational speed of the pump. The Multiple Reference Frames (MRF) methodology is implanted for considering the impeller as the rotating region. So, interfaces 2 and 3 are adjusted as "Transient Rotor-Stator" interfaces in Ansys CFX to transform the data from the stationary parts and the impeller region. Other interfaces (interface 1 and interface 4) are modeled with the "General Grid Interface (GGI)" option in the software.

In this setup, the rotational speed of the pump is applied with different strategies for each part. As mentioned above, the rotation of the impeller is set to its subdomain. In this case, the casing's internal wall is considered a counter-rotating wall (Casing Wall 2). On the other hand, the rotation of the rotor walls in the diffuser (Rotor 3) as well as coupling rotating walls (Rotor 1) are applied with a rotational speed equal to the impeller's one. At this point, it is important to note that all other walls, including walls surrounding the box, are assumed as a no-slip condition.

The inlet boundary condition is applied as static pressure with a uniform value of 30 mm Hg. On the other side, the outlet surface is adjusted with a flow rate respecting the PIV measurement condition (0.5 to 3 lpm). The detailed specification of all boundary conditions is indicated in Table 16. As mentioned in this table, the operating points of the pump are selected to be consistent with the experimental measurements.

Table 16. The detailed specification for the PIV simulations set up.

Boundary	**Location**	**Type**	**Value**
Inlet	Inlet	Static Pressure	30 mm Hg
Outlet	Outlet	Flow rate	Dependent on the condition
Wall	Box walls Casing wall 1 Rotor 2 Casing wall 3 Diffuser blades	Wall	No slip
Counter Rotating Wall	Casing wall 2	Counter Rotating Wall	No slip
Rotating Wall	Rotor 1 Rotor 3	Rotating Wall	Dependent on the rotational speed
Interface	Interface 1 Interface 4	GGI	-
	Interface 2 Interface 3	Transient Rotor-Stator	-

The operational conditions of the ICOMS inside the PIV box are plotted in Figure 65. Flow rate against rotational speed, using the PIV measurements with the ICOMS operated inside the box. In fact, the curve shows how much flow rate is generated as the rotational speed of the ICOMS increases, while keeping the pressure loss minimum in the test loop (control valves are open 100%). As shown in this figure, there is a linear relationship between the two parameters. The values of this plot are used to select the flow rate in the simulations for each operating point.

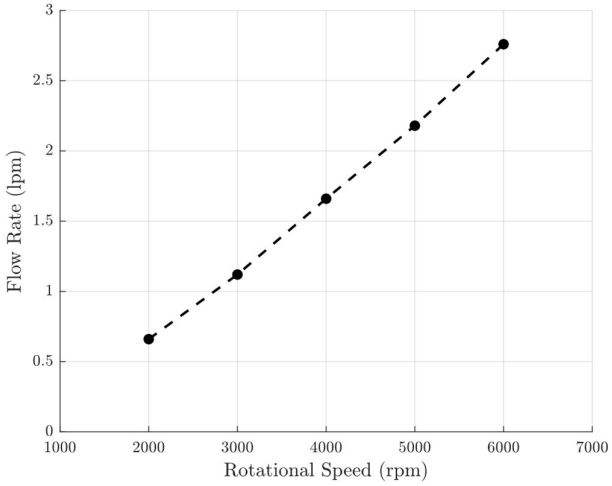

Figure 65. Flow rate against rotational speed, using the PIV measurements with the ICOMS operated inside the box.

c) Hemolysis tests

As mentioned in section 1.4.3, hemolysis tests were performed for the ICOMS to validate its biocompatibility performance. According to the testing geometrical conditions, hemolysis tests were conducted in the same box as the PIV measurements (see Figure 62. a) Positioning of the pump inside the PIV box for the CFD simulations. b) Actual position of the pump inside the PIV box in the experiments.). Therefore, the numerical framework used to predict the hemodynamic aspect of the blood flow are similar to the previous ones, but the hemolysis model was added to the solver to be resolved in conjunction with the hemodynamic model.

In terms of the operating condition, in the hemolysis tests the ICOMS is operated at a pulsatile rotational speed, while for the PIV test bench, it was in continuous mode (Figure 66). The pulsatile mode enables the pre-clinical measurements to be more relevant to the in vivo ones, as the pump is expected to operate synchronously with the natural blood flow inside the cardiac system. Figure 66 indicates the operation conditions of the ICOMS and different configurations for the hemolysis tests. In this case, there are two different modes of operation: TD high flow, and TD low flow. The “TD high flow” configuration is designed to represent the normal mode of the ICOMS, while it is rotating in synchronization with the left ventricle functionality. On the other side, the “TD low flow” profile is designed to represent the performance of the pump in safety mode. The condition where pump faces an urgent problem and starts to operate at low-speed rotational speeds.

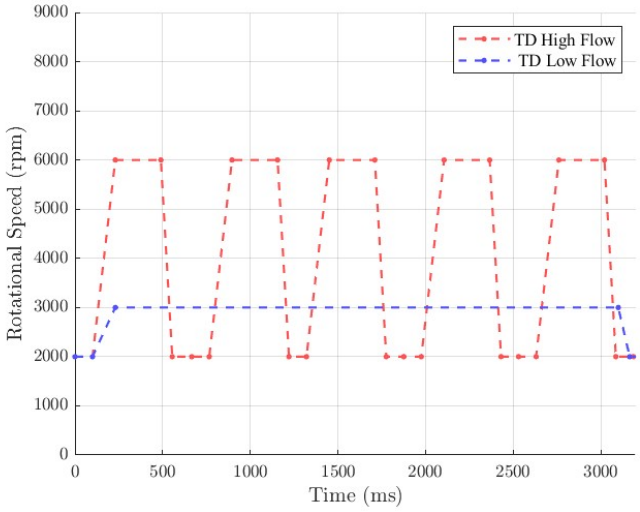

Figure 66. Operational conditions and different configurations of the ICOMS for the hemolysis tests.

In the hemolysis simulations of the ICOMS, the approach and the geometry will be identical to the setup of the PIV simulations. For the hemolysis aspects, the standard transport form of the power law equation will be added to the simulation using the porcine's blood coefficients provided by Ding et al. [18] (see

Table 5). In addition, three different convergence criteria (10^{-5}, 10^{-6}, and 10^{-7}) are successively applied to all equations to check with convergence level is required. The results of the convergence level study are presented in section 2.4.3.c).

2.4.2. Grid Generation

a) Correlation loop simulations

As mentioned in section 2.4.1, for the correlation loop simulations the geometry is limited to the hydraulic parts of the ICOMS. In this case of simulations, a structured mesh is generated using Ansys Turbogrid, a meshing module of the Ansys software specialized in turbomachinery meshing. As shown by surface imprints in Figure 67, the mesh for each of the three sets of blades has been created separately and assembled in the solver (This will enable us to focus on each part and to define better topologies for the process). More concentrations of cells are applied to the critical regions like the hub and the shroud clearances. In addition, boundary layer meshing is set to all walls with specific first layer thickness and expansion rates.

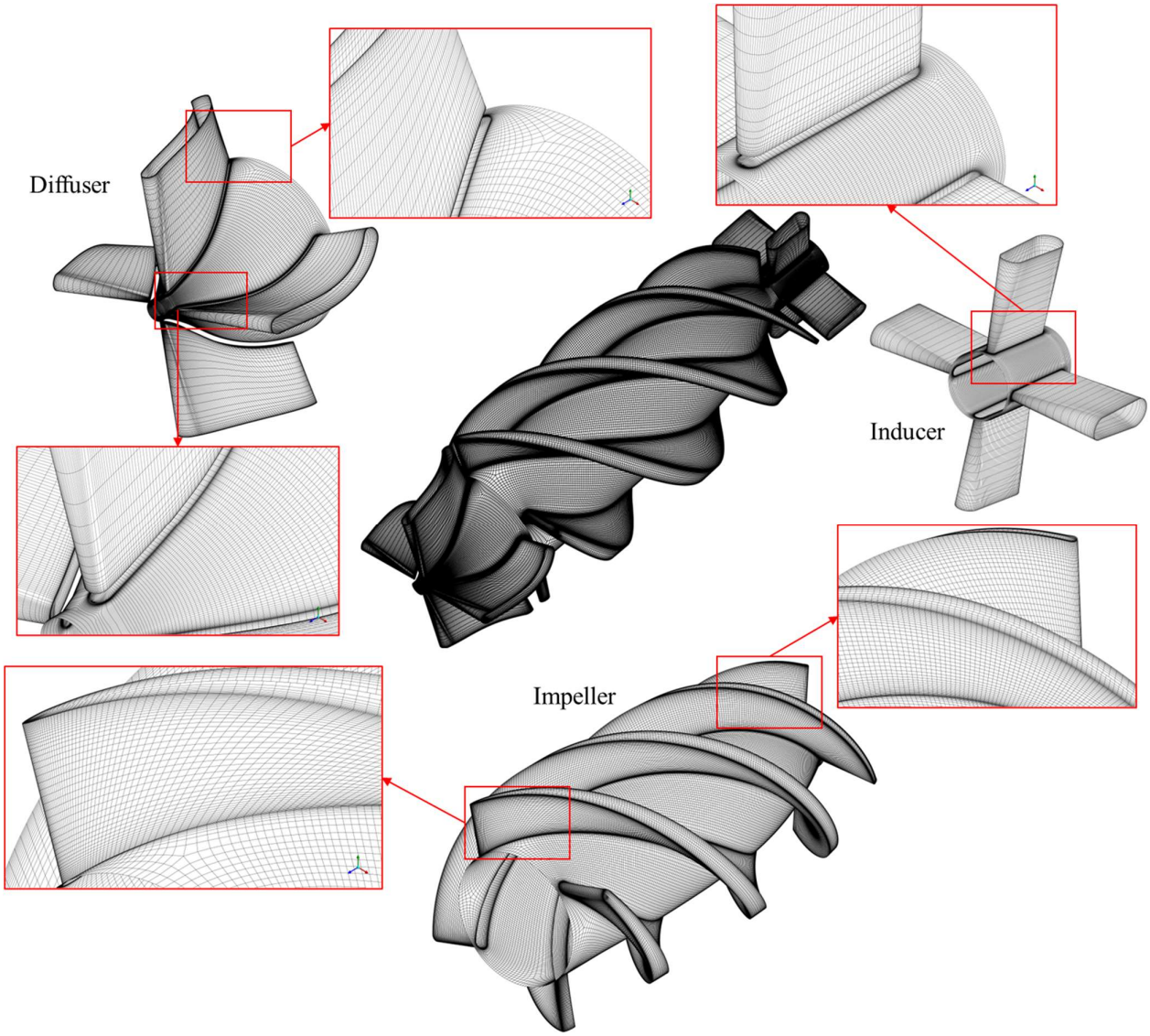

Figure 67. Surface imprints of the generated mesh for the hydraulic parts of the ICOMS.

To check the dependency of the results on the mesh, five different grids have been generated, as indicated in Table 14. To investigate this specific point, simulations were carried out for a specific operating point of the ICOMS with n=6000 rpm and Q=5 lpm. This point is selected as it is the nominal operating point of the pump in real conditions of use (inside the animal/human body). The pressure elevation generated by the pump is calculated and compared with the experimental data for each mesh (see Figure 68, left). The relative difference with the experimental data $e(\%) = \frac{|P_{EXP} - P_{CFD}|}{P_{EXP}} \times 100$) is also plotted in Figure 67 (right).

Table 17. Properties of the five different meshes generated by Ansys Turbogrid for the ICOMS hydraulic system for the correlation loop simulations.

Index	Parameter	Subdomain	Value				
			M1	M2	M3	M4	M5
P1	Max node size (mm)	Inducer	0.20	0.15	0.10	0.04	0.02
P3	First layer offset (mm)		0.050	0.020	0.010	0.005	0.001
P4	Maximum Expansion rate		1.30	1.20	1.10	1.07	1.05
P5	Max node size (mm)	Impeller	0.20	0.15	0.10	0.04	0.02
P7	First layer offset (mm)		0.050	0.020	0.010	0.005	0.001
P8	Maximum Expansion rate		1.30	1.20	1.10	1.07	1.05
P9	Max node size (mm)	Diffuser	0.20	0.15	0.10	0.04	0.02
P11	First layer offset (mm)		0.050	0.020	0.010	0.005	0.001
P12	Maximum Expansion rate		1.30	1.20	1.10	1.07	1.05
Total number of cells ($\times 10^6$)		All domains	0.12	0.33	0.76	1.56	2.23
Maximum y^+			14.6	8.7	5.3	2.6	1.3

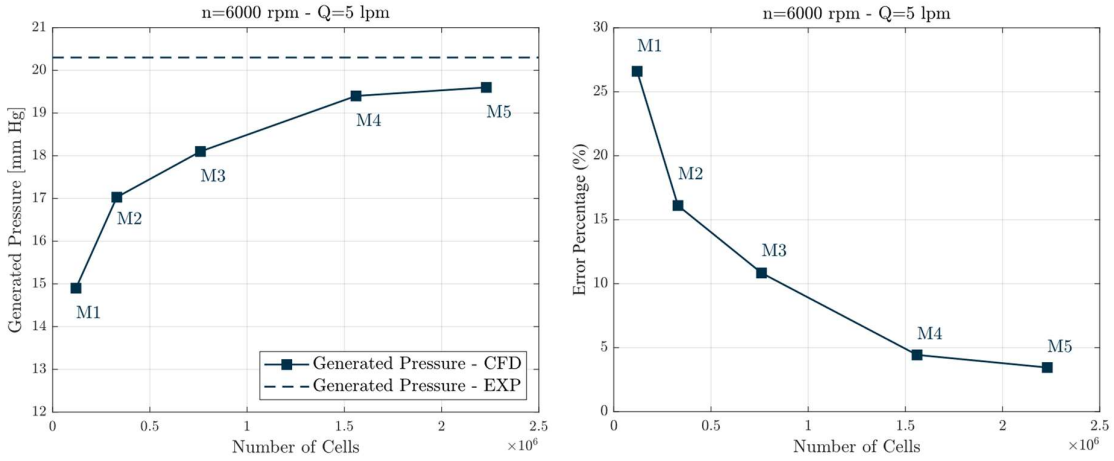

Figure 68. Left: Predicted pressure elevation in the pump according to the number of cells for the five different meshes (n=6000 rpm and Q=5 lpm). Right: Relative difference with the experimental values ($e(\%) = \frac{|P_{EXP} - P_{CFD}|}{P_{EXP}} \times 100$).

As shown in Figure 68, a large influence of the mesh size is observed from grid M1 up to grid M4. However, the difference with the experimental value tends to decrease with the number of cells, and eventually a good convergence is obtained between meshes M4 and M5. Both of them provide a pressure elevation in good agreement with the experiments, with a relative difference lower than 5%. So, hereafter the M4 is chosen to perform rest of the correlation loop simulations.

b) PIV and hemolysis simulations

For this stage of the numerical analysis, a tetrahedral mesh was created for the ICOMS inside the box (as shown in Figure 62) using the same process as for the FDA pump benchmark. The Ansys Meshing was used to generate unstructured grids, considering the complexity of the ICOMS geometry. It is important to note that the mesh here is regenerated for inside of the pump using the same methodology as the FDA pump benchmark.

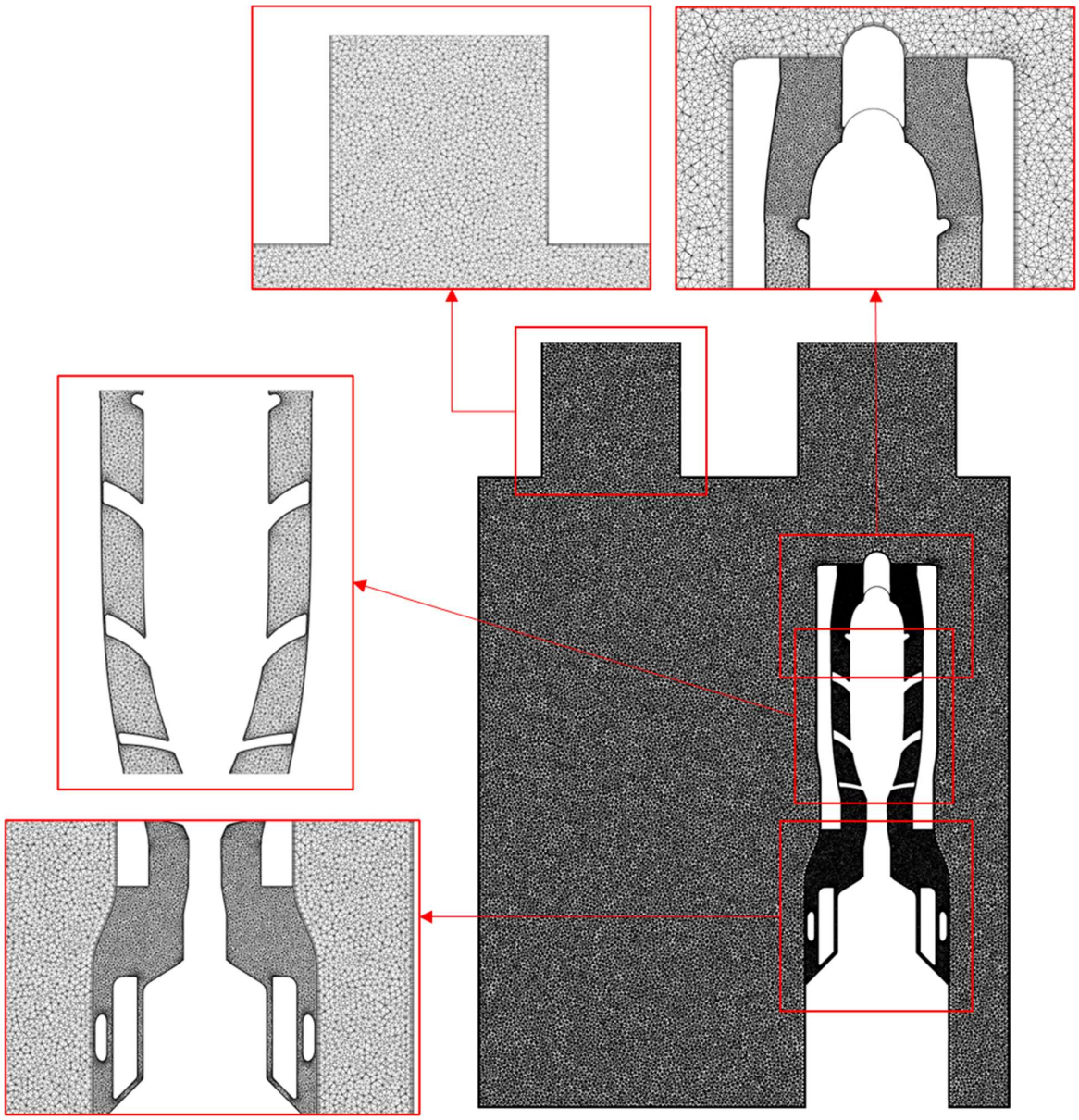

Figure 69. Generated mesh for the FineHeart blood pump test case inside the PIV box.

A mesh study was conducted as well, to enhance the result reliability and optimize the calculation time. This study is particularly important for the ICOMS simulation since the calculation for this test case is more time-consuming than the two other cases in the FDA benchmark. Table 18 presents the

properties of the five different meshes generated for the PIV and hemolysis simulations. The accuracy of each mesh was evaluated by monitoring the axial velocity at the center of Line 3 (see Figure 76) and the modified index of hemolysis (MIH). It should be noted that these initial simulations were performed for a specific operating condition of the ICOMS (TD High flow) with a rotational speed of n=6000 rpm. More detailed views of the generated mesh for this test case are provided in section 4.3.

Table 18. Properties of the five different meshes generated for the FineHeart PIV and hemolysis tests simulations.

Index	Parameter	Subdomain	Value				
			M1	M2	M3	M4	M5
P1	Max Tet size (mm)	Box	2.00	1.50	1.00	0.75	0.50
P2	Min Tet size (mm)		1.20	0.80	0.40	0.20	0.10
P3	First layer thickness (mm)		0.80	0.40	0.20	0.10	0.05
P4	Boundary layer growing ratio		1.40	1.30	1.25	1.20	1.15
P5	Max Tet size (mm)	Coupling	0.8	0.6	0.4	0.2	0.1
P6	Min Tet size (mm)		0.10	0.08	0.06	0.04	0.02
P7	First layer thickness (mm)		0.100	0.075	0.050	0.025	0.010
P8	Boundary layer growing ratio		1.20	1.15	1.10	1.07	1.05
P9	Max Tet size (mm)	Impeller	0.8	0.6	0.4	0.2	0.1
P10	Min Tet size (mm)		0.10	0.08	0.06	0.04	0.02
P11	First layer thickness (mm)		0.100	0.075	0.050	0.025	0.01
P12	Boundary layer growing ratio		1.30	1.20	1.10	1.07	1.05
P13	Max Tet size (mm)	Diffuser	0.8	0.6	0.4	0.2	0.1
P14	Min Tet size (mm)		0.10	0.08	0.06	0.04	0.02
P15	First layer thickness (mm)		0.100	0.075	0.050	0.025	0.01
P16	Boundary layer growing ratio		1.30	1.20	1.10	1.07	1.05
Total number of cells ($\times 10^6$)		All domains	2.1	6.2	12.4	21.7	35.3

Figure 70 indicates the results of the mesh study, considering both the hemodynamic and hemolysis aspects. The values of velocity at the center of the Line 3 and modified index of hemolysis and relevant errors is plotted for each of the meshes. Considering the outcomes, it is clear that the M4 mesh results in the optimum values for both the computation time and accuracy. Using a smaller number of cells (M3), the accuracy of the hemolysis prediction is dropped from 4% to 8%. While higher number of cells

(M5) doesn't improve the accuracy meaningfully. So, hereafter the selected mesh (M4) is used for the rest of the simulations.

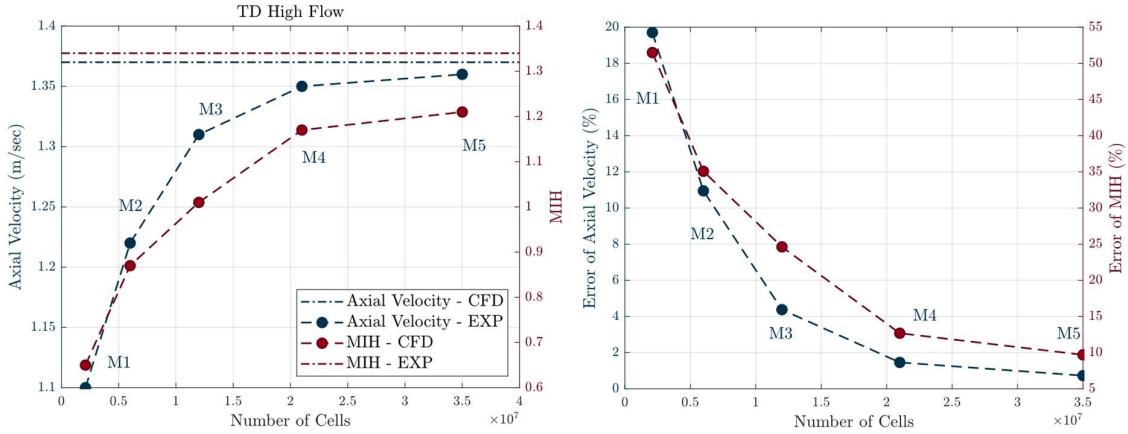

Figure 70. Left: Values of predicted axial velocity and MIH for the five different meshes (TD High flow with n=6000 rpm). Right: Error of calculated axial velocity and MIH considering the value of the experimental data as the reference ($e(\%) = \frac{|V_{EXP} - V_{CFD}|}{V_{EXP}} \times 100$).

2.4.3. Results

To ensure a dependable hemolysis simulation, the first step involves validating the simulated flow field in terms of hemodynamics. To achieve this, the hemodynamic features of the ICOMS pump were studied using two laboratory tests: correlation loop measurements and PIV velocimeters. The correlation loop is an experimental technique that measures the pump's performance, while the PIV tool helps study the flow pattern around the pump. This section validates the hemodynamic simulation method using the results from both experiments, both from quantitative and qualitative perspectives.

a) Correlation loop tests

The numerical results were initially validated against the performance diagrams of the pump, obtained from the correlation loop. Numerical simulations were performed for a broad range of rotational speeds (2000 to 7000 rpm) and flow rates (0.5 to 7 lpm). The ICOMS was characterized by an H-Q curve, which illustrates the flow rate (in l/min) and the total pressure difference between the inlet and outlet of the pump ($\Delta P = P_{outlet} - P_{inlet}$ in Figure 60, given in mmHg). The H-Q curve was generated using numerical tools and compared to experimental measurements (as seen in Figure 71). The figure shows that an increase in rotational speed results in a higher flow rate and pressure capacity for the ICOMS. Moreover, there is a linear correlation between the flow rate and generated pressure, with a negative slope, which is conventional for an axial blood pump, is evident in both numerical and experimental profiles.

Regarding Figure 71, the second significant observation is that the numerical tool is precise enough to predict the trend of the experimental curves. In this context, the errors of the simulation results for

each point were calculated using the formula: $e(\%) = \frac{|X_{EXP} - X_{CFD}|}{X_{EXP}} \times 100$. The calculated error was then plotted against the flow rate, as illustrated in Figure 72. This figure shows that, in most cases, except for n=2000 rpm and some particular operating points, the error of the numerical simulation is below 6 percent. Furthermore, for roughly two-thirds of the results, the error is under 4 percent.

In addition, the comparison between numerical and experimental results was also made for the torque, which directly impacts the energy consumption of the ICOMS. The torque was calculated using the formula $T = \int PrdA$, and the numerical simulations were carried out for the same operating configurations as the previous comparison. Figure 73 shows the comparison between the numerical and experimental results for the torque. As expected, there is a linear correlation between the torque and the flow rate and increasing the rotational speed leads to higher torque values.

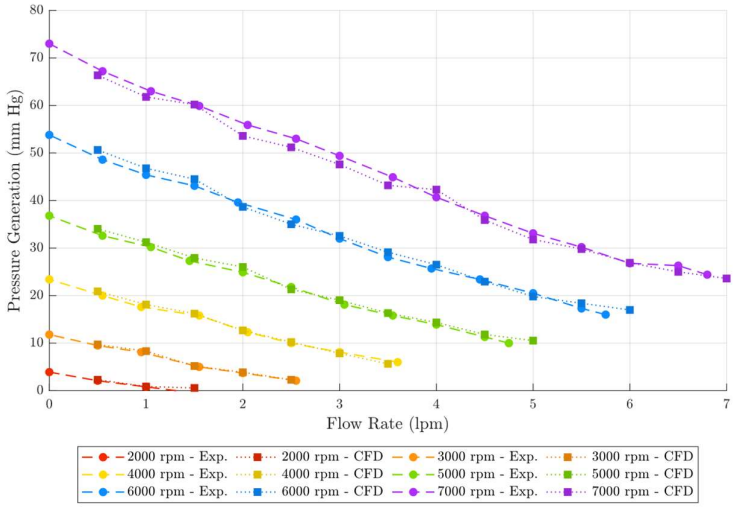

Figure 71. The generated pressure of the ICOMS in different rotational speeds and flow rates was compared between the CFD results and experimental measurements provided by FineHeart.

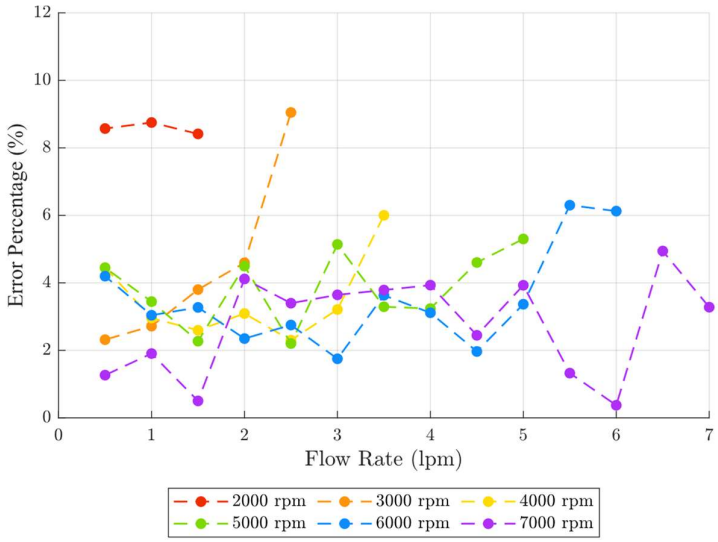

Figure 72. The error of the numerical results for the generated pressure at each operating point was calculated using the formula: $e(\%) = \frac{|X_{EXP} - X_{CFD}|}{X_{EXP}} \times 100$.

The error of calculation was also analyzed and plotted in Figure 74. The results show that the applied numerical method produced convincing outcomes with very low errors (less than 6% for all conditions except one).

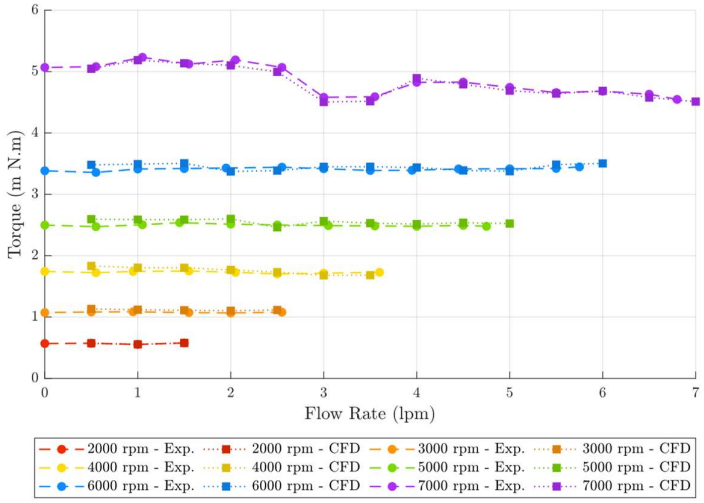

Figure 73. A comparison was made between the torque generated by the ICOMS at various rotational speeds and flow rates, as measured experimentally by FineHeart, and the torque values predicted by the CFD simulations.

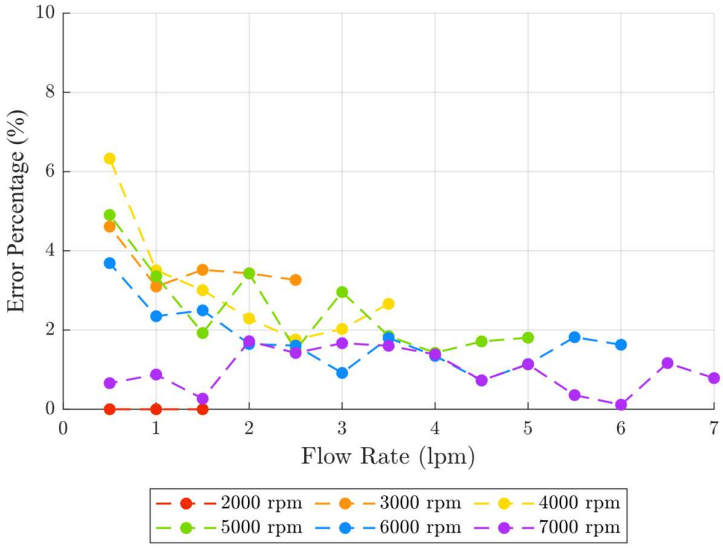

Figure 74. The errors in the numerical results for the calculated torque corresponding to each of the operating points were also analyzed. These errors were calculated using the formula: $e(\%) = \frac{|X_{EXP} - X_{CFD}|}{X_{EXP}} \times 100$.

b) Particle Image Velocimetry (PIV) tests

The PIV (Particle Image Velocimetry) tool is used to measure the velocity field in a plane illuminated with a laser light sheet, by calculating the average motion of particles between two frames separated by a very small time. It was performed here inside a box that represents the ventricle's environment, with the ICOMS pump inserted in it (as shown in Figure 62). The laser light sheets illuminate the liquid in

the box outside from the pump, so the PIV measurements provide the velocity field outside from the pump only. In this section, the CFD-based results calculated in the same configuration are compared with the experimental data obtained by FineHeart. To provide the results in a standard and comparable format, Matlab software was used for post-processing. Figure 75 displays a sample processed view of the PIV-measured flow pattern for a specific operating condition of the pump (n=6000 rpm). The fluid flow is sucked into the pump with a relatively lower velocity magnitude (indicated by the red line arrow). Due to the impeller's high rotational speed, the fluid is pushed out of the outlet towards the outlet of the box (indicated by the black line arrow). In this region, a small percentage of the flow generates a rotating vortex that never disappears (indicated by the purple line arrow). Additionally, there is a secondary outlet near the coupling that fluctuates over time, and its direction is generally dependent on the rotational speed (indicated by the green line arrow). The simulations are compared hereafter to the velocity field obtained by PIV, in these critical regions of the flow.

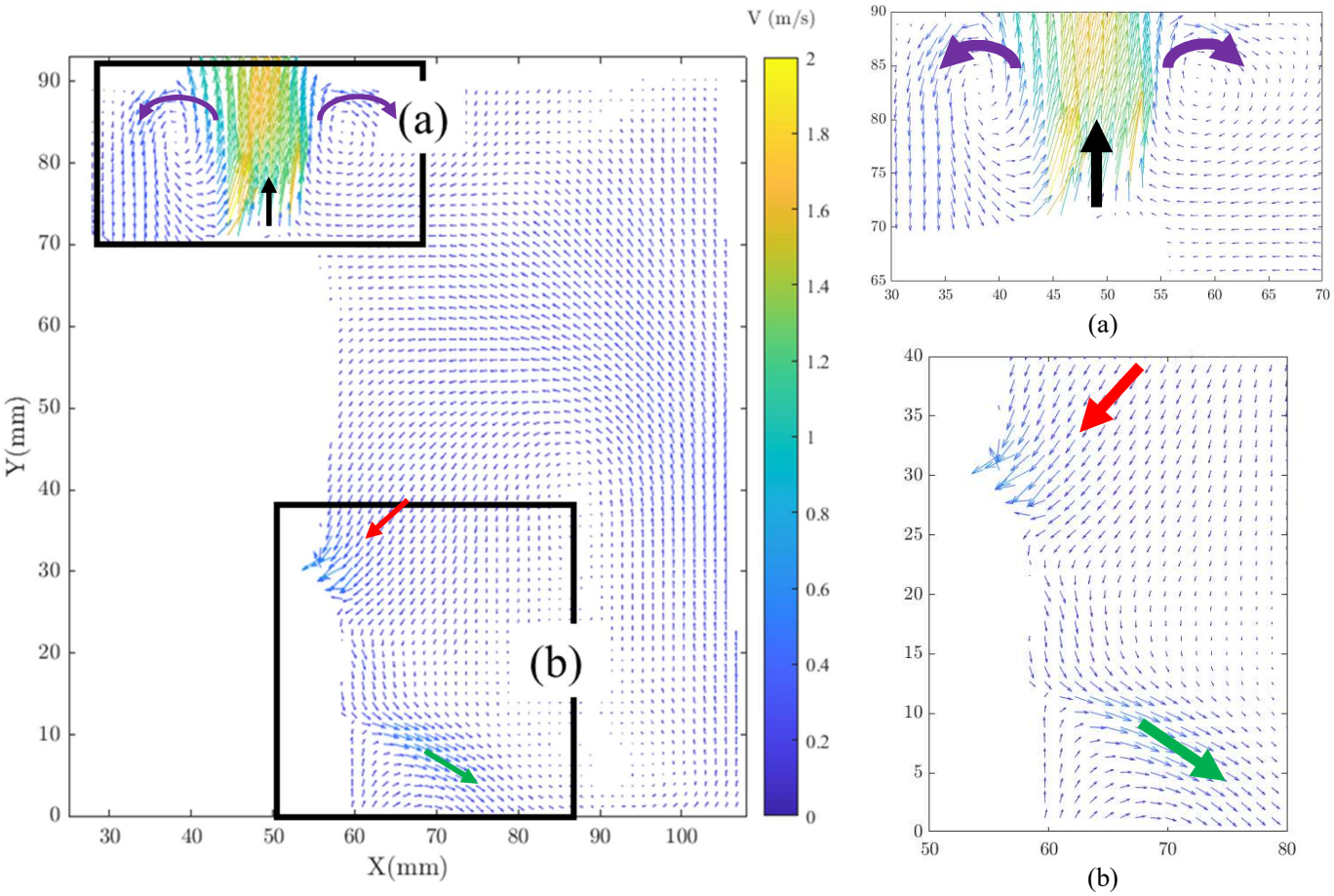

Figure 75. The PIV tool measures the 2D surface vectors of the flow velocity while the ICOMS is operating at 6000 rpm inside the PIV box shown in Figure 62.

Five lines have been identified in the mid-plane of the box (as shown in Figure 76). Velocity magnitude profiles were extracted from these lines for both the experimental and numerical results. Lines L1, L2, and L3 were chosen to quantify the velocity at the pump outlet where the highest velocity

gradients were observed. Line L4 was positioned at the pump inlet region with a rotation angle of α=-45° against the x-axis. Lastly, Line L5 was specified at an angle of α=45° against the same axis in front of the secondary pump outlet.

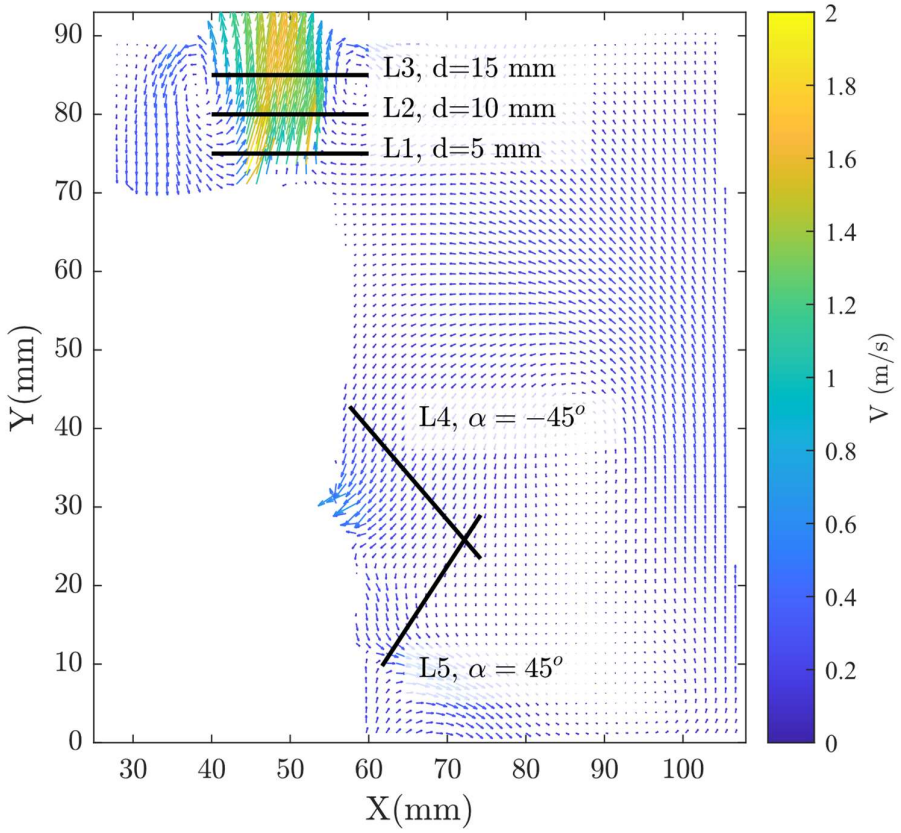

Figure 76. Specified lines to probe velocity magnitudes in the PIV box.

Figure 77-a shows a comparison between PIV measurements and CFD results for Line 1, based on time-averaged PIV data, time-averaged CFD results, and instantaneous CFD profiles in a single graph. The reason for comparing the averaged CFD results with the PIV outcomes is that the velocity components for the PIV measurements have been averaged over numerous pairs of images (300 pairs). Hence, to obtain a similar approach, the CFD velocity profiles were also averaged, but for a period of the latest 10 time steps. To summarize, the reason why averaged CFD results were compared with the PIV outcomes for Line 1 is that the PIV measurements themselves were averaged over a period of time to get more reliable results, and the CFD instantaneous profiles showed clear fluctuations in the velocity field. Averaging the CFD profiles helped to eliminate these fluctuations and make reliable comparisons with the PIV data. The numerical data are found in very good agreement with the experiments. Figure 77-b shows that the maximum relative difference between CFD and measurements is about 20%, while for most of the probe points, it is lower than 10%, which is considered acceptable. A similar observation can be drawn for Line 2 and Line 3 based on the information presented in Figure 78 and Figure 79, respectively. In both instances, the maximum error percentage is nearly 20%. However, the agreement is generally better for Line 3 (Figure 79-b).

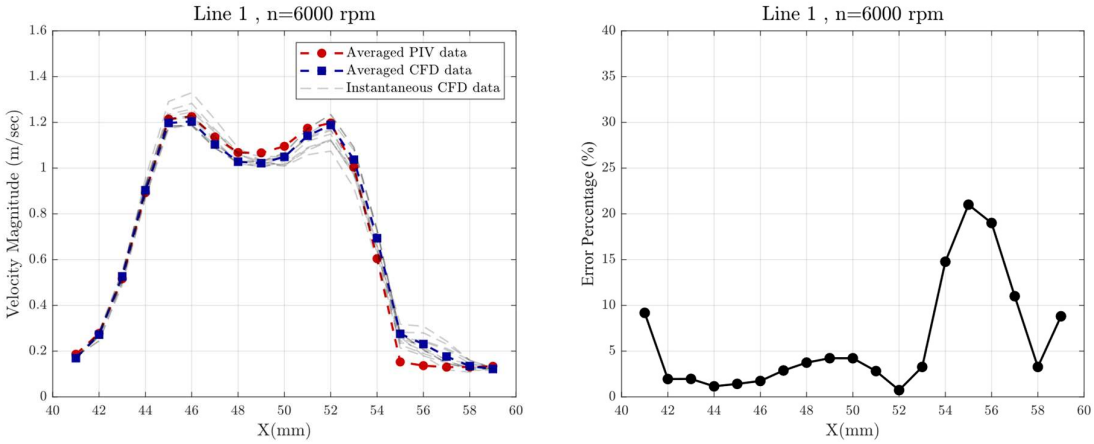

(a) (b)

Figure 77. Comparison between PIV measurements and CFD results for Line 1 (n=6000 rpm). a) Averaged profiles of the velocity magnitudes. b) Error percentage of the CFD calculations for the same profiles.

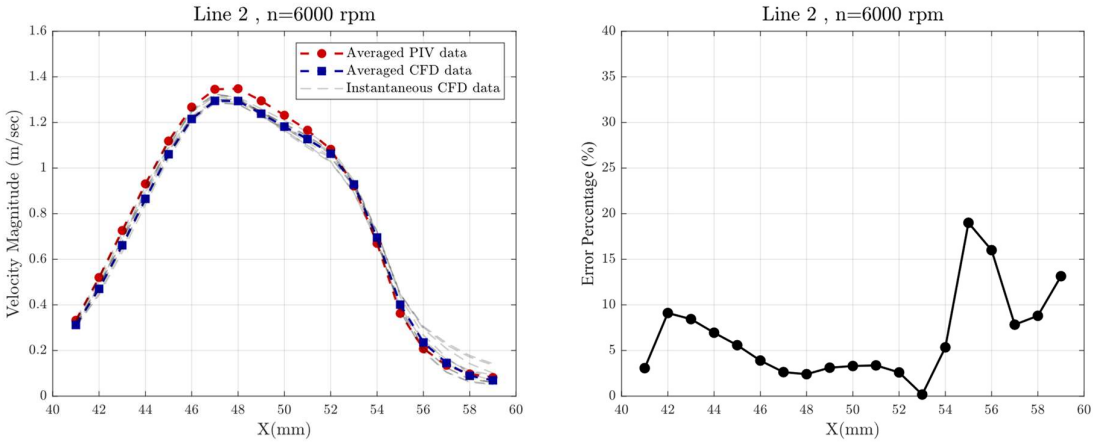

(a) (b)

Figure 78. Comparison between PIV measurements and CFD results for Line 2 (n=6000 rpm). a) Averaged profiles of the velocity magnitudes. b) Error percentage of the CFD calculations for the same profiles.

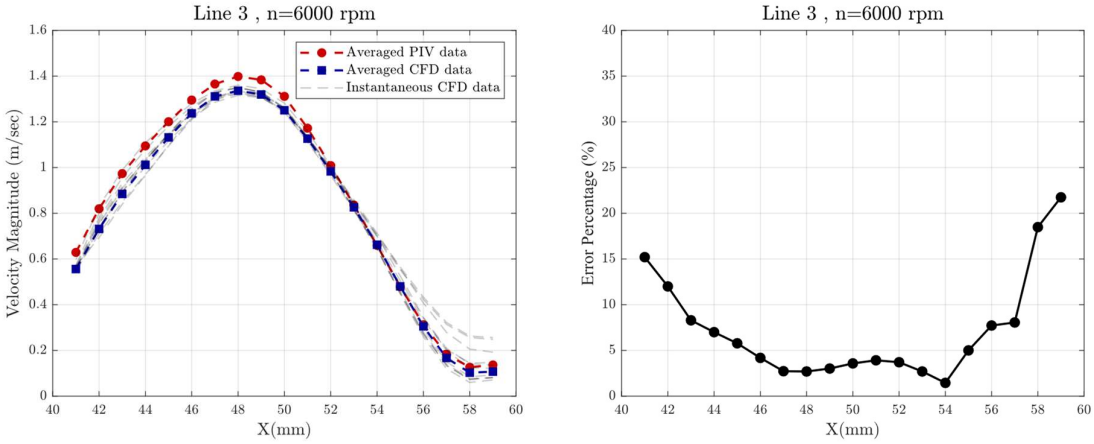

(a) (b)

Figure 79. Comparison between PIV measurements and CFD results for Line 3 (n=6000 rpm). a) Averaged profiles of the velocity magnitudes. b) Error percentage of the CFD calculations for the same profiles.

The same conclusion can be drawn for two other lines, Line 4 and Line 5, based on Figure 80-a and Figure 81-a, which display the velocity magnitude against the x-axis for these lines. These figures show that the CFD calculation reproduces the trend obtained in the PIV measurements, but it consistently underestimates the velocity magnitude at both locations. Figure 80-b and Figure 81-b display the error percentage of the calculated velocity profiles. For Line 4, the error rate is illustrated by a semi-linear curve that remains below 13%. In contrast, the error for Line 5 is somewhat higher, at approximately 15%.

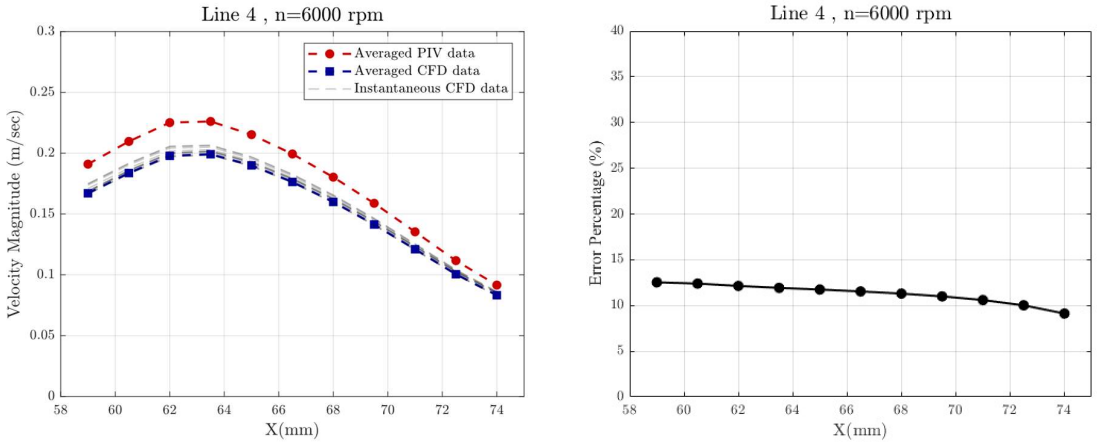

(a) (b)

Figure 80. Comparison between PIV measurements and CFD results for Line 4 (n=6000 rpm). a) Averaged profiles of the velocity magnitudes. b) Error percentage of the CFD calculations for the same profiles.

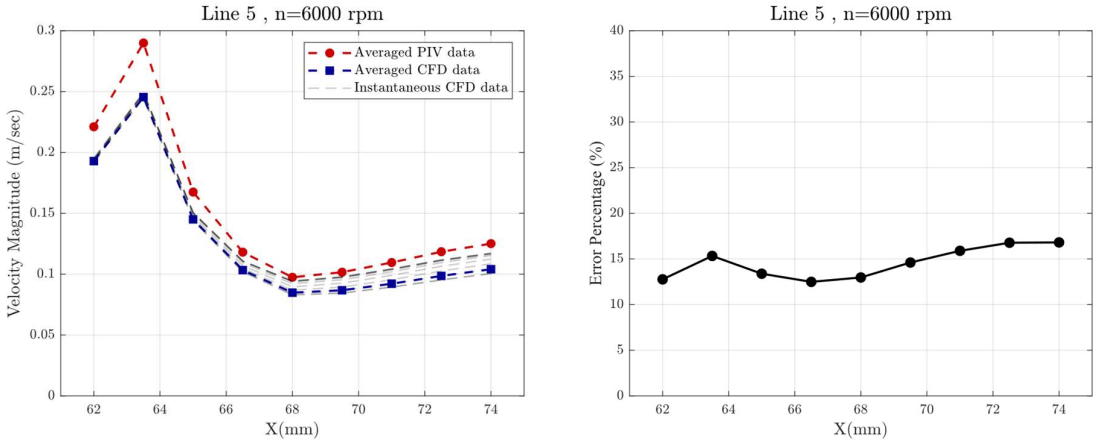

(a) (b)

Figure 81. Comparison between PIV measurements and CFD results for Line 5 (n=6000 rpm). a) Averaged profiles of the velocity magnitudes. b) Error percentage of the CFD calculations for the same profiles.

Table 19 indicates the average error for each of the five lines. For two of the lines (Line 2 and Line 3), the average error is lower than 10% which is acceptable. Moreover, for the other lines, the percentage of error is between 10% to 15% which is still reasonably accurate. A similar approach has been followed for the n=5000 rpm. More information is provided in section 4.4.

Table 19. The average error of CFD calculation compared with the PIV experimental measurements probed on each line.

Probe Location	Average Error (%)
Line 1	10.56
Line 2	6.38
Line 3	6.66
Line 4	11.29
Line 5	14.55

Based on the comparisons presented in this section, it is clear that the numerical framework used here is sufficiently accurate to be used as an initial step of the hemolysis simulations. Next, the procedure of the hemolysis simulations of the ICOMS is provided.

c) Hemolysis

As stated in section 2.4.1, the ICOMS underwent hemolysis tests inside a solid box (as shown in Figure 30). FineHeart conducted hemolysis experiments on the ICOMS under two operating conditions: "TD High Flow" and "TD Low Flow." The experiments consisted in measuring the released hemoglobin in the blood flow at various time intervals, with a total experiment duration of 360 minutes (60 minutes per interval). Table 20 displays the measured free hemoglobin at different time during the experiments. It should be noted that the hemolysis experiments were repeated three times, denoted by "A," "B," and "C" in the table. Therefore, a mean value has been added to the table as well.

Table 20. Measured Free Hemoglobin through hemolysis tests for two operating conditions of the ICOMS ("TD High Flow" and "TD Low Flow") with three repetitions "A", "B", and "C".

	t=0 min			t=60 min			t=120 min			t=180 min		
	No.	value	mean	No.	value	mean	No.	value	mean	No.	value	mean
TD High Flow	0A	16.68	16.86	1A	18.66	18.81	2A	22.83	22.31	3A	24.51	24.51
	0B	17.14		1B	18.99		2B	22.39		3B	24.22	
	0C	16.77		1C	18.77		2C	21.72		3C	24.81	
TD Low Flow	0A	17.03	16.86	1A	16.33	16.28	2A	18.25	18.36	3A	22.17	22.08
	0B	16.99		1B	16.14		2B	18.34		3B	21.78	
	0C	16.57		1C	16.36		2C	18.5		3C	22.3	
	t=240 min			t=300 min			t=360 min					
	No.	value	mean	No.	value	mean	No.	value	mean			
TD High Flow	4A	26.67	26.46	5A	31.24	31.07	6A	33.76	22.31			
	4B	26.49		5B	31.08		6B	34.92				
	4C	26.21		5C	30.88		6C	34.87				
TD Low Flow	4A	24.31	23.92	5A	24.85	24.89	6A	27.43	18.36			
	4B	23.71		5B	24.78		6B	26.86				
	4C	23.74		5C	25.05		6C	26.89				

Figure 82 displays the results of an experiment where free hemoglobin levels were measured over time for the two different operating conditions, referred to as "TD High Flow" and "TD Low Flow". The green line, which represents higher rotational speeds within this condition, shows a steeper slope than the other line, indicating a greater increase in free hemoglobin levels over time.

The fact that the two lines start from similar levels of free hemoglobin (about 15 mg/dL) suggests that the initial conditions were the same for both operating conditions. As time progresses, however, the difference between the two lines increases, with the green line showing significantly higher levels of free hemoglobin by the end of the experiment (about 7-8 mg/dL higher). The objective of this part of the study is to identify the sources of this difference between the two flow configurations.

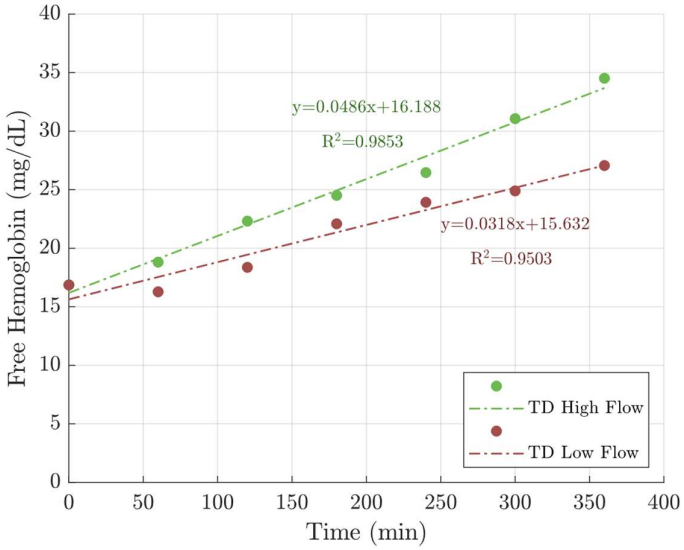

Figure 82. Free hemoglobin against time for two operating conditions of the ICOMS based on the mean probed data provided by Table 20.

The simulations were carried out using both configurations, as stated earlier. First, the pump was simulated under the "TD High flow" condition with higher rotational speed. The calculated MIH values were then validated against the experimental data from FineHeart. To evaluate the required convergence level, the calculations were repeated with different convergence levels (10^{-5}, 10^{-6}, and 10^{-7}). Figure 83 shows a comparison between the instantaneous calculated MIH values at the three different convergence levels and the FineHeart experimental measurements for the "TD High flow" configuration. The experimental uncertainty range is represented by a transparent gray area on the graph. It is evident that the simulation with the highest convergence criteria ($<10^{-5}$) underestimates the MIH. However, when the convergence level is decreased down to 10^{-6}, the predicted curves fall within the acceptable range. Moreover, reducing the convergence level further (to 10^{-7}) does not result in a significant improvement in the predicted curve. It is important to note that the experimental uncertainty range was calculated

using the mathematical process outlined in section 4.1. Therefore, the value 10^{-6} was adopted as the target convergence criteria for both the "TD High flow" and the "TD low flow" simulations.

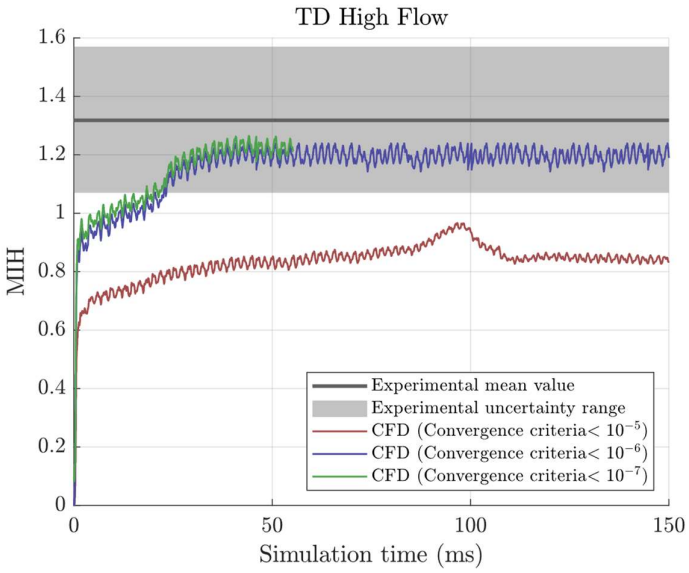

Figure 83. Comparison between calculated MIH with three different convergence levels and FineHeart experimental measurements for the "TD High flow" operating configuration.

Figure 84 shows the comparison between the calculated MIH and the experimental measurements for the "TD High flow" operating configuration. As shown, after about 300 ms of physical time of simulation the predicted MIH stabilizes to a value very close to the experimental one, with a difference much smaller than the uncertainty range.

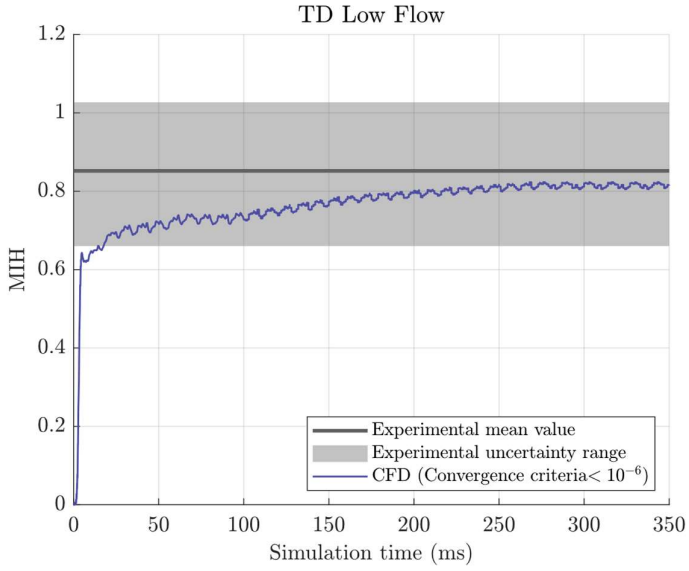

Figure 84. Comparison between calculated MIH with three different convergence levels and FineHeart experimental measurements for the "TD Low flow" operating configuration.

Considering Figure 83 and Figure 84, it is clear that it takes lots of rotations (more than 20) for the MIH curve to reach a significant convergence, regardless of operating conditions. In addition, the "TD Low Flow" requires much more simulation time, compared with the "TD High Flow". To understand this behavior, a more in-depth analysis of the results is performed hereafter.

Figure 85 indicates the maximum and average values of the equivalent stress probed in the "TD Low Flow" operating condition and for a specific period of the simulation (150ms<time<250ms). The values of Figure 85-a are processed for the stationary and rotating walls of the ICOMS, while Figure 85-b is related to the volumes of the same subdomains. Considering these two graphs, the maximum values of τ_n are observed inside the impeller as expected, while the average curves show that the diffuser is the more critical part, with higher values of stress. It suggests that the hemolysis inside the impeller is concentrated at some specific locations, while in the diffuser, it is distributed within various regions. The stress values are minimum for the coupling, and we expect to see a lower hemolysis index for this part as well.

In addition, all the curves are oscillating around a constant value (with different oscillation magnitudes), which means that the τ_n distribution inside the pump is well converged during this period of time.

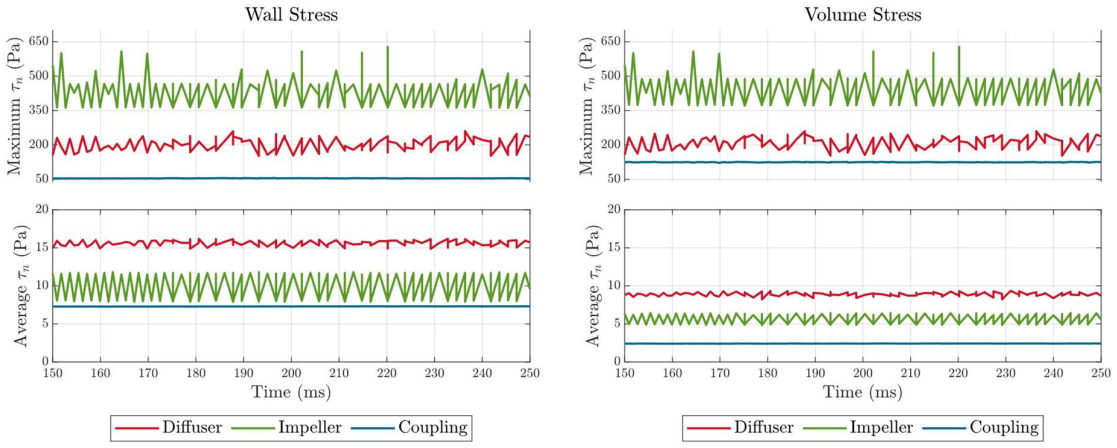

Figure 85. a) Maximum and averaged values of the τ_n probed on the walls of the ICOMS hydraulic parts at a specific time of the simulation (150 ms < time < 250 ms). b) Maximum and averaged values of the τ_n calculated for different subdomains of the ICOMS at the same period of the simulation.

To have a clear understanding of the parameters affecting the hemolysis index, 3D streamlines of the velocity are plotted for time=250ms (Figure 86) of the "TD Low Flow" simulations. 200 streamlines are processed from the starting surface of the coupling (interface 1 shown in Figure 64) up to the end of the diffuser (interface 4). Then, they have been colored based on the values of the hemolysis index (H, Figure 86-a), equivalent stress (τ_n, Figure 86-b), and exposure time (t, Figure 86-c). In this case, the exposure time (t) is the time during which each particle experiences the equivalent stress (τ_n) while passing along a streamline. Using these two parameters, it is possible to recalculate the hemolysis index

for each streamline using equation 22 ($H = C\tau^{\alpha}t^{\beta}$), independently from the results obtained for hemolysis simulations based on equation 23.

Based on this visualization, critical regions of the ICOMS in terms of the hemolysis index can be identified (Figure 86-a). The tip clearance of the impeller, the gap clearance between the impeller and the diffuser, the gap located at the hub of the diffuser, and the secondary outlet of the coupling are the most important ones. Focusing on Figure 86-b and Figure 86-c makes it possible to find the sources of the phenomena. For example, inside the impeller, it is clear that the stress is high at the tip of the blades, especially at the entering sections. But, due to the high rotational speed of this part and consequently high velocity of the flow, the exposure time is relatively small. So, for this part, the source of the hemolysis is the stress and not the exposure time.

Inside the coupling, the stress distribution on streamlines is very small. On the other side, the exposure time is high, since the velocity of the secondary outlet is about 0.15 m/s for this operating condition. Therefore, the higher exposure time is the main reason for the hemolysis here. The diffuser seems to be the most critical part; as the flow experiences a combination of a quite high stress and exposure time.

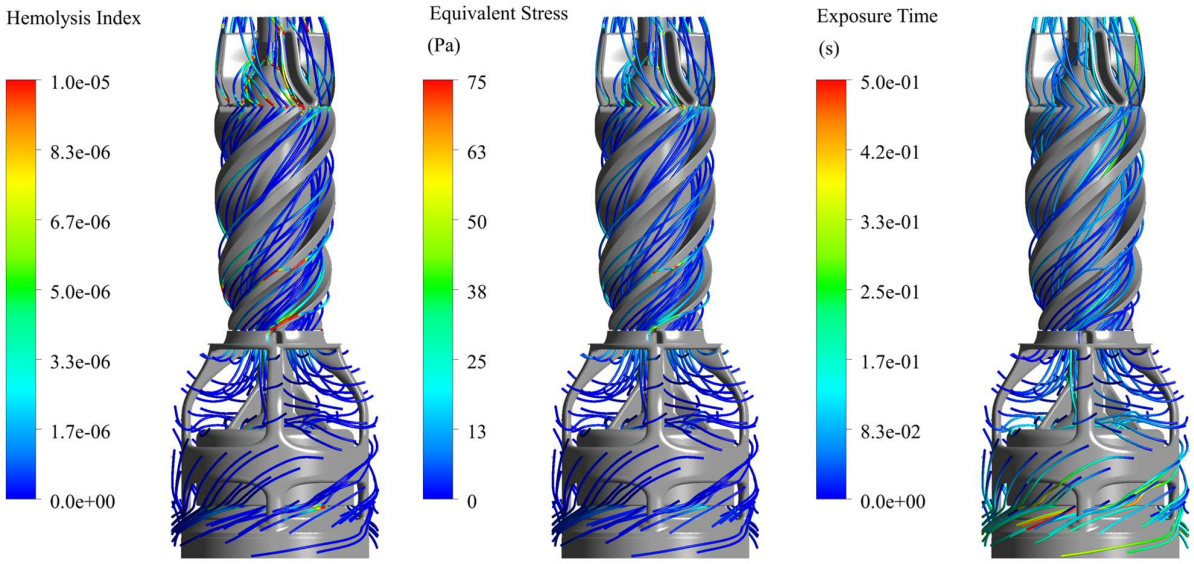

(a) (b) (c)

Figure 86. 3D streamlines are plotted inside the pump for a specific time step of the simulation (time=150 ms) and colored by: a) Hemolysis index. b) Equivalent stress (τ_n). c) Exposure time (t). The starting points of the 200 streamlines are specified in interface 1 shown in Figure 64 and the sampling is defined by the "equally spaced" option (equal distance between all the starting points).

The same post-processing methodology is used to investigate the reason for the slow increase of the hemolysis during the simulation. The objective is to understand why the hemolysis simulations take much more time for this test case compared with the FDA benchmarks. At this point, 3D streamlines were replotted considering two different scenarios:

- Scenario 1: 300 3D streamlines inside the pump with the same options regarding the start surface (Interface 1) and the spacing distance.
- Scenario 2: The same number of streamlines plotted for the whole computing domain (box+pump). The starting surface is applied at the inlet of the box, while the spacing selection for the streamlines is the same as in scenario 1.

For both scenarios, the hemolysis index along the streamlines was calculated using the original format of the Power-law model:

$$HI_{str} = \frac{\int C\tau^{\alpha} t^{\beta} dl}{L} \tag{28}$$

Where, L is the length of each streamline and dl is the spatial derivative on each line. Then, the calculated values are averaged for all the streamlines:

$$HI_{avg} = \frac{\sum_{n=1}^{300} HI_{str}}{N} \tag{29}$$

Figure 87 shows the comparison between the Eulerian-based hemolysis calculations (equation 23), the experimental data, and the streamline-based hemolysis post-processing (equation 22), for the "TD Low Flow" operating condition. In this figure, the streamline-based results for both scenarios are colored in green and red for scenarios 1 and 2, respectively. It is shown that the new method results in relatively high magnitudes of fluctuations in the corresponding curves. This is a consequence of considering a limited amount of streamline, instead of averaging the hemolysis evolution within the entire pump.

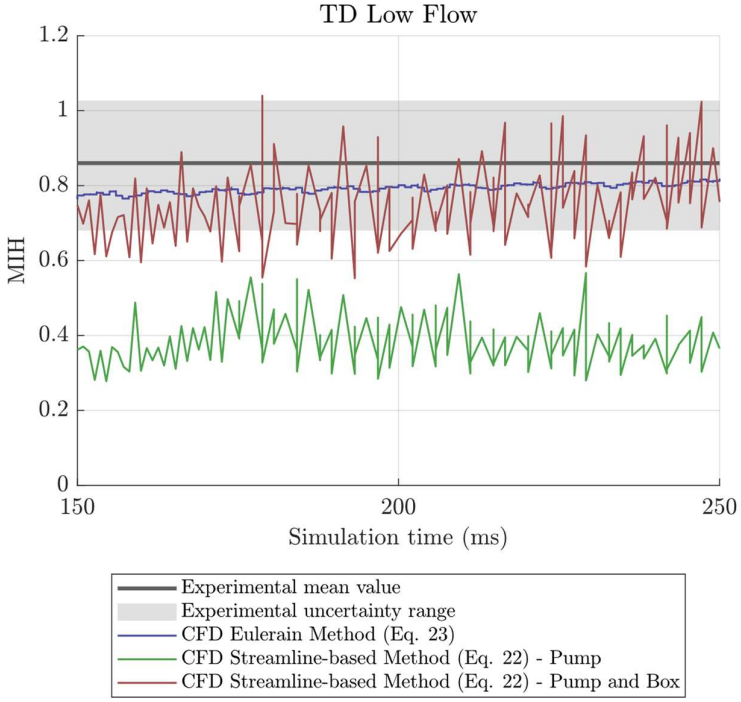

Figure 87. Comparison between the eulerian-based hemolysis calculations (equation 23), the experimental data, and the streamline-based hemolysis post-processing (equation 32), for the "TD Low Flow" operating condition.

Despite this shortcoming, these two curves provide us with some very useful information. The curve related to the hemolysis index inside the pump (green line), oscillates around a constant mean value. It means that the hemolysis production inside the pump is constant in the period of time considered here. Conversely, the red line (hemolysis inside the whole system: box and pump) is increasing with time. It means that a percentage of the flow exiting the pump does not exit the box: it recirculates inside the box. Therefore, compared with the FDA pump benchmark where the outlet of the pump was directly connected to the outlet pipe, here some hemolysis is constantly generated inside the box and is responsible for the slow increase of hemolysis obtained in the CFD simulation. In addition, some flow is passing several times into the ICOMS, thus experiencing a higher increase of hemolysis, even if the in all cases, the difference between inlet and outlet of the pump is constant. Therefore, it takes a significant time for the hemolysis to eventually stabilize within the box as well. In addition, due to the higher rotational speed and flow velocity for the "TD High Flow", the recirculation process for this configuration is faster. Consequently, the hemolysis level stabilizes earlier, compared with the "TD Low Flow".

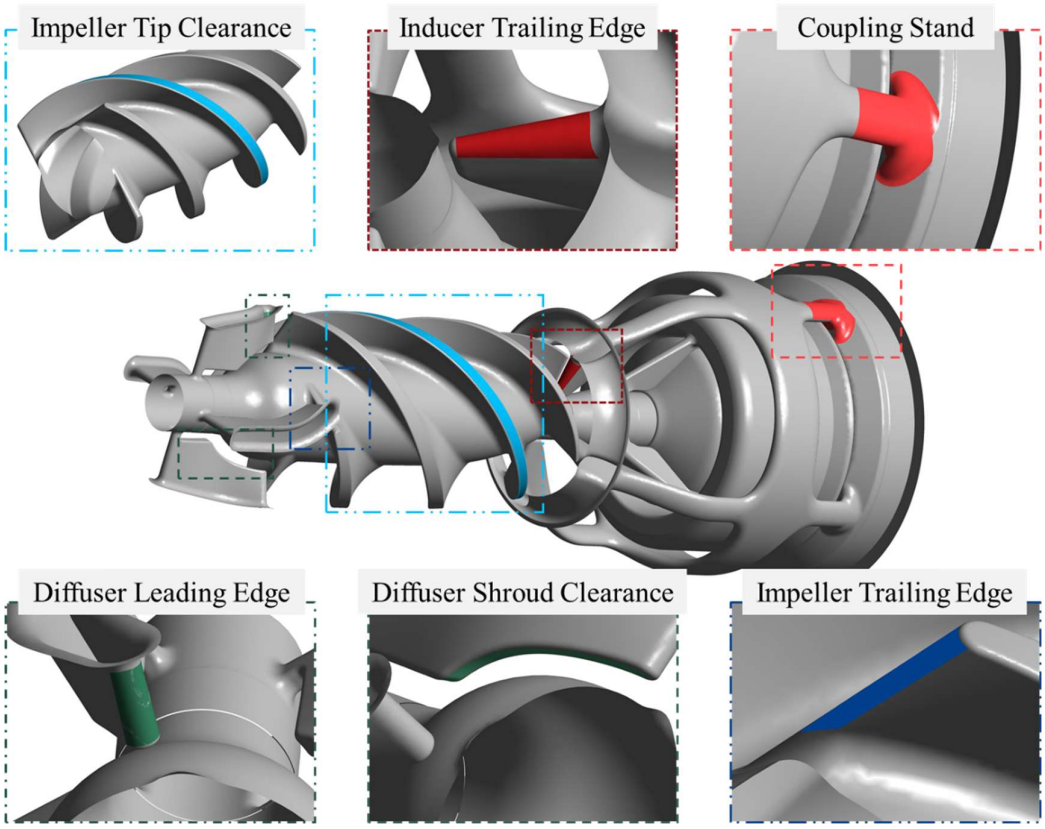

Figure 88. Six critical regions were monitored during one cycle of the simulation to evaluate the sources of hemolysis at each of them: 1. Coupling stand 2. Inducer trailing edge 3. Impeller tip clearance 4. Impeller trailing edge 5. Diffuser shroud clearance 6. Diffuser leading edge.

In this step of the study, the values of the equivalent stress and the hemolysis index in specific areas are monitored through a cycle of rotation for "TD High Flow", which is the main operating configuration

of the pump in a real situation. Here the objective is to evaluate the sources of the hemolysis for each of these regions. The selected ones are coupling stand, inducer trailing edge, impeller tip clearance, impeller trailing edge, diffuser shroud clearance, diffuser leading edge (Figure 88). Figure 89-a displays area-averaged values of the equivalent stress τ_n for the selected regions of the ICOMS during one complete impeller rotation (130 ms < time < 140 ms). As shown by this graph, the values of τ_n for all curves are fluctuating in time, except for the curve of the "Coupling stand". As expected, the highest values of the stress are observed in the impeller ("Impeller trailing edge" then "Impeller tip clearance"), where the velocity of the flow is highest ($V \cong 3m/s$). On the other side, the lowest values are found in the coupling stand, due to the much lower values of the velocity ($V < 0.5\ m/s$). And the diffuser is in between, with values of τ_n that oscillate between 100 and 200 Pa.

Figure 89-b shows the area-averaged hemolysis index curves at the same locations. By comparing Figure 89-b and Figure 89-a, it is obvious that the order of the curves are changed. For instance, the curve of the "Coupling stand" shows the lowest stress but, at the same time, it provides mid-range values for the hemolysis index. In this case, the impact of the exposure time becomes clear. It shows that it is possible to have very low values of the stress in a specific region, due to the low velocity gradients, but to have a long exposure time and consequently a high hemolysis index, for the very same reason (low velocity). As another example, Figure 89-a shows that the "Impeller tip clearance" is a source of high stress in the field, but the predicted hemolysis is lower than in other regions, because of a very low exposure time of particles at the tip of the blades (due to the very high rotational speed of the impeller's blades).

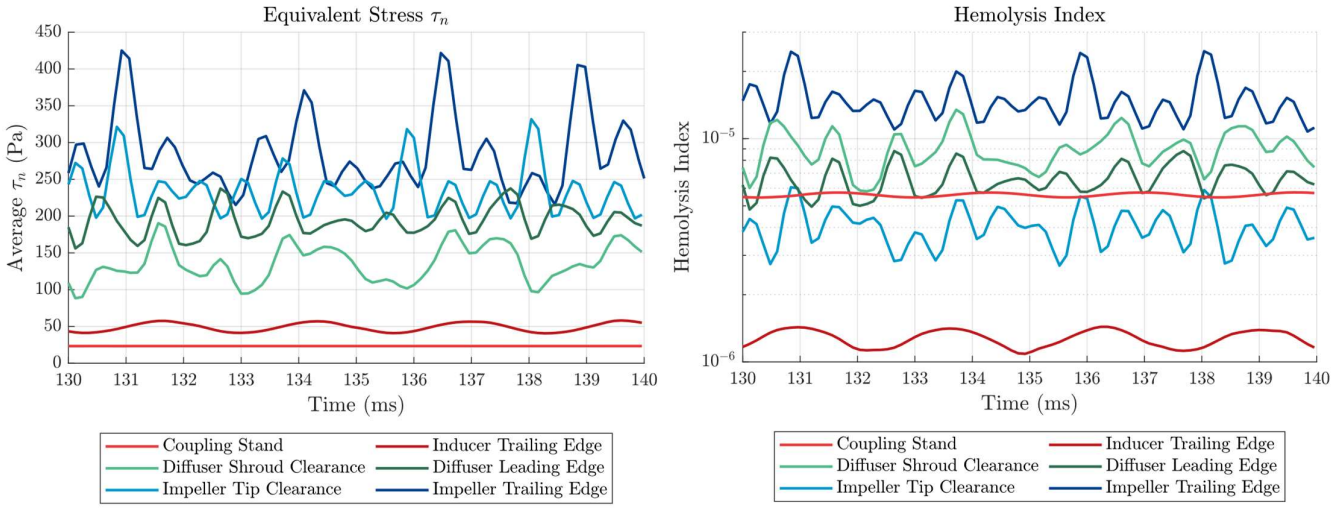

Figure 89. a) Area-averaged values of the equivalent stress τ_n (a) and hemolysis index (b) for selected regions of the ICOMS through one complete rotation of it ("TD High flow").

Anyway, considering Figure 89-b, it is concluded that the most important critical regions of the hemolysis are "Impeller trailing edge", "Diffuser shroud clearance", and "Diffuser leading edge", in that

order. All of the predicted critical regions are located at the outlet regions of the pump, which means that a specific attention needs to be paid to these parts during the pump design.

In addition, five 3D streamlines were plotted for the latest timestep of the simulations of "TD High flow". They were selected to pass through critical regions of the pump (Figure 90). This can help investigating the evolution of the effective parameters on the hemolysis. Each of the streamlines is crossing a specific critical region. For instance, purple (streamline 4) and green (streamline 2) lines pass along the secondary outlet of the pump and the region between the rotating coupling and casing, respectively. Other streamlines go throughout the impeller and diffuser. The orange streamline (streamline 5) faces the tip clearance of the impeller as well as its leading edge. The red one (streamline 1) reaches the diffuser's shroud clearance after facing the inner surfaces of the impeller. Finally, the blue streamline (streamline 3) passes the inner faces of the impeller and the diffuser.

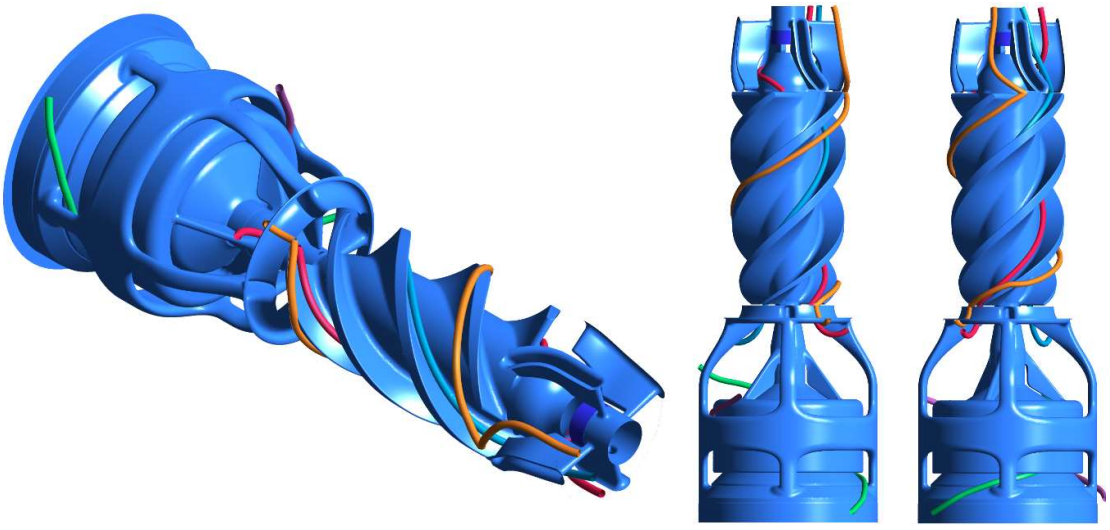

(a) (b) (c)

Figure 90. Selected 3D streamline adjusted close to critical regions to study the equivalent stress, hemolysis index and velocity on them. a) Isovolumetric view b,c) side view from two perpendicular angles.

Figure 91-a shows the evolution of the probed equivalent stress τ_n against time through each of the five 3D streamlines. As expected, the time needed for each of the streamlines to be passed is not equal. The streamlines that pass the impeller and diffuser (Streamlines 1, 3, and 5) finish earlier, compared with the ones passing the coupling. Those lines passing the impeller and diffuser face higher amounts of stress but during short times only. On the other side, streamlines 2 and 4 tolerates lower stress but during larger periods of time.

of the time evolutions of the stress provides some meaningful information. for example, by considering the results of streamline 4, it is evident that relatively high values of stress are passed at the end of the period. Then, looking at the streamline formation (purple curve) in Figure 90, it can be concluded that it is a consequence of the "Coupling stand" geometry.

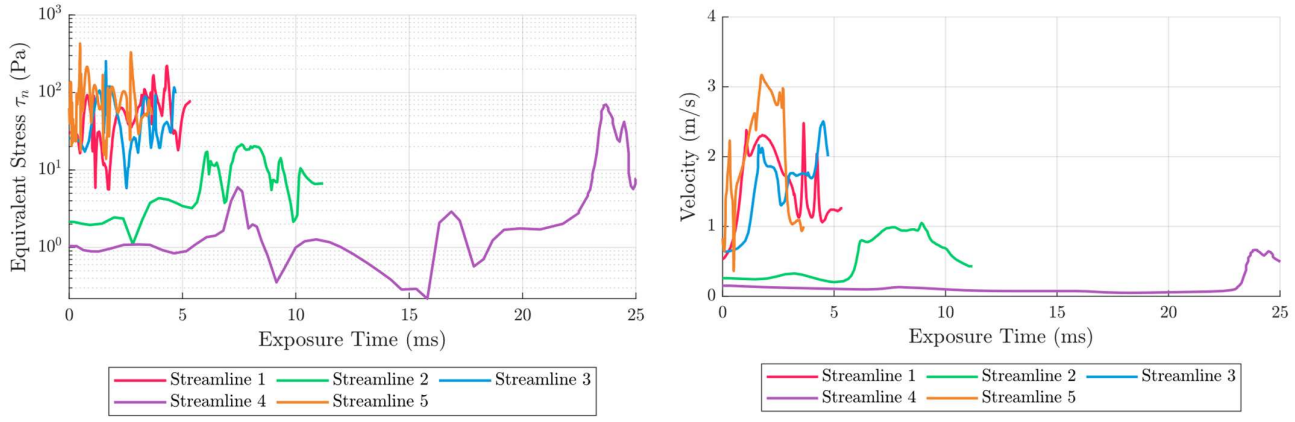

(a) (b)

Figure 91. Evolution of the probed equivalent stress τ_n (a) and velocity (b) through each of the five the 3D streamlines.

Figure 91-b also indicates the evolution of the velocity for the same streamlines. It is clear that the streamlines with the highest velocity finish earlier. As expected, the highest velocity is observed in the streamlines going through the impeller (streamlines 1, 3, and 5). The maximum value of the velocity is reached when the streamline 5 passes the tip clearance of the impeller. On the other hand, the streamline 4 has the lowest velocities but the highest duration.

The evolution is calculated and plotted for the hemolysis index (using equation 22) for the five streamlines (Figure 92-a). As shown by this figure, the streamlines 1, 3, and 5 produce relatively higher amounts of hemolysis index but in smaller time periods. Vice versa, streamlines 2 and 4 generate lower amounts of the hemolysis but in a large period of time.

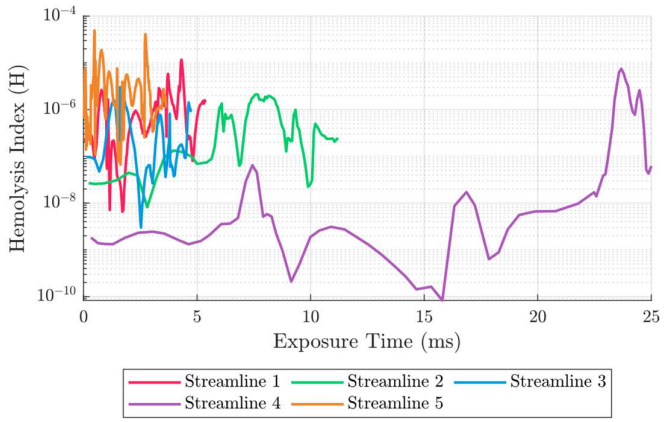

(a)

Location	Hemolysis index (HI_{str})
Streamline 1	1.782×10^{-4}
Streamline 2	4.938×10^{-5}
Streamline 3	6.947×10^{-5}
Streamline 4	8.718×10^{-5}
Streamline 5	1.219×10^{-4}

(b)

Figure 92. a) Evolution of the calculated hemolysis index using equation 22 through each of the five the 3D streamlines. b) Calculated HI_{str} for each of the streamlines based on the equation 32.

In order to provide a quantitative and comparable result for the hemolysis evolution along the five streamlines, the HI_{str} has been calculated for each of them using equation 32 (Figure 92-b). Considering the results, it can be concluded that the streamline 1, which faces the tip of the impeller blades and the leading edge of it, experiences the highest hemolysis. Then, streamline 5 that passes through the diffuser

shroud clearance is the second one. And the streamline 4, which goes through the coupling and faces the “Coupling stand” is the third critical streamline in terms of hemolysis generation.

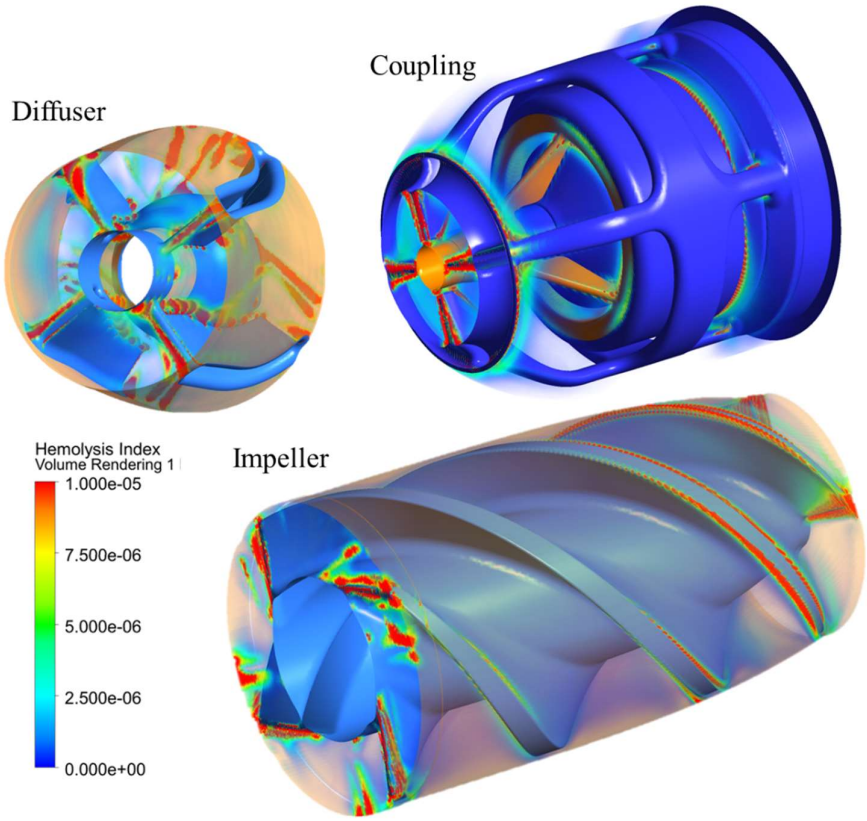

Figure 93. Volume rendering of the hemolysis index inside the hydraulic parts of the ICOMS while operating in "TD High Flow" operating condition.

Figure 93 illustrates the distribution of the hemolysis index inside the hydraulic parts of the ICOMS. It provides a deeper understanding of the most critical regions in terms of hemolysis. Generally, any region that is located between a rotating part and a stationary part or between two rotating parts is a source of hemolysis. For example, inside the diffuser, the critical points include the leading edge and the trailing edge of the blades as well as the gap between the stationary blades and the rotor. Another example, in the impeller, is the leading edge and trailing edge of the blades and the tip clearance.

To the best of our knowledge, there is no clinical equipment to monitor the hemolysis index locally. So, there is no way to validate these qualitative results (Figure 93) directly. However, it is proven that hemolysis is the main source of thrombosis [12–14]. Based on the clinical tests conducted by FineHeart, the same critical regions, indicated by the red color in Figure 93, have been observed to be the sources of thrombosis clots, especially in the coupling and in the diffuser. Unfortunately, due to confidentiality reasons, we are not allowed to report the observations. Meanwhile, it is possible to check the same fact provided by scientific sources for other axial LVADs, as shown hereafter.

Figure 94 indicates the thrombosis formation for different hydraulic parts of the axial pump LVAD HeartMate 2. For example, Figure 94-a shows the thrombosis clots at the leading edge of the impeller blades. This is observed in the FineHeart pump as well. Of course, the size of the blood clots is dependent on the operational condition of the pump (the rotational speed). For instance, the thrombosis clot extends through the impeller blade and fills the flow pathway in Figure 94-c. Figure 94-b and Figure 94-d show the clot formation in the straightener and diffuser of the HeartMate 2, respectively. The location of thrombosis regions in these two figures is consistent with what has been predicted by the numerical framework as well.

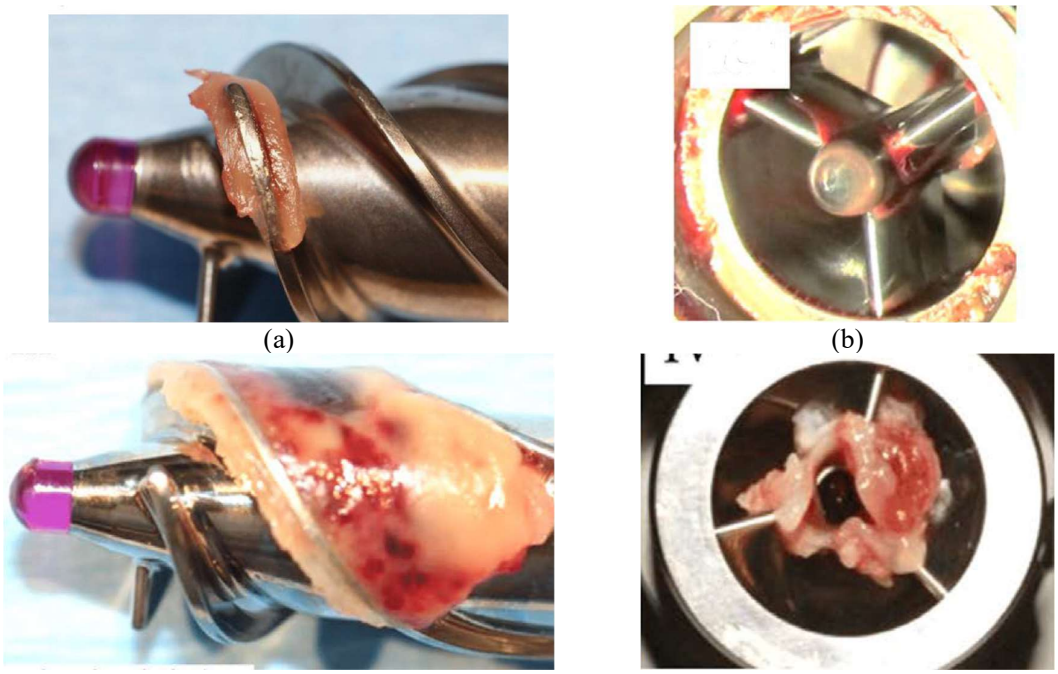

Figure 94. Examples of thrombus clots in the HeartMate 2 LVAD provided by [6,106] for different hydraulic parts of the pump: a) the leading edge of the Impeller blade. b) Leading edge of the Straightener (Inducer). c) Tip clearance of the Impeller blades. d) Diffuser and trailing edge of its blades.

2.4.4. Conclusion

In this section of the thesis, steady and transient simulations were conducted to predict the hemodynamic and hemolysis aspects of the FineHeart blood pump (the ICOMS). This section aimed to use the numerical methodology, which was validated by sections 2.2 and 2.3, to predict the sources of the hemolysis in this innovative device.

Firstly, the flow field inside and outside the pump was validated based on the two sorts of experimental data provided by the company: the correlation loop tests and the PIV measurements. Considering the correlation loop tests, RANS-based steady state simulations were performed for the hydraulic parts of the pump. Characteristic curves of the system, including pressure elevation and torque,

were compared to the experimental measurements. A nice agreement was observed between the two sets of data.

Considering the PIV measurements, transient simulations were carried out while the pump was positioned and operated inside a solid chamber. In this case, RANS equations combined with the K-ω SST model were solved to predict fluid flow behavior inside and outside of the pump. In addition, the Multiple Reference Frames (MRF) methodology was applied to take into account the impeller rotation. To validate the results, five lines have been considered in a mid-plane of the box, and the numerical and experimental velocities were probed and compared. Despite the existence of fluctuations in the numerical data, there is a fair agreement between the experimental data and CFD predictions.

In the next step, the hemolytic parameters were calculated by coupling the RANS equations to the standard transport form of the power-law model using the equivalent stress τ_n ($C_n = 19.45$, the default value). Comparing the predicted hemolysis index with the experimental data at two operating modes of the ICOMS ("TD High Flow" and "TD Low Flow") has shown that the new methodology provides some accurate results. To be more specific, the numerical predictions were inside the range of hemolysis measurements uncertainty. Quantify here the gap between exp and sim: it's much better than just being in the uncertainty range!

The nice correlation between the quantitative numerical and experimental data allows us to visualize the sources of the phenomenon inside the ICOMS. Considering the results, it is evident that the sources of the hemolysis can be classified into two groups: 1. The gaps between two rotating parts or between a rotating part and a stationary part. 2. Leading edge and trailing edge of the blades. By comparing the predicted sources of hemolysis with published images of a commercialized axial blood pump, it is clear that the same critical regions can be found on the HM2 as well. Considering these observations, we can provide some suggestions to FineHeart and any other groups developing axial blood pumps:

- One of the main sources of hemolysis and thrombosis is the gap considered between each set of blades (e.g., between the impeller and the diffuser). In this case, the best strategy is to simplify the design by removing the inducer. Considering the length of the inducer and the velocity of the flow inside it, the inducer cannot help the inlet flow to be uniform. So, it would be useful to have just the impeller and the diffuser as hydraulic parts. This way, it is possible to remove the sources of the hemolysis located on the trailing edge of the inducer (see Figure 93).
- Considering the qualitative result provided by Figure 93, it is expected to have blood clots around the rotating parts of the coupling. It is indeed needed to increase the clearance between the rotating part and the stationary one. So, the flow can pass this space with lower stress resulting in lower impacts of hemolysis.

- Extensive R&D work is needed to see the impact of the leading edge and trailing edge parameters on the hemolysis aspects. From the results, it is evident that these regions as well as the tip clearance are the most critical parameters from the hemolytic point of view. It is also proven that these parameters have also a significant influence on the hydraulic performance of the pump as well. Therefore, an optimization study seems worthy for this part to find the optimum design in terms of both hemodynamics and hemolysis.
- It is important to find the optimum rotational speed of the pump. It is clear that by decreasing the rotational speed the hemolytic effect of the blood pump can decrease meaningfully. So, it would be great to find the optimum rotational speed, which can respond to the heart's flow rate demand with the lowest hemolytic subsequences at the same time; and the best tool to find it is to perform clinical tests.
- Finally, it would be beneficial to conduct such a simulation within the real situation of the blood pump. Knowing that the hemolysis field is a direct consequence of the velocity field and in this case, simulating and testing the pump inside a solid chamber will not take the effects of the wall motions into account.

3. Overall Summary and Conclusion

Despite comprehensive research aimed at developing blood pumps, challenges have arisen due to the occurrence of undesirable natural phenomena such as hemolysis and thrombosis. These phenomena cause blood clots to form inside the pumps, preventing them from functioning properly. From an engineering perspective, one potential solution involves using mathematical models to predict and eliminate the sources of these phenomena. Hemolysis modeling can help developers of left ventricular assist devices (LVADs) reducing the impact of these phenomena to their devices. This requires an accurate and reliable model that bridges the gap between the mechanical and physiological aspects of blood flow. In this thesis, a new methodology has been developed to simulate the hemolysis phenomenon, based on experimental measurements. The primary source of the phenomenon is considered to be extensional stress. One important objective of this work was to evaluate the new model using numerical tools in different geometries. Three test cases are examined: the FDA nozzle benchmark, the FDA pump benchmark, and the FineHeart blood pump (ICOMS). Simulations were performed for these three models in order. For the first two cases, standard models provided by the FDA were used to validate the numerical methodology. For the more realistic FineHeart blood pump, the goal was to provide recommendations for reducing the hemolysis index.

For the FDA nozzle benchmark, numerical simulations were performed to validate the model's predicted hemodynamic field. This was achieved by comparing the model's predictions with experimental measurements for two different operating configurations, one with a sudden expansion upstream from the nozzle and another with a conical diffuser, at a Reynolds number of 6500. Three turbulent models were tested (k-ε, k-ω, and k-ω SST), and the k-ω SST model was found to be reliable for both configurations. Subsequently, the hemolysis index was calculated using two conventional expressions of equivalent shear stress (τ_s and τ_e) and a more recent one (τ_n), and compared with experimental data in three different operating conditions. Despite the large uncertainty of the experimental data, τ_n was found to produce the most reliable results. Additionally, the the effect of the C_n constant in the τ_n expression was investigated for different species, revealing a significant impact on hemolysis, especially for bovine and human blood, where the α coefficient in the model is the largest. A suitable range for the constant was determined to be $18<C_n<30$, by comparing the curve obtained with bovine blood to the experimental range of MIH at three different operating conditions.

Secondly, numerical methods were developed to predict hemodynamic and hemolysis of the blood flow inside the FDA pump benchmark, based on the findings of the nozzle benchmark. The Power-law model with the Eulerian approach was applied, and the same expression of the equivalent shear stress was tested to evaluate the numerical framework in these more realistic operation conditions. Validation of numerical predictions over the flow field was performed by comparing CFD results to the FDA PIV

measurements for three operational conditions, which showed a nice agreement regarding both global aspects and local flow variations. The hemolysis index was calculated by coupling the additional standard transport equation of the power-law model to the RANS equations using the equivalent stress τ_n. Comparisons with experimental data at three operating conditions showed that the new methodology provides accurate results, despite a non-negligible uncertainty on the experimental data. Moreover, the impact of the C_n constant used in the τ_n expression was studied for different species, with a significant effect on hemolysis observed for species where the α coefficient in the model is the largest, such as human blood. By comparing the curve obtained with bovine blood with the experimental range of MIH at three different operating conditions, it was concluded that the appropriate range for the constant is $18<C_n<27$.

For the FineHeart blood pump, steady state and transient simulations were performed to predict the hemodynamic and hemolysis aspects of the ICOMS, with the aim of identifying the sources of hemolysis in the device. The flow field inside and outside the pump was validated based on two types of experimental data: correlation loop tests and PIV measurements. The results showed good agreement between the numerical and experimental data. In the next step, the hemolysis model, which was validated by the FDA benchmarks, was added to the simulations. Hemolytic parameters were then calculated, compared, and validated with the FineHeart data for two operating configurations of the pump. Moreover, the sources of hemolysis were identified as the gaps between rotating and stationary parts, as well as the leading and trailing edges of the blades. Finally, some suggestions for improving the design of axial blood pumps are also provided based on these findings.

The FineHeart blood pump as an innovative left ventricular assist device has had promising results in animal tests to date. This system is waiting for the first human tests in the coming months. We hope that the results presented in this research will lead to the improvement of its performance from the point of view of hemolysis and thrombosis. The method presented in this research can be used from now on as a solution to optimize the design of this pump; A way that can greatly help reduce animal sacrifices and the risk of human use of this LVAD.

.

4. Appendix

4.1. Experimental Equations for the Hemolysis Measurements

As described in section 1.1, Hemolysis is defined as the act of releasing free hemoglobin into the plasma. Earlier in the 1970s and 1980s, reporting and comparing the hemolysis level was difficult owing to the lack of uniformity in the test methods and equations. To respond to the issue, the first standard equation was proposed by Naito et al. (1994) [59]:

$$IH = \Delta fHb \times V \times \frac{100}{Q \times time} \tag{30}$$

Where ΔfHb is the increase of plasma free hemoglobin concentration during the sampling period (g/L), V is the circuit volume (L), Q is the flow rate given as L/min, and time is the sampling interval in (min). The normalized index of hemolysis (NIH) is normalized by hematocrit. The consideration of hematocrit is important for comparison among different values of hematocrit.

$$NIH = \Delta fHb \times V \times \frac{100 - Hct}{100} \frac{100}{Q \times time} \tag{31}$$

Where Hct is the hematocrit in (%). In addition, the modified index of hemolysis (MIH) can be derived from the NIH and accounts for the total hemoglobin concentration in the blood (tHb, mg/dL).

$$MIH = \Delta fHb \times V \times \frac{100 - Hct}{100} \frac{100}{Q \times time} \tag{32}$$

MIH is reported in dimensional units of milligrams of hemoglobin released into plasma divided by the milligrams of total hemoglobin pumped through the loop. To calculate the uncertainty range for the experimental data of NIH, the natural logarithm operator is applied to both sides of the equation (33:

$$\ln(NIH) = \ln(\Delta fHb) + \ln(V) + \ln(100 - Hct) - \ln(Q) - \ln(time) \tag{33}$$

Using equation (35), it is possible to calculate the derivatives of the equilibrium:

$$\frac{\delta NIH}{NIH} = \frac{\delta \Delta fHb}{\Delta fHb} + \frac{\delta V}{V} + \frac{\delta(100 - Hct)}{(100 - Hct)} - \frac{\delta Q}{Q} - \frac{\delta time}{Qtime} \tag{34}$$

So, the error range of the NIH parameter ($\pm\delta NIH$) is accessible by equation (37):

$$\delta NIH = NIH \times \left(\frac{\delta \Delta fHb}{\Delta fHb} + \frac{\delta V}{V} + \frac{\delta(100 - Hct)}{(100 - Hct)} - \frac{\delta Q}{Q} - \frac{\delta time}{Qtime}\right) \tag{35}$$

With the same procedure, the uncertainty range for the modified index of hemolysis can be calculated by equation (38):

$$\delta MIH = MIH \times \left(\frac{\delta NIH}{\text{NIH}} + \frac{\delta tHb}{tHb}\right) \tag{36}$$

We have used equation (38) to calculate the experimental uncertainties of the hemolysis data provided by FineHeart (see section 2.4.3).

4.2. Hemodynamic verification for the FDA nozzle benchmark

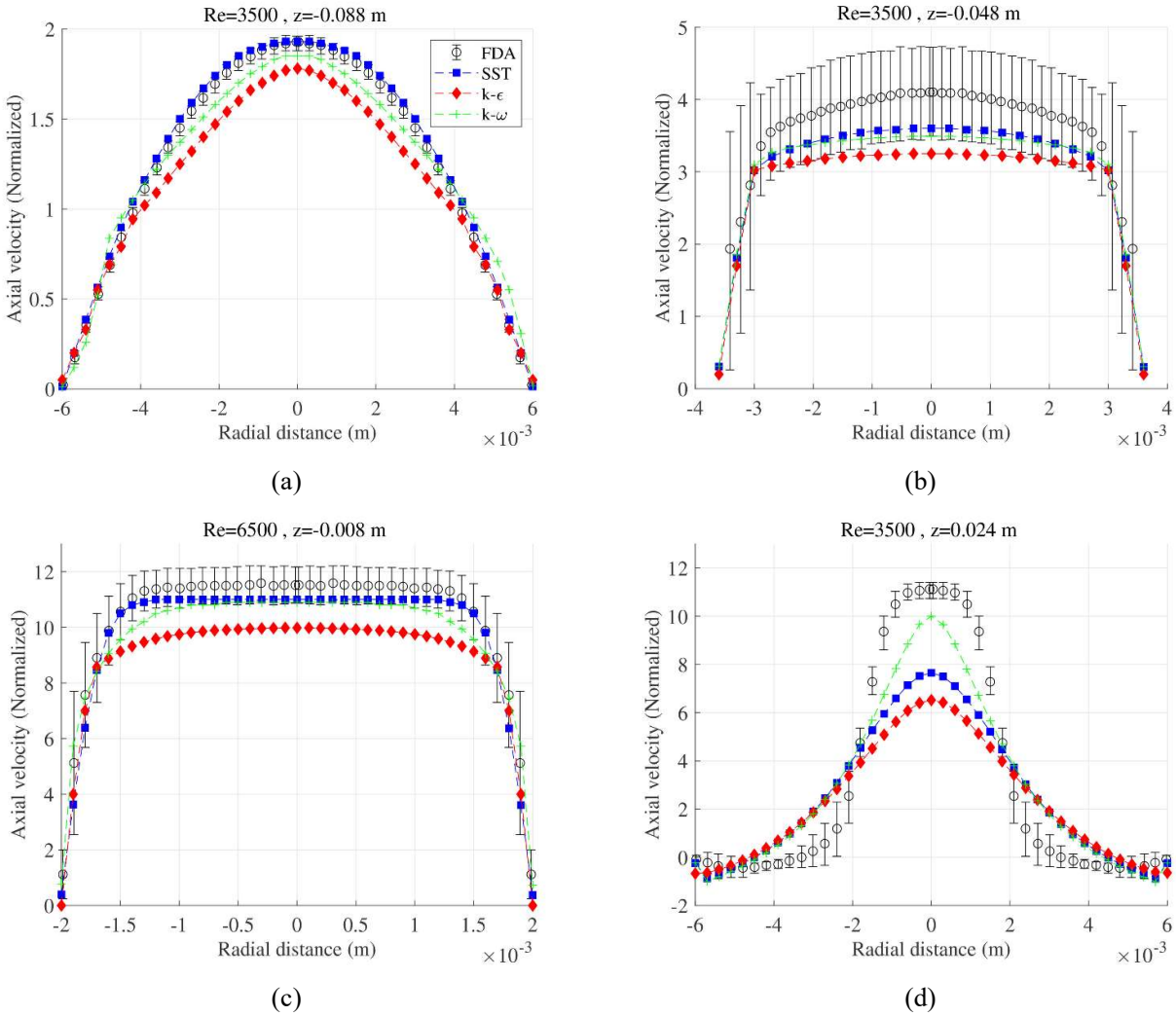

Figure 95. Comparison between experimental and numerical results: axial velocities at Re=3500 for the sudden expansion test case at stations. a) z=-0.088 b) z=-0.048 c) z=-0.008 d) z=0.024.

4.3. Grid Generation for the FineHeart blood pump

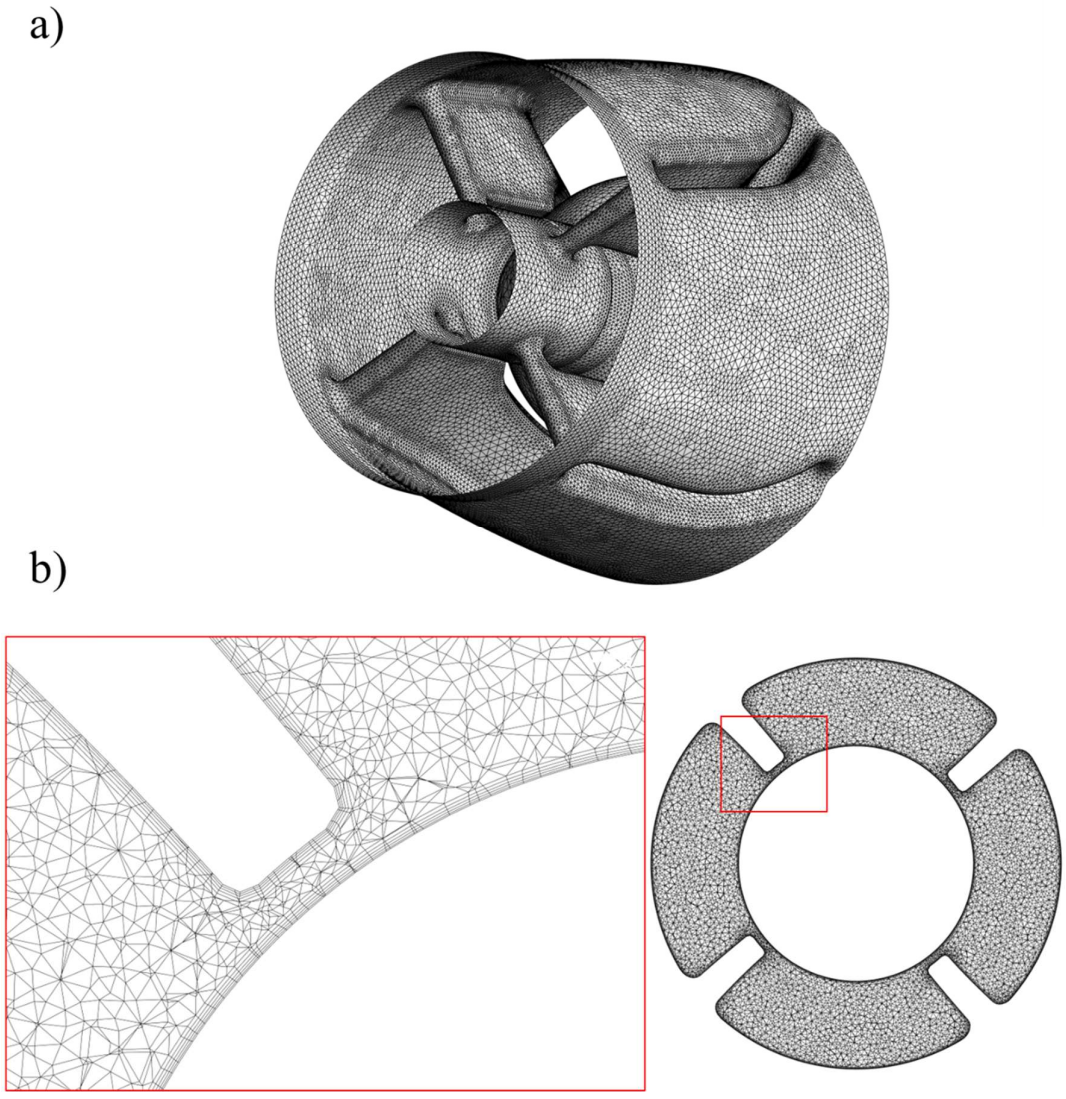

Figure 96. Generated grid of the Diffuser part of the ICOMS for the PIV and hemolysis simulations. a) The Surface imprint mesh. b) The mesh is projected on a plane perpendicular to the axial direction of the pump.

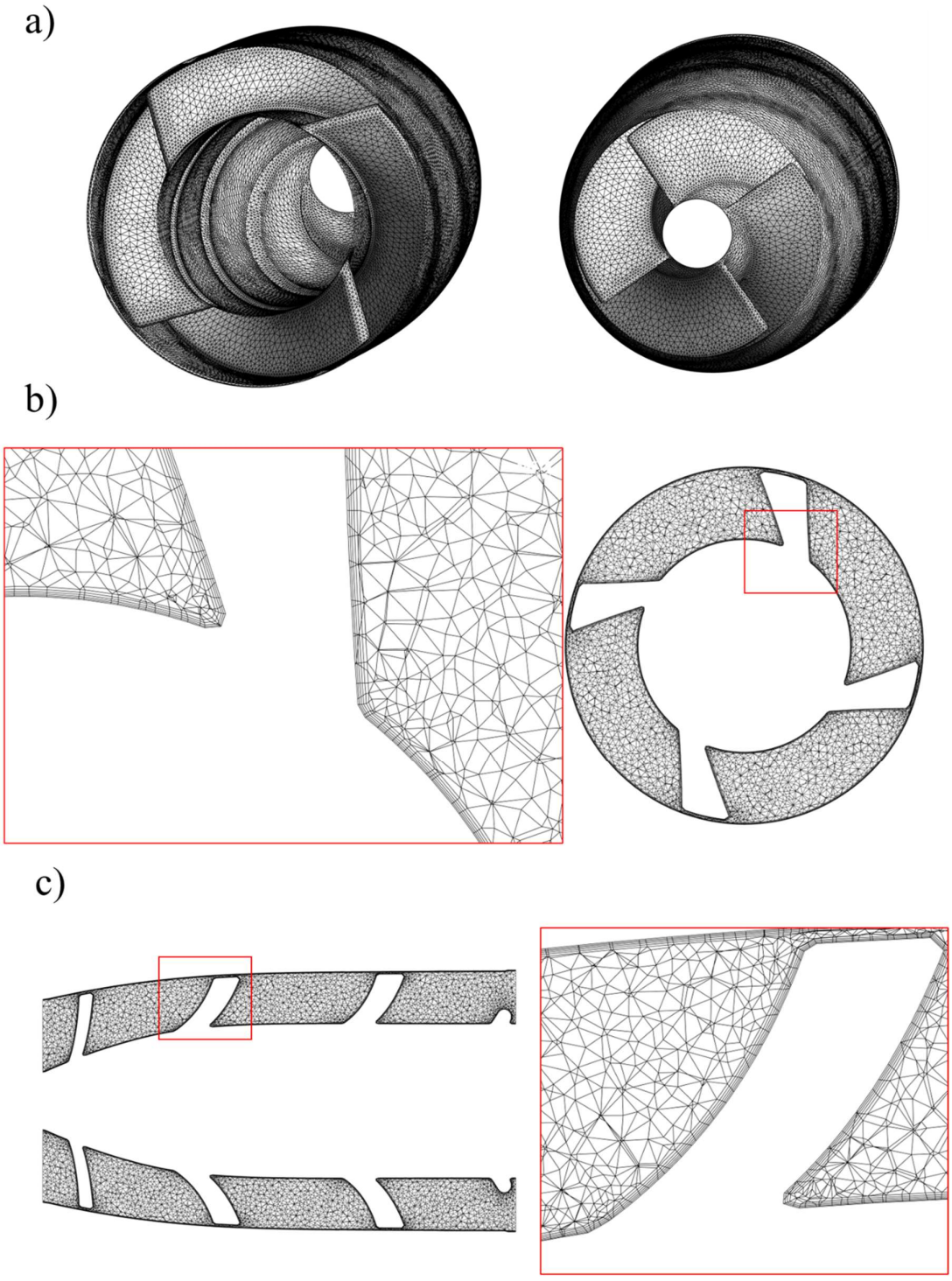

Figure 97. Generated grid of the Impeller part of the ICOMS for the PIV and hemolysis simulations. a) The Surface imprint mesh (right: view from the leading edge. Left: view from the trailing edge). b) The mesh is projected on a plane perpendicular to the axial direction of the pump. c) The mesh is projected to a plane across the axis of the pump.

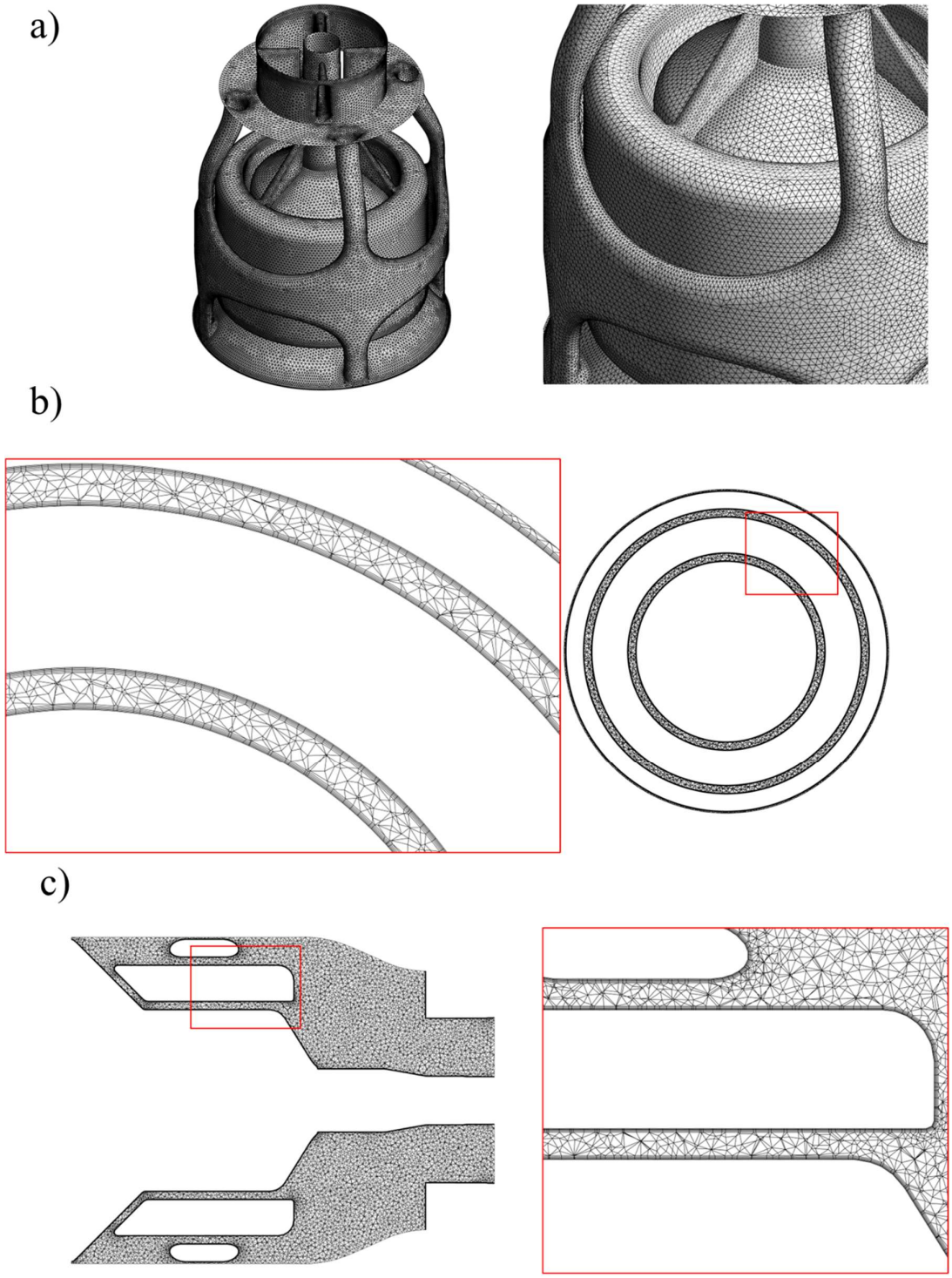

Figure 98. Generated grid of the Coupling part of the ICOMS for the PIV and hemolysis simulations. a) The Surface imprint mesh (right: view from the leading edge. Left: view from the trailing edge). b) The mesh is projected on a plane perpendicular to the axial direction of the pump. c) The mesh is projected to a plane across the axis of the pump.

4.4. Hemodynamic verification for the FineHeart Blood Pump

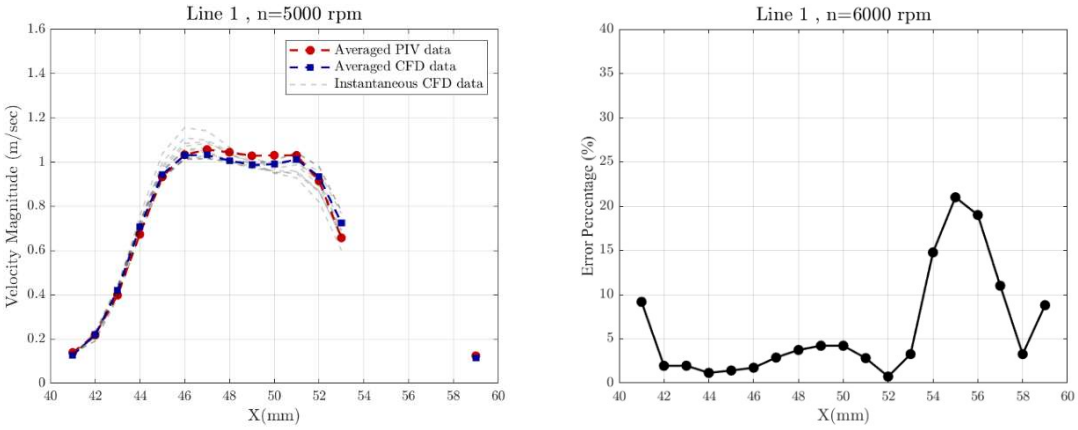

(a) (b)

Figure 99. Comparison between PIV measurements and CFD results for Line 1 (n=5000 rpm). a) Averaged profiles of the velocity magnitudes. b) Error percentage of the CFD calculations for the same profiles.

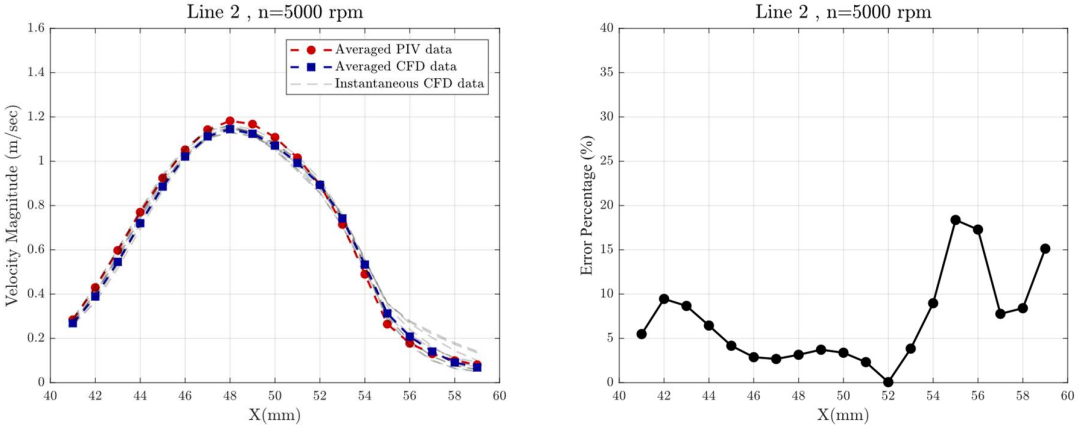

(a) (b)

Figure 100. Comparison between PIV measurements and CFD results for Line 2 (n=5000 rpm). a) Averaged profiles of the velocity magnitudes. b) Error percentage of the CFD calculations for the same profiles.

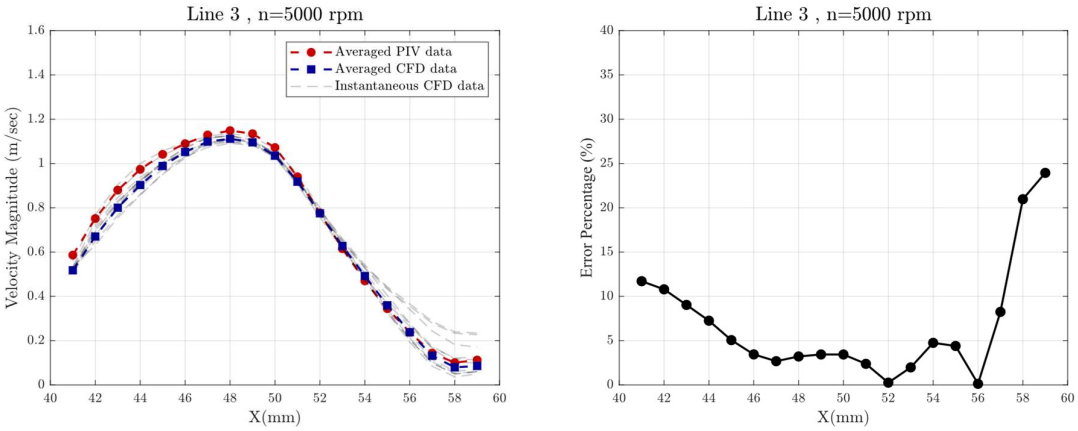

(a) (b)

Figure 101. Comparison between PIV measurements and CFD results for Line 3 (n=5000 rpm). a) Averaged profiles of the velocity magnitudes. b) Error percentage of the CFD calculations for the same profiles.

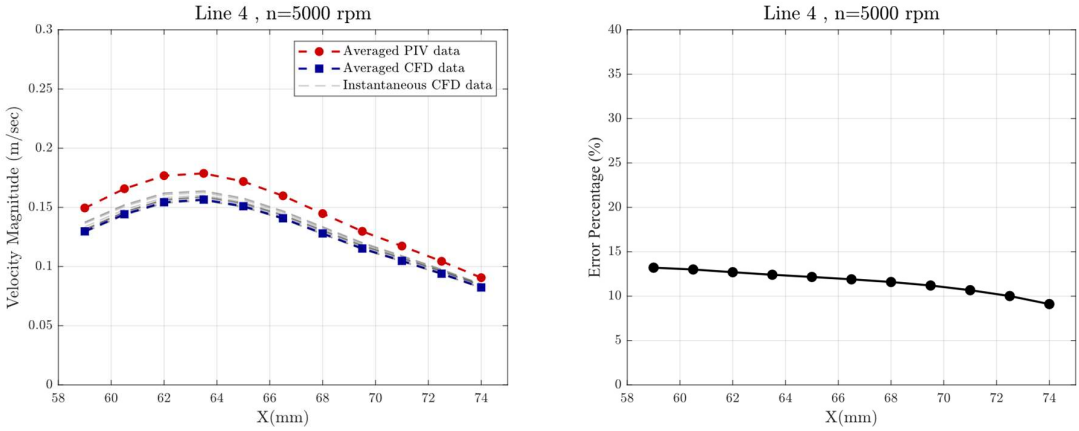

(a) (b)

Figure 102. Comparison between PIV measurements and CFD results for Line 4 (n=5000 rpm). a) Averaged profiles of the velocity magnitudes. b) Error percentage of the CFD calculations for the same profiles.

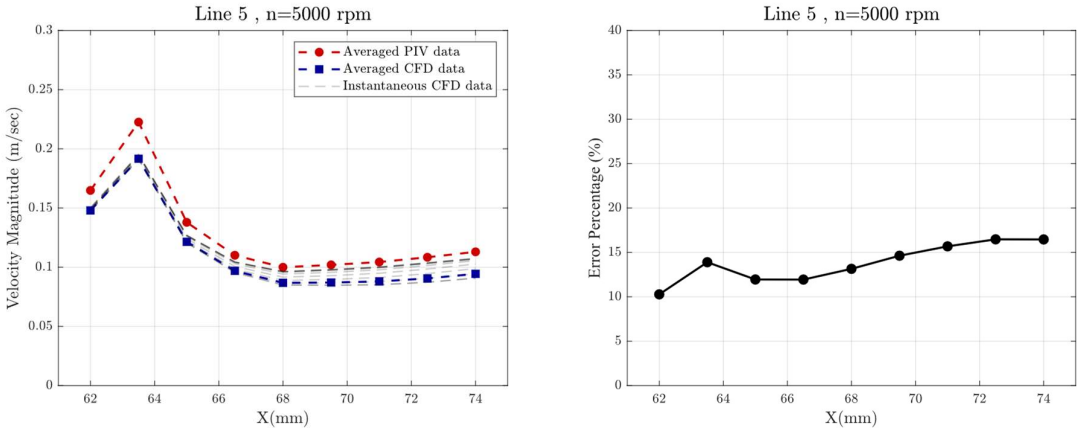

(a) (b)

Figure 103. Comparison between PIV measurements and CFD results for Line 5 (n=5000 rpm). a) Averaged profiles of the velocity magnitudes. b) Error percentage of the CFD calculations for the same profile.

5. References

[1] Gąsiorowski A, Dutkiewicz J. Comprehensive rehabilitation in chronic heart failure. Ann Agric Environ Med 2013;20:606–12.

[2] Heart Failure n.d. https://www.cardiolrx.com/our-focus/heart-failure/.

[3] Torregrossa G, Anyanwu A, Zucchetta F, Gerosa G. SynCardia: the total artificial heart. Ann Cardiothorac Surg 2014;3:612.

[4] Kirklin JK, Naftel DC, Pagani FD, Kormos RL, Stevenson LW, Blume ED, et al. Seventh INTERMACS annual report: 15,000 patients and counting. J Hear Lung Transplant 2015;34:1495–504.

[5] Scandroglio AM, Kaufmann F, Pieri M, Kretzschmar A, Müller M, Pergantis P, et al. Diagnosis and treatment algorithm for blood flow obstructions in patients with left ventricular assist device. J Am Coll Cardiol 2016;67:2758–68.

[6] Uriel N, Han J, Morrison KA, Nahumi N, Yuzefpolskaya M, Garan AR, et al. Device thrombosis in HeartMate II continuous-flow left ventricular assist devices: a multifactorial phenomenon. J Hear Lung Transplant 2014;33:51–9.

[7] Chen Y. Analysis and experiments on flow-induced hemolysis. University of Louisville; 2006.

[8] R. O. Thrombosis and antithrombotic therapy. Cardiovasc Diagn Ther 2017;7:1218–57. https://doi.org/10.21037/cdt.2017.11.08.

[9] Akhtar S, McCash LB, Nadeem S, Saleem A. Scientific breakdown for physiological blood flow inside a tube with multi-thrombosis. Sci Rep 2021;11:1–14.

[10] Lazzari MA, Sanchez-Luceros A, Woods AI, Alberto MF, Meschengieser SS. Von Willebrand factor (VWF) as a risk factor for bleeding and thrombosis. Hematology 2012;17:s150–2.

[11] Tschopp TB, Baumgartner HR. Physiological experiments in haemostasis and thrombosis. Br J Haematol 1975;31:221–9.

[12] Bartoli CR, Zhang D, Kang J, Hennessy-Strahs S, Restle D, Howard J, et al. Clinical and in vitro evidence that subclinical hemolysis contributes to LVAD thrombosis. Ann Thorac Surg 2018;105:807–14.

[13] Da Q, Teruya M, Guchhait P, Teruya J, Olson JS, Cruz MA. Free hemoglobin increases von Willebrand factor–mediated platelet adhesion in vitro: implications for circulatory devices.

Blood, J Am Soc Hematol 2015;126:2338–41.

[14] Tsai H-M, Lian EC-Y. Antibodies to von Willebrand factor–cleaving protease in acute thrombotic thrombocytopenic purpura. N Engl J Med 1998;339:1585–94.

[15] Giersiepen M, Wurzinger LJ, Opitz R, Reul H. Estimation of shear stress-related blood damage in heart valve prostheses-in vitro comparison of 25 aortic valves. Int J Artif Organs 1990;13:300–6.

[16] Heuser G, Opitz R. A Couette viscometer for short time shearing of blood. Biorheology 1980;17:17–24.

[17] Zhang T, Taskin ME, Fang H, Pampori A, Jarvik R, Griffith BP, et al. Study of flow-induced hemolysis using novel couette-type blood-shearing devices. Artif Organs 2011;35:1180–6.

[18] Ding J, Niu S, Chen Z, Zhang T, Griffith BP, Wu ZJ. Shear-induced hemolysis: species differences. Artif Organs 2015;39:795–802.

[19] Yu H, Engel S, Janiga G, Thévenin D. A review of hemolysis prediction models for computational fluid dynamics. Artif Organs 2017;41:603–21.

[20] Faghih MM, Sharp MK. Modeling and prediction of flow-induced hemolysis: a review. Biomech Model Mechanobiol 2019;18:845–81.

[21] Ngoepe MN, Frangi AF, Byrne J V, Ventikos Y. Thrombosis in cerebral aneurysms and the computational modeling thereof: a review. Front Physiol 2018;9:306.

[22] Delvasto-Nuñez L, Jongerius I, Zeerleder S. It takes two to thrombosis: Hemolysis and complement. Blood Rev 2021;50:100834.

[23] Su B, Chua LP, Wang X. Validation of an axial flow blood pump: Computational fluid dynamics results using particle image velocimetry. Artif Organs 2012;36:359–67.

[24] Schüle CY, Thamsen B, Blümel B, Lommel M, Karakaya T, Paschereit CO, et al. Experimental and numerical investigation of an axial rotary blood pump. Artif Organs 2016;40:E192--E202.

[25] Fan H, Hong F, Zhang G, Ye L, Liu Z-M. Applications of CFD technique in the design and flow analysis of implantable axial flow blood pump. J Hydrodyn 2010;22:518–25.

[26] Chassagne F, Beckman J, Mahr C, Aliseda A. The effect of timing of the LVAD speed modulation on intraventricular flow patterns. An in-vitro PIV study. APS Div. Fluid Dyn. Meet. Abstr., 2021, p. E28-006.

[27] Steiner JM, Gomez R, Suchodolski JS, Lidbury JA. Specificity of, and influence of hemolysis, lipemia, and icterus on serum lipase activity as measured by the v-LIP-P slide. Vet Clin Pathol

2017;46:508–15.

[28] Skalak R, Ozkaya N, Skalak TC. Biofluid mechanics. Annu Rev Fluid Mech 1989;21:167–200.

[29] Robert S. Schwartz. blood biochemistry. Encycl Br 2022. https://www.britannica.com/science/blood-biochemistry.

[30] Klinken SP. Red blood cells. Int J Biochem Cell Biol 2002;34:1513–8.

[31] Fung YCB, Tong P. Theory of the sphering of red blood cells. Biophys J 1968;8:175–98.

[32] Andrews DA, Low PS. Role of red blood cells in thrombosis. Curr Opin Hematol 1999;6:76.

[33] Aycock KI, Campbell RL, Lynch FC, Manning KB, Craven BA. The importance of hemorheology and patient anatomy on the hemodynamics in the inferior vena cava. Ann Biomed Eng 2016;44:3568–82.

[34] Fraser KH, Zhang T, Taskin ME, Griffith BP, Wu ZJ. A quantitative comparison of mechanical blood damage parameters in rotary ventricular assist devices: shear stress, exposure time and hemolysis index 2012.

[35] Mohammadi R, Karimi MS, Raisee M, Sharbatdar M. Probabilistic CFD analysis on the flow field and performance of the FDA centrifugal blood pump. Appl Math Model 2022.

[36] Pinotti M, Rosa ES. Computational prediction of hemolysis in a centrifugal ventricular assist device. Artif Organs 1995;19:267–73.

[37] Song X, Throckmorton AL, Wood HG, Allaire PE, Olsen DB. Transient and quasi-steady computational fluid dynamics study of a left ventricular assist device. ASAIO J 2004;50:410–7.

[38] Untaroiu A, Throckmorton AL, Patel SM, Wood HG, Allaire PE, Olsen DB. Numerical and experimental analysis of an axial flow left ventricular assist device: the influence of the diffuser on overall pump performance. Artif Organs 2005;29:581–91.

[39] Li H, Chan WK. Inverse design and CFD investigation of blood pump impeller. Crit Rev Biomed Eng 2000;28.

[40] Burgreen GW, Antaki JF, Wu ZJ, Holmes AJ. Computational fluid dynamics as a development tool for rotary blood pumps. Artif Organs 2001;25:336–40.

[41] Zhang Y, Zhan Z, Gui X-M, Sun H-S, Zhang H, Zheng Z, et al. Design optimization of an axial blood pump with computational fluid dynamics. ASAIO J 2008;54:150–5.

[42] Legendre D, Antunes P, Bock E, Andrade A, Biscegli JF, Ortiz JP. Computational fluid dynamics investigation of a centrifugal blood pump. Artif Organs 2008;32:342–8.

[43] Al-Azawy MG, Turan A, Revell A. Assessment of turbulence models for pulsatile flow inside a heart pump. Comput Methods Biomech Biomed Engin 2016;19:271–85.

[44] Medvitz RB. Development and validation of a computational fluid dynamic methodology for pulsatile blood pump design and prediction of thrombus potential. The Pennsylvania State University; 2008.

[45] Al-Azawy MG, Turan A, Revell A. Investigating the impact of non-Newtonian blood models within a heart pump. Int j Numer Method Biomed Eng 2017;33:e02780.

[46] Griffith BP, Kormos RL, Borovetz HS, Litwak K, Antaki JF, Poirier VL, et al. HeartMate II left ventricular assist system: from concept to first clinical use. Ann Thorac Surg 2001;71:S116–20.

[47] Miyazoe Y, Sawairi T, Ito K, Konishi Y, Yamane T, Nishida M, et al. Computational fluid dynamics analysis to establish the design process of a centrifugal blood pump: second report. Artif Organs 1999;23:762–8.

[48] Anderson JB, Wood HG, Allaire PE, Bearnson G, Khanwilkar P. Computational flow study of the continuous flow ventricular assist device, prototype number 3 blood pump. Artif Organs 2000;24:377–85.

[49] Curtas AR, Wood HG, Allaire PE, McDaniel JC, Day SW, Olsen DB. Computational fluid dynamics modeling of impeller designs for the HeartQuest left ventricular assist device. ASAIO J 2002;48:552–61.

[50] Arvand A, Hahn N, Hormes M, Akdis M, Martin M, Reul H. Comparison of hydraulic and hemolytic properties of different impeller designs of an implantable rotary blood pump by computational fluid dynamics. Artif Organs 2004;28:892–8.

[51] Zhang Y, Xue S, Gui X, Sun H, Zhang H, Zhu X, et al. A novel integrated rotor of axial blood flow pump designed with computational fluid dynamics. Artif Organs 2007;31:580–5.

[52] Zhu L, Zhang X, Yao Z. Shape optimization of the diffuser blade of an axial blood pump by computational fluid dynamics. Artif Organs 2010;34:185–92.

[53] Mozafari S, Rezaienia MA, Paul GM, Rothman MT, Wen P, Korakianitis T. The effect of geometry on the efficiency and hemolysis of centrifugal implantable blood pumps. Asaio J 2017;63:53–9.

[54] Ghadimi B, Nejat A, Nourbakhsh SA, Naderi N. Shape optimization of a centrifugal blood pump by coupling CFD with metamodel-assisted genetic algorithm. J Artif Organs 2019;22:29–36.

[55] Schmitto JD, Hanke JS, Rojas S V, Avsar M, Haverich A. First implantation in man of a new magnetically levitated left ventricular assist device (HeartMate III). J Hear Lung Transplant

2015;34:858–60.

[56] Blackshear Jr PL, Dorman FD, Steinbach JH. Some mechanical effects that influence hemolysis. ASAIO J 1965;11:112–7.

[57] Frank JJ, Bermes EW, Bickel MJ, Watkins BF. Effect of in vitro hemolysis on chemical values for serum. Clin Chem 1978;24:1966–70.

[58] Yücel D, Dalva K. Effect of in vitro hemolysis on 25 common biochemical tests. Clin Chem 1992;38:575–7.

[59] Naito K, Mizuguchi K, Nosé Y. The need for standardizing the index of hemolysis. Artif Organs 1994;18:7–10.

[60] Blackshear Jr PL, Dorman FD, Steinbach JH, Maybach EJ, Singh A, Collingham RE. Shear, wall interaction and hemolysis. Asaio J 1966;12:113–20.

[61] Nevaril CG, Lynch EG, Alfrey CP, Hellums JD. Erythrocyte damage and destruction induced by shearing stress. J Lab Clin Med 1968;71:784–90.

[62] Forstrom RJ. A new measure of erythrocyte membrane strength-the jet fragility test. University of Minnesota; 1969.

[63] Leverett LB, Hellums JD, Alfrey CP, Lynch EC. Red blood cell damage by shear stress. Biophys J 1972;12:257–73.

[64] Paul R, Apel J, Klaus S, Schügner F, Schwindke P, Reul H. Shear stress related blood damage in laminar couette flow. Artif Organs 2003;27:517–29.

[65] Lee SS, Ahn KH, Lee SJ, Sun K, Goedhart PT, Hardeman MR. Shear induced damage of red blood cells monitored by the decrease of their deformability. Korea-Australia Rheol J 2004;16:141–6.

[66] Kameneva M V, Burgreen GW, Kono K, Repko B, Antaki JF, Umezu M. EFFECTS OF TURBULENT STRESSES ON MECHANICAL HEMOLYSIS: EXPERIMENTAL AND COMPUTATIONAL ANALYSIS. ASAIO J (American Soc Artif Intern Organs 1992) 2004;50:418.

[67] Zhao R, Antaki JF, Naik T, Bachman TN, Kameneva M V, Wu ZJ. Microscopic investigation of erythrocyte deformation dynamics. Biorheology 2006;43:747–65.

[68] Boehning F, Mejia T, Schmitz-Rode T, Steinseifer U. Hemolysis in a laminar flow-through couette shearing device: an experimental study. Artif Organs 2014;38:761–5.

[69] Laugel J-F, Beissinger RL. Low stress shear-induced hemolysis in capillary flow. Trans Soc

Artif Intern Organs 1983;29:158–62.

[70] Arvand A, Hormes M, Reul H. A validated computational fluid dynamics model to estimate hemolysis in a rotary blood pump. Artif Organs 2005;29:531–40.

[71] Wurzinger LJ, Opitz R, Eckstein H. Mechanical bloodtrauma. An overview. Angéiologie (Paris) 1986;38:81–97.

[72] Wurzinger LJ, Opitz R, Blasberg P, Schmid-Schönbein H. Platelet and coagulation parameters following millisecond exposure to laminar shear stress. Thromb Haemost 1985;54:381–6.

[73] Faghih MM, Sharp MK. Extending the Power-Law Hemolysis Model to Complex Flows 2017;138:6–9. https://doi.org/10.1115/1.4034786.

[74] Faghih MM, Sharp MK. On Eulerian versus Lagrangian models of mechanical blood damage and the linearized damage function. Artif Organs 2019;43:681–7.

[75] Good BC, Manning KB. Computational modeling of the Food and Drug Administration's benchmark centrifugal blood pump. Artif Organs 2020;44:E263–76.

[76] Lacasse D, Garon A, Pelletier D. Mechanical hemolysis in blood flow: user-independent predictions with the solution of a partial differential equation. Comput Methods Biomech Biomed Engin 2007;10:1–12.

[77] Salazar FA, Rojas-Solo´ rzano LR, Antaki JF. Numerical study of turbulence models in the computation of blood flow in cannulas. Fluids Eng. Div. Summer Meet., vol. 48401, 2008, p. 999–1005.

[78] Nikfar M, Razizadeh M, Zhang J, Paul R, Wu ZJ, Liu Y. Prediction of mechanical hemolysis in medical devices via a Lagrangian strain-based multiscale model. Artif Organs 2020;44:E348–68.

[79] Heck ML, Yen A, Snyder TA, O'Rear EA, Papavassiliou D V. Flow-field simulations and hemolysis estimates for the food and drug administration critical path initiative centrifugal blood pump. Artif Organs 2017;41:E129–40.

[80] Taskin ME, Fraser KH, Zhang T, Wu C, Griffith BP, Wu ZJ. Evaluation of Eulerian and Lagrangian models for hemolysis estimation. ASAIO J 2012;58:363–72.

[81] Menter FR. Two-equation eddy-viscosity turbulence models for engineering applications. AIAA J 1994;32:1598–605.

[82] Bludszuweit C. Three-Dimensional numerical prediction of stress loading of blood particles in a centrifugal pump. Artif Organs 1995;19:590–6.

[83] Faghih MM, Keith Sharp M. Extending the power-law hemolysis model to complex flows. J Biomech Eng 2016;138.

[84] Faghih MM, Sharp MK. Deformation of human red blood cells in extensional flow through a hyperbolic contraction. Biomech Model Mechanobiol 2020;19:251–61.

[85] Herbertson LH, Olia SE, Daly A, Noatch CP, Smith WA, Kameneva M V, et al. Multilaboratory study of flow-induced hemolysis using the FDA benchmark nozzle model. Artif Organs 2015;39:237–48.

[86] Tobin N, Manning KB. Large-eddy simulations of flow in the FDA benchmark nozzle geometry to predict hemolysis. Cardiovasc Eng Technol 2020;11:254–67.

[87] Hariharan P, Giarra M, Reddy V, Day SW, Manning KB, Deutsch S, et al. Multilaboratory particle image velocimetry analysis of the FDA benchmark nozzle model to support validation of computational fluid dynamics simulations. J Biomech Eng 2011;133.

[88] Malinauskas RA, Hariharan P, Day SW, Herbertson LH, Buesen M, Steinseifer U, et al. FDA benchmark medical device flow models for CFD validation. ASAIO J 2017;63:150–60.

[89] Haddadi M. Conception et développement dune turbine intracardiaque pour suppléer les insuffisances cardiaques. Paris Est, 2015.

[90] Janiga G. Large eddy simulation of the FDA benchmark nozzle for a Reynolds number of 6500. Comput Biol Med 2014;47:113–9.

[91] Stewart SFC, Paterson EG, Burgreen GW, Hariharan P, Giarra M, Reddy V, et al. Assessment of CFD performance in simulations of an idealized medical device: results of FDA's first computational interlaboratory study. Cardiovasc Eng Technol 2012;3:139–60.

[92] Stewart SFC, Hariharan P, Paterson EG, Burgreen GW, Reddy V, Day SW, et al. Results of FDA's first interlaboratory computational study of a nozzle with a sudden contraction and conical diffuser. Cardiovasc Eng Technol 2013;4:374–91.

[93] Trias M, Arbona A, Massó J, Miñano B, Bona C. FDA's nozzle numerical simulation challenge: non-Newtonian fluid effects and blood damage. PLoS One 2014;9:e92638.

[94] Manchester EL, Xu XY. The effect of turbulence on transitional flow in the FDA's benchmark nozzle model using large-eddy simulation. Int j Numer Method Biomed Eng 2020;36:e3389.

[95] Hariharan P, D'Souza GA, Horner M, Morrison TM, Malinauskas RA, Myers MR. Use of the FDA nozzle model to illustrate validation techniques in computational fluid dynamics (CFD) simulations. PLoS One 2017;12:e0178749.

[96] Wu P, Groß-Hardt S, Boehning F, Hsu P-L. An energy-dissipation-based power-law formulation for estimating hemolysis. Biomech Model Mechanobiol 2020;19:591–602.

[97] Cleland JGF, Daubert J-C, Erdmann E, Freemantle N, Gras D, Kappenberger L, et al. The effect of cardiac resynchronization on morbidity and mortality in heart failure. N Engl J Med 2005;352:1539–49.

[98] committee A. Standard practice for assessment of hemolysis in continuous flow blood pumps. vol. 13. 1998.

[99] ANSYS Inc. ANSYS CFX-Solver Theory Guide. vol. 15317. 2009.

[100] Morshed KN, Bark D, Forleo M, Dasi LP. Theory to predict shear stress on cells in turbulent blood flow. PLoS One 2014;9. https://doi.org/10.1371/journal.pone.0105357.

[101] Fehn N, Wall WA, Kronbichler M. Modern discontinuous Galerkin methods for the simulation of transitional and turbulent flows in biomedical engineering: a comprehensive LES study of the FDA benchmark nozzle model. Int j Numer Method Biomed Eng 2019;35:e3228.

[102] Chau KT. Electric vehicle machines and drives: design, analysis and application. John Wiley & Sons; 2015.

[103] Karimi MS, Razzaghi P, Raisee M, Hendrick P, Nourbakhsh A. Stochastic simulation of the FDA centrifugal blood pump benchmark. Biomech Model Mechanobiol 2021;20:1871–87. https://doi.org/10.1007/s10237-021-01482-0.

[104] Avci M, Heck M, O'Rear EA, Papavassiliou D V. Hemolysis estimation in turbulent flow for the FDA critical path initiative centrifugal blood pump. Biomech Model Mechanobiol 2021;20:1709–22. https://doi.org/10.1007/s10237-021-01471-3.

[105] Wu P, Zhang L, Gao Q, Dai W. Effect of turbulent inlet conditions on the prediction of flow field and hemolysis in the FDA ideal medical device. Proc Inst Mech Eng Part C J Mech Eng Sci 2021;235:391–401.

[106] Rowlands GW, Pagani FD, Antaki JF. Classification of the frequency, severity, and propagation of thrombi in the HeartMate II left ventricular assist device. ASAIO J 2020:992–9. https://doi.org/10.1097/MAT.0000000000001151.

6. Résumé Étendu en Français

6.1. Introduction

Dans les directives de l'American Heart Association (AHA), l'insuffisance cardiaque (IC) est définie comme "un syndrome clinique complexe qui peut résulter de tout trouble cardiaque structurel ou fonctionnel qui altère la capacité du ventricule à remplir ou à éjecter le sang" [2,3]. D'un point de vue physiologique, l'insuffisance cardiaque signifie réduire l'efficacité du cœur à envoyer ou à recevoir le flux sanguin en fonction des besoins des organes naturels. Selon les dernières statistiques de l'Organisation mondiale de la santé, les maladies cardiovasculaires sont la principale cause de décès dans le monde, emportant environ 17,9 millions de vies chaque année [1]. Dans les sociétés développées, la prévalence des maladies cardiaques reconnues est estimée à 1 % à 2 % de la population âgée, les coûts de santé associés aux États-Unis dépassant 30 milliards de dollars par an.

Pendant ce temps, la propagation des maladies cardiovasculaires a motivé les scientifiques et les innovateurs à fournir un dispositif d'assistance approprié pour le cœur. Comme mentionné, l'objectif de tous ces systèmes est de faire le pont entre l'insuffisance cardiaque et la transplantation cardiaque. Le cœur artificiel total, la pompe à ballon intra-aortique et le dispositif d'assistance ventriculaire (VAD) sont différents types de dispositifs d'assistance. Un dispositif d'assistance ventriculaire, communément appelé pompe à sang, est une pompe mécanique reliée aux muscles ventriculaires et aux artères associées pour assister le ventricule et augmenter le débit cardiaque. Cet équipement est utilisé pour les patients transplantés cardiaques et les patients sans conditions de transplantation. En raison des limites des transplantations cardiaques, l'utilisation de la VAD en tant que thérapie ciblée a augmenté ces dernières années. Près d'un patient sur deux souffrant d'affections aiguës a été traité avec cet équipement [4].

Malgré des recherches approfondies pour développer ces dispositifs, des phénomènes naturels indésirables leur ont créé des défis. Pour être plus précis, la survenue d'hémolyse et de thrombose provoque la formation de caillots sanguins à l'intérieur des pompes à sang et les empêche de fonctionner. L'hémolyse est la libération d'hémoglobine des globules rouges dans le plasma en raison de l'endommagement des membranes des cellules [7], tandis que la thrombose est la formation d'un caillot sanguin dans le système cardiaque et peut survenir à la fois dans les artères et les ventricules [8]. En raison de ce problème, des recherches approfondies ont été menées sur l'hémolyse et la thrombose au cours des dernières décennies. Les sujets incluent les aspects physiologiques de deux phénomènes [9–11], la relation entre l'hémolyse et la thrombose [12–14], la prédiction expérimentale de leur apparition [15–18] et la modélisation de phénomènes [19–21]. À l'heure actuelle, il est prouvé que la thrombose du système cardiovasculaire résulte d'une hémolyse [12,22]. En d'autres termes, le contrôle du niveau d'hémolyse dans un système VAD conduit à une diminution de la thrombose à l'intérieur de celui-ci.

D'un point de vue technique, une solution possible est de prédire et d'éliminer les sources du phénomène à l'aide de modèles mathématiques. La modélisation de l'hémolyse peut aider les développeurs de LVAD à réduire les risques du phénomène dans ces dispositifs. Cet objectif nécessite un modèle précis qui doit servir de lien entre les aspects mécaniques et physiologiques du flux sanguin.

Plus tôt dans les années 1960 et 1970, la relation entre la contrainte de cisaillement (τ) et le temps d'exposition (t), en tant que deux paramètres mécaniques, et les phénomènes d'hémolyse a été prouvée [56,60]. A cette époque, l'objectif des chercheurs était de déterminer un seuil d'apparition de l'hémolyse. Par exemple, Blackshear et al. [60] ont fourni une formulation explicite pour prédire la survenue d'une hémolyse (équation 39). Cette formule a ensuite été améliorée en ajoutant une contrainte de cisaillement seuil au modèle

$$\tau t^{0,5} = const, \tag{37}$$

L'équation ci-dessus ne peut pas prédire quantitativement la quantité de l'indice d'hémolyse et n'explique que les conditions d'apparition de ce phénomène. Par conséquent, un modèle mathématique était nécessaire pour prédire l'indice d'hémolyse. Le modèle de loi de puissance introduit par Giersiepen et al. [15] a été le premier à prédire localement ce phénomène. Dans l'équation proposée (équation 40), l'indice d'hémolyse H est calculé en fonction de la contrainte de cisaillement du champ d'écoulement ($\tau\ (Pa)$) et du temps ($t\ (s)$).

$$H = C\tau^{\alpha} t^{\beta} \tag{38}$$

Où C, α et β sont des constantes empiriques sans dimension égales à $3\,62 \times 10^{-7}$, $2{,}416$, and $0{,}785$, respectivement. Après cette première publication, des études plus expérimentales ont été menées par d'autres chercheurs pour les optimiser. L'étude la plus récente de Ding et al. [18] est la plus complète. Les auteurs ont conclu que l'hémolyse obtenue dans des conditions similaires n'est pas égale pour différentes espèces (Table 21).

Table 21. Coefficients du modèle de loi de puissance basés sur Ding et al. [18].

Species	$\boldsymbol{C}(\times \mathbf{10^{-7}})$	$\boldsymbol{\alpha}$	$\boldsymbol{\beta}$
Ovine	1.228	1.9918	0.6606
Human	0.3458	2.0639	0.2777
Porcine	67.01	1.098	0.2778
Bovine	9.772	1.444	0.2076

Dans l'équation (42), τ est un paramètre scalaire qui a l'unité de contrainte équivalente. Sur cette base, le principal défi consiste à sélectionner la contrainte de cisaillement équivalente à utiliser dans le

modèle de loi de puissance. Plus précisément, la question est de savoir comment trouver une expression de contrainte de cisaillement scalaire à partir du tenseur de contrainte.

Table 22. Différentes expressions proposées pour calculer la contrainte scalaire équivalente.

Définition	Référence
$\boldsymbol{\tau_b = \left(\frac{1}{2}\left[\left(\tau_{xx}-\tau_{yy}\right)^2+\left(\tau_{xx}-\tau_{zz}\right)^2+\left(\tau_{yy}-\tau_{zz}\right)^2+6\left(\tau_{xy}^2+\tau_{xz}^2+\tau_{yz}^2\right)\right]\right)^{\frac{1}{2}}}$	[82]
$\boldsymbol{\tau_s = \left(\frac{1}{3}\left(\tau_{xx}^2+\tau_{yy}^2+\tau_{zz}^2-\tau_{xx}\tau_{yy}-\tau_{xx}\tau_{zz}-\tau_{yy}\tau_{zz}\right)+\left(\tau_{xy}^2+\tau_{xz}^2+\tau_{yz}^2\right)\right)^{\frac{1}{2}}}$	[83]
$\boldsymbol{\tau_e = \left(\frac{1}{2}\left(\tau_{xx}^2+\tau_{yy}^2+\tau_{zz}^2\right)+\left(\tau_{xy}^2+\tau_{xz}^2+\tau_{yz}^2\right)\right)^{\frac{1}{2}}}$	[20]

L'une des dernières versions de la contrainte équivalente est celle proposée par Faghih et Sharp (2020) [84]. Dans cet article, les auteurs tentent d'étudier l'impact des différentes composantes du tenseur des contraintes sur le phénomène d'Hémolyse. Ils ont appliqué des contraintes de traction, compression et de cisaillement à l'aide de deux cas test distincts. En conclusion, ils ont constaté que l'hémolyse dépend plus composantes de traction, compression. Par conséquent, ils ont fourni une nouvelle expression de la contrainte de cisaillement équivalente, qui est basée sur un nouveau paramètre C_n :

$$\tau_n = \left(C_n^2\left(\tau_{xx}^2+\tau_{yy}^2+\tau_{zz}^2-\tau_{xx}\tau_{yy}-\tau_{xx}\tau_{zz}-\tau_{yy}\tau_{zz}\right)+\left(\tau_{xy}^2+\tau_{xz}^2+\tau_{yz}^2\right)\right)^{\frac{1}{2}} \quad (39)$$

Où C_n définit le poids des différents types de contraintes. Compte tenu des données expérimentales, $\sqrt{3}\,C_n = 33{,}69$ est annoncé comme la valeur optimale pour ce paramètre.

Cette thèse vise à étudier l'impact de la prise en compte des contraintes de traction, compression comme cause principale de l'hémolyse dans les trois cas tests : le benchmark de la buse FDA, le benchmark de la pompe FDA et la pompe à sang innovante FineHeart (l'ICOMS). Pour les deux premières géométries, les modèles standards fournis par la FDA, l'objectif est de valider la méthodologie numérique. Alors que pour le cas de test plus réaliste, la pompe cardiaque FineHeart, l'objectif final est de fournir quelques conseils pour réduire le niveau d'hémolyse.

6.2. Méthodologie Numérique et Résultats

6.2.1. Référence de buse de la FDA

Pour le benchmark de la buse FDA (Figure 104), premièrement, la précision de la simulation d'écoulement stationnaire a été validée en comparant la vitesse axiale normalisée prédite dans plusieurs sections avec les données expérimentales. À cette fin, les équations Reynolds-Averaged Navier-Stokes (RANS) en conjonction avec trois modèles de turbulence différents k-ϵ, k-ω et k-ω SST ont été utilisées et comparées. Des simulations en régime permanent ont été réalisées pour les deux orientations de la

tuyère ("Élargissement Brusque (ÉB)" et "Élargissement Progressive (ÉP)"). Il est important de préciser que toutes les simulations de cette thèse ont été réalisées avec le solveur commercial Ansys CFX v2020 R2 (ANSYS, Inc., Canonsburg, PA).

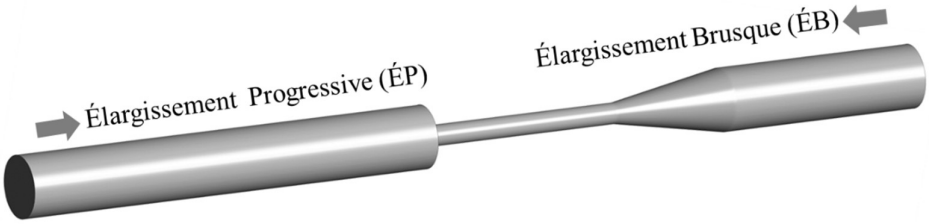

Figure 104. Géométrie de l'élément de référence de tuyère FDA [87].

La Figure 105-b et la Figure 105-c montrent une comparaison de la vitesse axiale normalisée entre les résultats numériques et les données expérimentales dans le cas d'une réduction brusque, dans les deux sections repérées à la Figure 105-a. Les résultats obtenus avec les trois modèles de turbulence testés sont tracés ici pour l'orientation de l'élargissement brusque. Les modèles k-ω et k-ω SST prédisent les profils de vitesse en bon accord avec les mesures expérimentales, tandis que des écarts plus importants peuvent être observés avec le modèle k-ϵ, en particulier en aval de la section réduite. Cela était attendu, car le modèle k-ϵ est bien connu pour générer de moins bons résultats dans les zones d'écoulement tourbillonnaires. Des tests identiques ont été réalisés dans le cas de l'élargissement progressif de la tuyère. Il est clair que le modèle de turbulence k-ω SST s'est avéré être le modèle le plus précis.

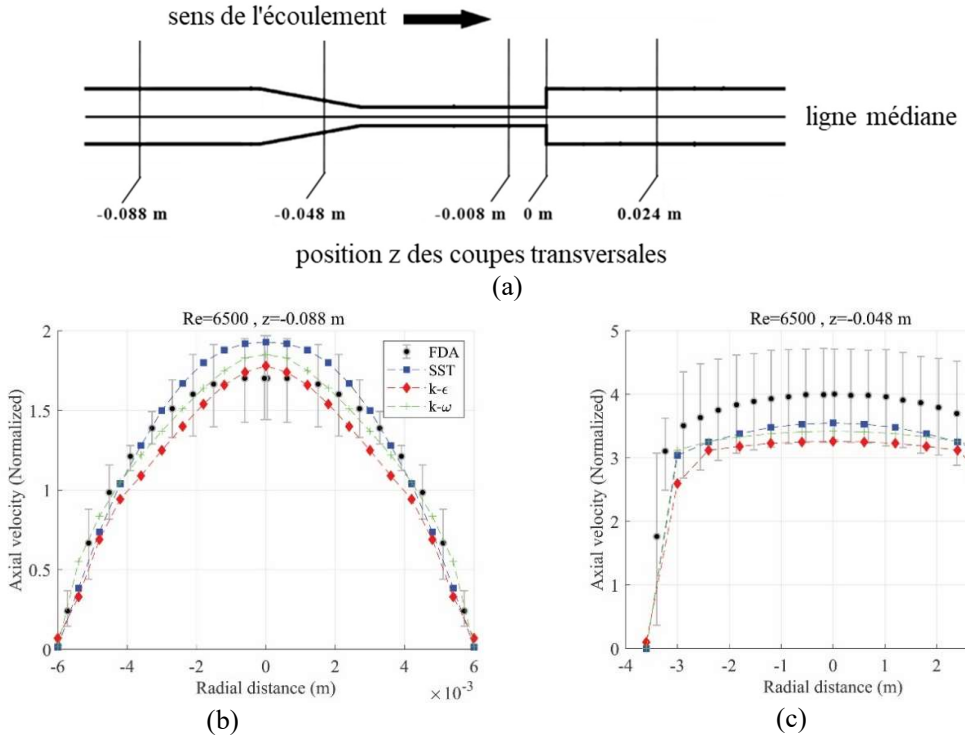

Figure 105. a) Géométrie du du cas test de la tuyère FDA et section transversale de sondage à côté de celle-ci. b,c) Comparaison entre les résultats expérimentaux et numériques : vitesses axiales à Re=6500 pour le cas test d'élargissement brusque aux positions z=-0,088 et z=-0,048, respectivement.

Dans l'étape suivante, les indices d'hémolyse ont été calculés en utilisant différentes expressions pour la contrainte équivalente. Des calculs du modèle d'hémolyse (équation 42) en plus des équations de Navier-Stokes ont été réalisés, en utilisant les trois contraintes de cisaillement équivalentes (τ_s, τ_e, τ_n) pour trois conditions de fonctionnement différentes de la tuyère (voir Figure 106-a). Ci-après, les résultats CFD actuels sont comparés à la fois aux données expérimentales et aux résultats CFD précédents fournis par Tobin et Manning (2020) [86]. Dans cet article, le débit à l'intérieur de la tuyère est calculé à l'aide d'un modèle turbulent LES, en conjonction avec les constantes du modèle modifié de Ding et al. [18] ($\beta = 0{,}1$ au lieu de $\beta = 0{,}2076$).

La Figure 106-b montre la comparaison entre les résultats actuels, les données expérimentales rapportées dans [90], et les calculs CFD précédents [86], pour les trois conditions d'écoulement. On peut observer que l'expression de la contrainte de cisaillement équivalente a un impact important sur les résultats. Plus précisément, les valeurs MIH obtenues avec τ_s et τ_e sont bien inférieures à celles obtenues avec τ_n. Par conséquent, pour le point de fonctionnement ÉP6, τ_s et τ_e entraînent une sous-estimation de MIH. D'autre part, τ_n avec la valeur par défaut de C_n ($\sqrt{3}C_n = 33{,}69$), donne des plages correctes de valeurs MIH pour toutes les conditions de fonctionnement.

Indice	Position	Débit (l/min)	Re_{FDA}
DP5	Élargissement Progressive (ÉP)	5	6650
DP6		6	7860
ES6	Élargissement Brusque (ÉB)	6	8020

(a)

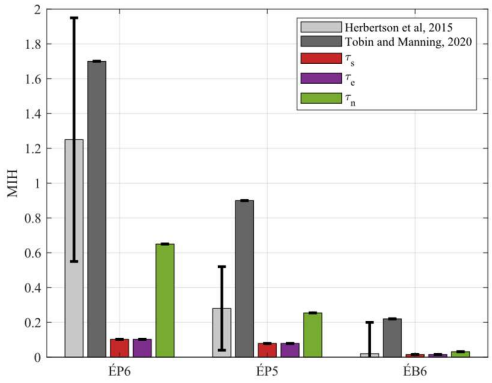

(b)

Figure 106. a) Conditions d'écoulement des tests d'hémolyse rapportés dans [90]. b) Indice d'hémolyse : comparaison entre les résultats actuels (avec 3 expressions différentes de la contrainte de cisaillement équivalente), les données expérimentales de la FDA [90], et les résultats numériques de Tobin et Manning [86].

Dans ce cas, l'impact de l'augmentation des contraintes d'extension sur l'hémolyse prédite est étudié en ajoutant un coefficient C_n à la contrainte équivalente (équation 43). La Figure 107 montre l'impact de C_n sur MIH pour différentes espèces, dans les conditions d'écoulement "DP6", en utilisant les constantes du modèle proposées par Ding et al. [18]. C_n a un fort effet sur MIH, en particulier pour le sang humain et bovin. De plus, à mesure que C_n augmente, la différence entre les valeurs MIH obtenues pour différentes espèces devient plus grande. D'un point de vue mathématique, ceci est une conséquence directe de l'utilisation de différentes valeurs de coefficients α pour les différentes espèces.

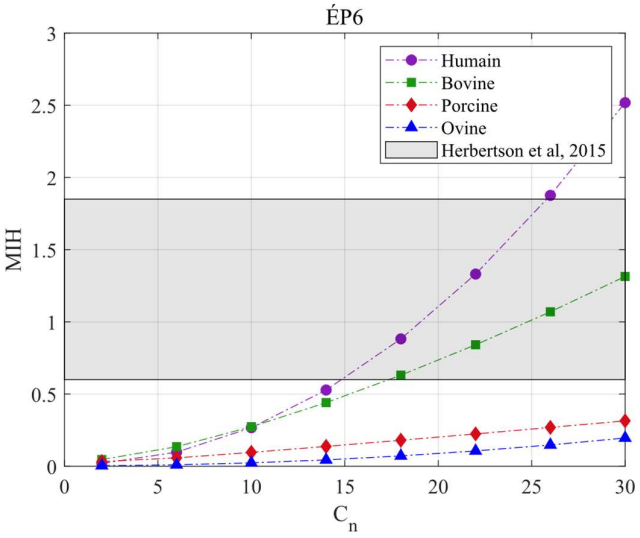

Figure 107. Impact du paramètre C_n sur l'indice d'hémolyse pour différentes espèces et comparaison avec les données expérimentales de la FDA [90] pour les conditions d'écoulement DP6, en utilisant les constantes du modèle proposées par Ding et al. [18].

À ce stade, nous devons reconsidérer Table 21 pour mieux comprendre le comportement des courbes. Par exemple, la courbe du sang humain est inférieure à celle du sang bovin pour les faibles valeurs de C_n, alors qu'elle augmente à un rythme beaucoup plus élevé et va donc bien au-dessus pour les plus grandes valeurs de C_n. En effet, la courbe du sang bovin croît semi-linéairement ($\alpha = 1{,}444$) tandis que la courbe du Sang Humain a un comportement exponentiel ($\alpha = 2{,}0639$). Donc, généralement, on peut s'attendre à ce que le comportement d'une espèce dépende du coefficient α. Dans ce cas, la courbe du sang ovin n'est pas cohérente avec les autres car nous nous attendons à ce qu'elle soit supérieure celles du sang porcin ou du sang bovin mais inférieure à celle du sang humain ($\alpha_{Human} > \alpha_{Ovine} > \alpha_{Bovine} > \alpha_{Porcine}$). Dans ce cas l'impact de deux autres constantes C et β se traduit par un comportement différent de la courbe MIH de l'Ovin.

Enfin, il est conclu que l'indice d'hémolyse serait dans une plage fiable de $18<C_n<30$. De plus, l'impact de différentes valeurs de C_n a été étudié pour plusieurs espèces. En comparant les résultats, le coefficient C_n peut faire une large gamme d'hémolyse, en particulier pour des valeurs plus élevées de celui-ci.

6.2.2. Référence de la pompe de la FDA

Pour le le cas test de la pompe FDA [88] (Figure 108), les équations moyennées de Navier-Stokes (RANS) sont résolues en régime transitoire, en utilisant le modèle de turbulence k-ω SST, pour simuler l'hémodynamique du flux sanguin. Le modèle de turbulence k-ω SST a été précédemment signalé comme le modèle de turbulence RANS le plus fiable pour la simulation de la pompe FDA [75,97,98,102]. Le pas de temps utilisé dans les simulations est calculé en fonction de la vitesse de rotation de la pompe, pour avoir 2 degrés de rotation par pas de temps (soit 0,13 ms pour n=2500 tr/min

et 0,095 ms pour n=3500 tr/min), et les simulations ont été menées pendant 24 rotations. Dans toutes les simulations, les critères de convergence basés sur les résidus RMS ont été fixés à 10^{-5}, avec un maximum de 25 itérations internes autorisées à chaque pas de temps.

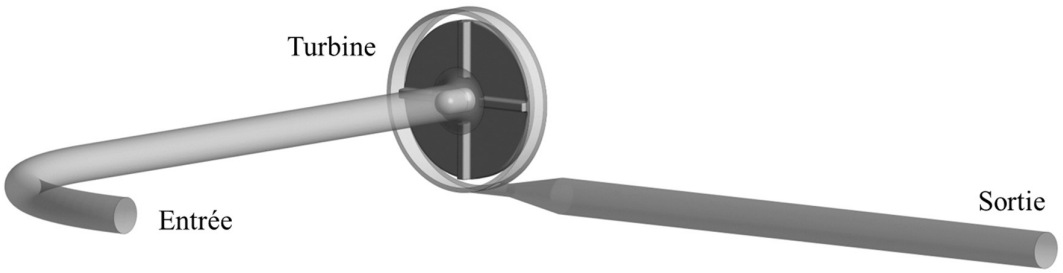

Figure 108. Géométrie du benchmark pompe FDA [88].

Les paramètres hémodynamiques, y compris la vitesse et la pression, ont été validés en comparant les résultats CFD avec les données expérimentales de la FDA. Tout d'abord, une comparaison qualitative entre les données expérimentales et numériques est montrée en traçant les contours de vitesse dans un plan de coupe situé à 1,2 mm de la surface supérieure des aubes de la turbine (voir Figure 48). Dans les mesures FDA PIV, le champ de vitesses a été obtenu en faisant la moyenne des résultats de 500 à 2500 paires d'images capturées à une vitesse de rotor donnée (avec une position constante de l'une des pales par rapport à la conduite de sortie) [88]. De même, les données numériques ont été moyennées sur les 10 derniers pas de temps calculés avec une aube dans la même position.

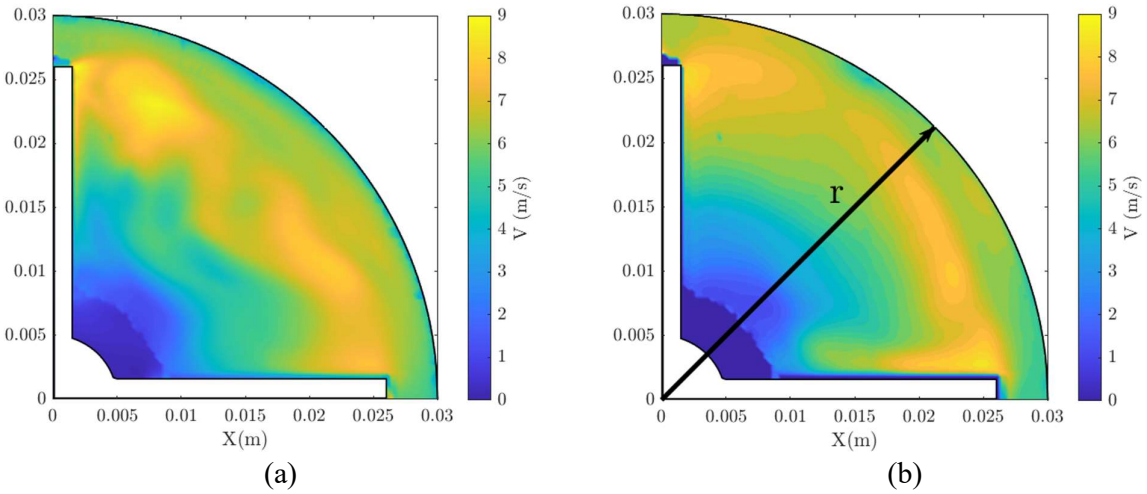

Figure 109. Distributions de l'amplitude de la vitesse dans un plan de coupe dans la roue et comparaison entre les mesures FDA PIV [88] (b) et les prédictions numériques (a) pour n = 3500 rpm et Q = 6lpm.

La Figure 110-a montre l'évolution de l'amplitude de la vitesse le long d'une ligne diagonale à 45° (ligne 'r' montrée sur la Figure 109-b) dans la même section. Les résultats numériques sont à nouveau comparés aux données obtenues précédemment par PIV par deux laboratoires différents et notées ‘lab1’ et ‘lab2’. Malgré quelques déviations en bout de pale, cela montre que la CFD est en bon accord avec les expériences. L'erreur relative entre la vitesse calculée et celle obtenue par PIV ($e=|V_{PIV}-V_{CFD}|/V_{PIV}$, lab. 2) est portée par la même ligne radiale sur la Figure 110-b. On constate qu'il est toujours inférieur à 10%, ce qui confirme la bonne précision de la simulation numérique au sein de la roue.

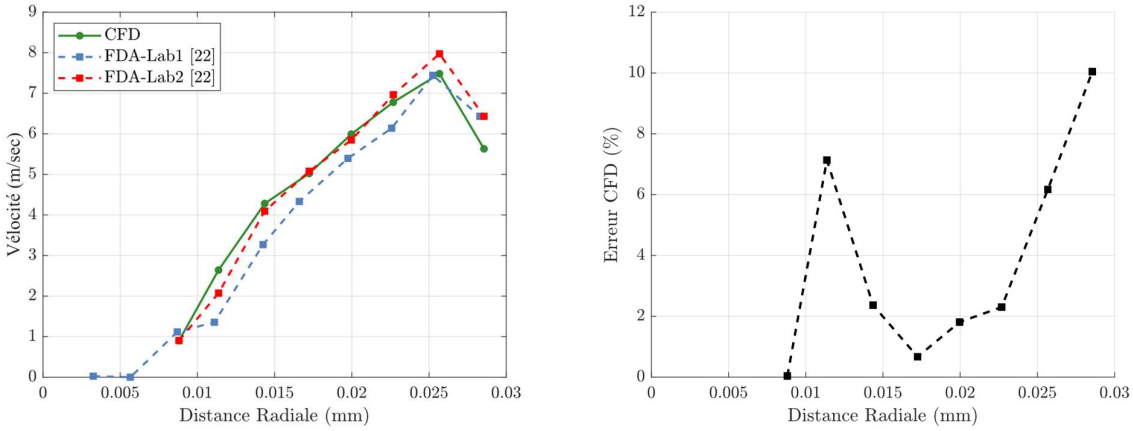

(a) (b)

Figure 110. a) Comparaison entre les profils numériques et expérimentaux de l'amplitude de la vitesse par rapport à la distance radiale du centre de rotation. b) Erreur entre la vitesse calculée par CFD et les mesures PIV (Lab 2).

L'élévation de pression dans la pompe FDA est un autre point de contrôle pour la validation hémodynamique. La différence entre la pression totale entre l'entrée et la sortie a été calculée pour chaque cas ($\Delta P = P_{Tot\ Out} - P_{Tot\ in}$). Des données expérimentales existent pour deux fluides opératoires : l'iodure de sodium utilisé pour les mesures PIV et le sang porcin utilisé pour les tests d'hémolyse. D'autre part, des simulations CFD ont été menées avec les propriétés fluides des expériences hémodynamiques de la FDA (iodure de sodium comme matériau). La Figure 111 montre la comparaison entre les valeurs expérimentales et numériques de l'élévation de pression. Les prédictions CFD sont en assez bon accord avec les expériences : les valeurs se situent toujours dans la plage d'incertitude des expériences, et les écarts sont généralement inférieurs à 10 %. Cela confirme que le champ d'écoulement est assez correctement prédit par la CFD, en ce qui concerne à la fois les aspects globaux et les propriétés d'écoulement locales, de sorte que le cadre numérique proposé peut être utilisé pour effectuer des calculs d'hémolyse.

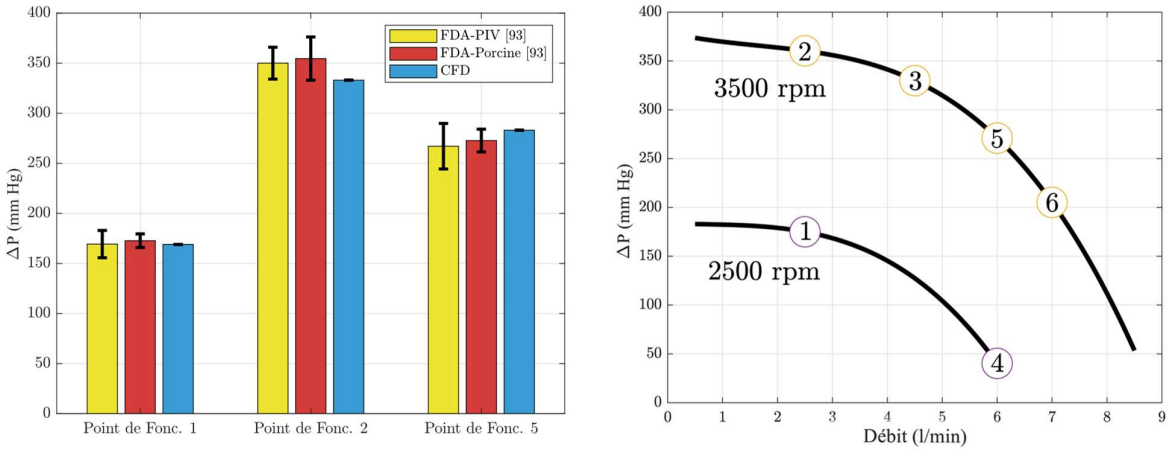

(a) (b)

Figure 111. Élévation de pression dans la pompe pour trois conditions de fonctionnement. Jaune : Mesures FDA PIV, Rouge : FDA avec du sang dans les tests d'hémolyse, et Bleu : Résultats de la simulation CFD avec les propriétés du matériau FDA PIV (iodure de sodium).

Dans l'étape suivante, l'équation de transport standard du modèle de loi de puissance a été couplée aux équations de fluide dans la simulation. À ce stade, l'objectif principal est d'évaluer l'efficacité d'une nouvelle expression de la contrainte équivalente fournie par Faghih et Sharp [84] (équation 41). Pour cela, les prédictions numériques de l'indice d'hémolyse sont comparées aux mesures expérimentales [88] pour trois conditions opératoires. Pour respecter la définition originale [84], le paramètre C_n est fixé égal à 19,45 sachant que les tests expérimentaux ont été retenus pour le sang humain et non pour le sang porcin. La Figure 112 montre la comparaison entre le MIH prédit par CFD et les mesures expérimentales. Il est clair que les valeurs CFD sont à l'intérieur de la plage d'incertitude expérimentale pour tous les points de fonctionnement. Cependant, toutes les valeurs MIH calculées sont inférieures aux valeurs moyennes de l'indice d'hémolyse mesuré. Cette observation nous a motivés à étudier l'impact du paramètre C_n sur les prédictions CFD.

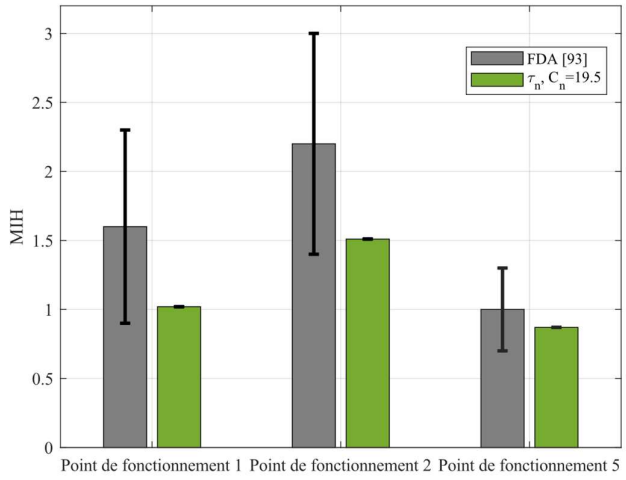

Figure 112. MIH calculé sur la base de la nouvelle définition de la contrainte équivalente définie par Faghih et Sharp [84] (C_n=19,45) pour trois points de fonctionnement de la pompe FDA.

Des simulations ont ainsi été réalisées pour une large gamme du paramètre C_n (2<C_n<30 avec un intervalle de 4). De plus, ils ont été répétés pour différentes espèces afin d'étudier simultanément l'influence du paramètre C_n et les propriétés du sang. La figure 101 montre les résultats pour le point de fonctionnement 1. Les valeurs MIH ont été tracées par rapport au paramètre C_n avec une échelle logarithmique. En considérant ce graphique, il est clair que l'augmentation du paramètre C_n entraîne une augmentation exponentielle du MIH. Ainsi, l'ajustement d'une valeur fiable peut améliorer efficacement la précision des simulations.

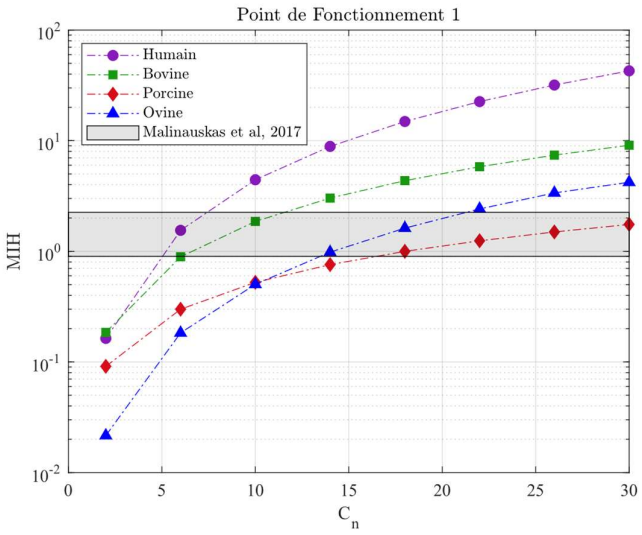

Figure 113. MIH en fonction de C_n pour différentes espèces et sa comparaison avec les données expérimentales pour le point de fonctionnement 1.

Généralement, C_n a un effet significatif sur l'hémolyse, en particulier pour les espèces où le coefficient α dans le modèle est le plus grand, par exemple le sang humain. En comparant la courbe obtenue avec le sang bovin avec la gamme expérimentale de MIH dans trois conditions de fonctionnement différentes, on pourrait conclure qu'une gamme appropriée pour la constante est $18<C_n<27$, avec une valeur optimale autour de 22 - 23.

6.2.3. Pompe à sang FineHeart (l'ICOMS)

Enfin, l'étude a mené des simulations transitoires en utilisant des configurations identiques pour la pompe à sang innovante FineHeart, l'ICOMS. L'objectif final de cette étape est de fournir quelques suggestions pour améliorer les performances de l'ICOMS en terme d'hémolyse. Pour l'hémodynamique, l'outil PIV est utilisé pour mesurer l'amplitude de la vitesse et sa direction dans la configuration de la boîte solide, qui représente l'environnement du ventricule, avec la pompe ICOMS insérée dedans (comme illustré à la Figure 114). Pour les simulations de banc d'essai PIV, l'ICOMS est positionné verticalement à l'intérieur du boîtier PIV, où la sortie de la pompe est ajustée devant la sortie du boîtier. Dans ce cas, l'axe de rotation de la pompe est aligné avec la conduite de sortie. La distance entre la sortie de la pompe et la paroi adjacente est fixée à 16 mm, en respectant la configuration expérimentale. Dans ce travail, les résultats basés sur la CFD d'un cas de test similaire sont comparés aux données expérimentales obtenues par FineHeart. Afin de fournir les résultats dans un format standard et comparable, le logiciel Matlab a été utilisé pour le post-traitement.

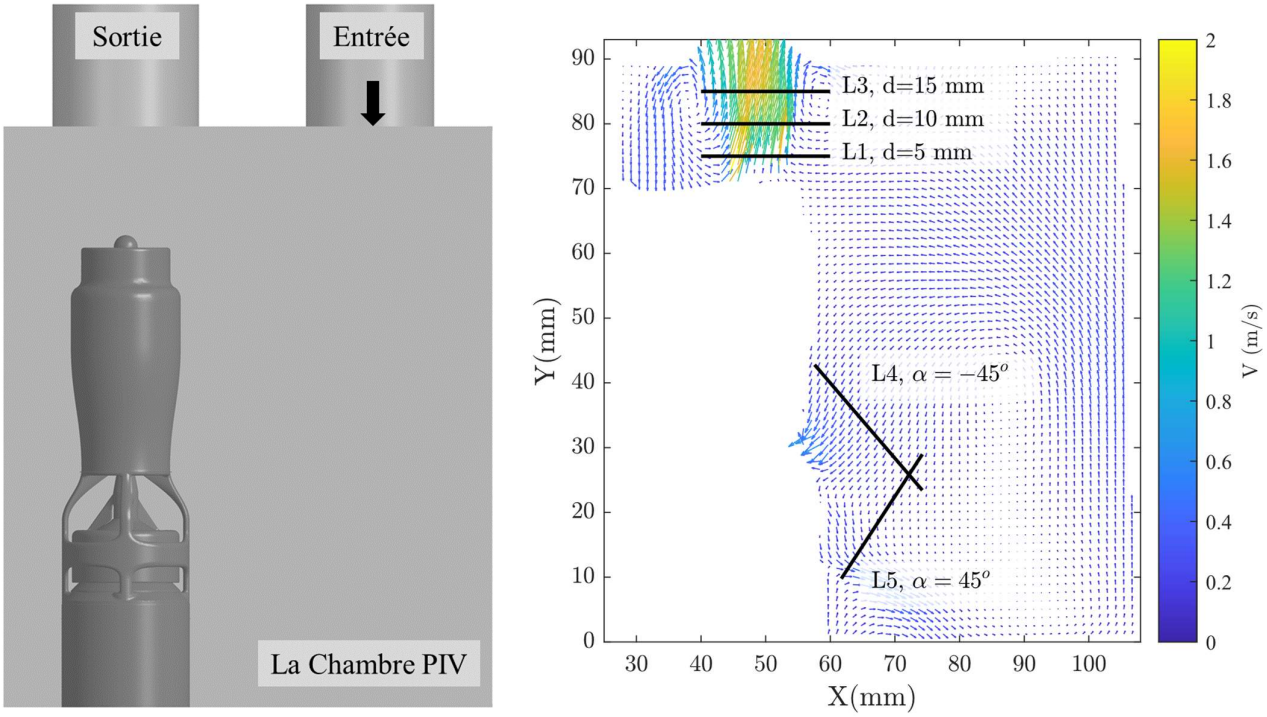

(a) (b)

Figure 114. a)représentation schématique de la chambre PIV avec la pompe ICOMS positionnée à l'intérieur. b)exemple de champ de vitesses PIV mesurées. Cinq lignes différentes ont été localisées dans des zones importantes afin de sonder les paramètres de vitesse.

Cinq lignes ont été identifiées dans le plan médian de la boîte (comme illustré à la Figure 114). Des profils d'amplitude de vitesse ont été extraits de ces lignes pour des résultats expérimentaux et numériques. Les lignes L1, L2 et L3 ont été choisies pour quantifier la vitesse à la sortie de la pompe où les gradients de vitesse les plus élevés ont été observés. La ligne L4 a été positionnée au niveau de la région d'entrée de la pompe avec un angle de rotation de α = -45° par rapport à l'axe x. Enfin, la ligne L5 a été spécifiée à un angle de α=45° degrés par rapport au même axe devant la sortie de la pompe secondaire. La Figure 115-a montre une comparaison entre les mesures PIV et les résultats CFD pour la ligne 1, y compris les données PIV moyennes, les résultats CFD moyens et les profils CFD instantanés dans un seul graphique. La raison de la comparaison des résultats CFD moyens avec les résultats PIV est que les composantes de vitesse pour les mesures PIV ont été moyennées sur de nombreuses paires d'images (300 paires). Par conséquent, pour obtenir une approche similaire, les profils de vitesse CFD ont également été moyennés, mais pour une période des dix derniers pas de temps. Pour résumer, la raison pour laquelle les résultats CFD moyens ont été comparés aux résultats PIV pour la ligne 1 est que les mesures PIV elles-mêmes ont été moyennées sur une période de temps pour obtenir des résultats plus fiables, et les profils instantanés CFD ont montré des fluctuations claires dans le champ de vitesse. La moyenne des profils CFD a permis d'éliminer ces fluctuations et de faire des comparaisons fiables avec les données PIV. La méthode CFD s'est avérée significativement précise pour prédire qualitativement le comportement du profil de vitesse. La comparaison quantitative de la Figure 115-b a

montré que le pourcentage maximal d'erreur CFD était de près de 20 %, alors que pour la plupart des points de sonde, il était inférieur à 10 %, ce qui est considéré comme acceptable.

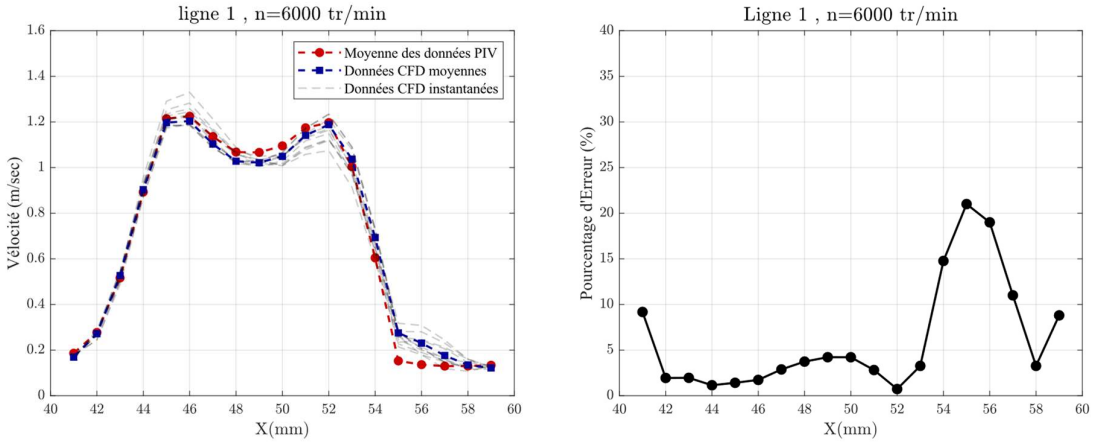

(a) (b)

Figure 115. Comparison between PIV measurements and CFD results for Line 1 (n=6000 rpm). a) Averaged profiles of the velocity magnitudes. b) Error percentage of the CFD calculations for the same profiles.

Un processus similaire a également été suivi pour les autres lignes. Les résultats indiquent qu'il existe une corrélation claire entre les profils de vitesse prédits par CFD et ceux de PIV. En conclusion, il est évident que la méthodologie de simulation est suffisamment précise en terme d'hémodynamique. Ainsi, il peut être mis en œuvre pour les simulations d'hémolyse.

Dans l'étape suivante, l'équation de transport standard du modèle de loi de puissance a été couplée aux équations de fluide dans la simulation. Une méthodologie similaire avec la pompe à sang de la FDA a été utilisée pour modéliser le phénomène à l'intérieur de l'ICOMS. Dans ce cas, les conditions de fonctionnement de la pompe ont été ajustées en fonction des configurations expérimentales des tests FineHeart. FineHeart a mené des expériences d'hémolyse sur l'ICOMS dans deux conditions opératoires : « TD haut débit » et « TD bas débit » (voir Figure 116-a). Les expériences consistaient à mesurer l'hémoglobine libérée dans le flux sanguin à différents intervalles de temps, avec une durée totale d'expérience de 360 minutes (60 minutes par intervalle).

La Figure 116-b montre les résultats d'une expérience dans laquelle les taux d'hémoglobine libre ont été mesurés dans le temps pour deux conditions de fonctionnement différentes, appelées « TD haut débit » et « TD bas débit » La ligne verte, qui représente des vitesses de rotation plus élevées dans cette condition, montre une pente plus raide que l'autre ligne, indiquant une plus grande augmentation des niveaux d'hémoglobine libre au fil du temps. Le fait que les deux lignes partent de niveaux similaires d'hémoglobine libre (environ 15 mg/dL) suggère que les conditions initiales étaient les mêmes pour les deux conditions opératoires. Au fil du temps, cependant, la différence entre les deux lignes devient plus prononcée, la ligne verte montrant des niveaux significativement plus élevés d'hémoglobine libre à la fin de l'expérience (environ 7-8 mg/dL de plus).

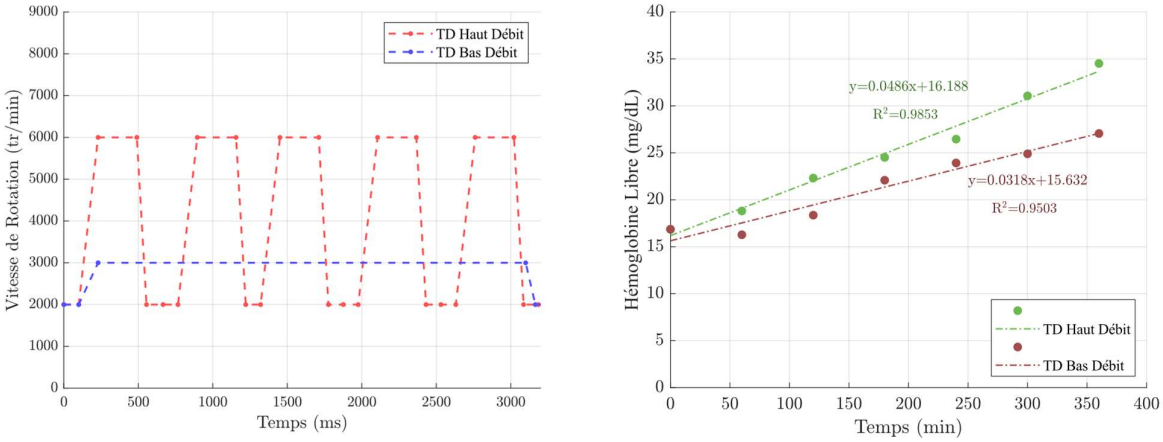

(a) (b)

Figure 116. a) Conditions opératoires et différentes configurations de l'ICOMS pour les tests d'hémolyse « TD haut débit » et « TD bas débit ». b) Hémoglobine libre en fonction du temps pour les deux conditions de fonctionnement de l'ICOMS.

Les simulations ont été réalisées en utilisant les deux configurations, comme indiqué précédemment. Tout d'abord, la pompe a été simulée dans la condition « TD haut débit » avec une vitesse de rotation plus élevée. Les valeurs MIH calculées ont ensuite été validées par rapport aux données expérimentales de FineHeart. Pour garantir la précision, les calculs ont été répétés trois fois avec différents niveaux de convergence (10^{-5}, 10^{-6} et 10^{-7}). La Figure 117 montre une comparaison entre les valeurs MIH calculées instantanées aux trois différents niveaux de convergence et les mesures expérimentales FineHeart pour la configuration « TD haut débit ». La plage d'incertitude expérimentale est représentée par une zone grise transparente sur le graphique. Il est évident que la simulation avec le plus grand critère de convergence ($<10^{-5}$) sous-estime le MIH. Cependant, lorsque le niveau de convergence est abaissé à 10^{-6}, les courbes prédites se situent dans la plage acceptable. De plus, réduire davantage le niveau de convergence (à 10^{-7}) n'entraîne pas une amélioration significative de la courbe prédite. Ainsi, la même valeur a été retenue comme critère de convergence pour la simulation « TD bas débit ». Il a été observé que la méthodologie de simulation est également valable pour cette condition de fonctionnement.

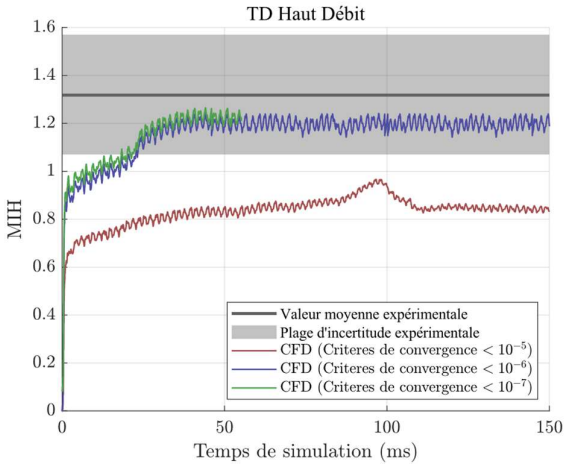

Figure 117. Comparaison entre le MIH calculé avec trois niveaux de convergence différents et les mesures expérimentales FineHeart pour la configuration de fonctionnement « TD haut débit ».

6.3. Conclusion

Les défis du développement des pompes à sang incluent l'apparition de phénomènes naturels indésirables tels que l'hémolyse et la thrombose. Une solution potentielle consiste à utiliser des modèles mathématiques pour prédire et éliminer les sources de ces phénomènes, en particulier la modélisation de l'hémolyse pour les dispositifs d'assistance ventriculaire gauche (LVAD). Cette thèse présente une nouvelle méthodologie pour simuler le phénomène d'hémolyse basée sur des mesures expérimentales, avec l'objectif principal d'évaluer le nouveau modèle à l'aide d'outils numériques dans différentes géométries. Trois cas de test ont été examinés : Le cas test de la tuyère FDA, le cas test de la pompe FDA et la pompe à sang FineHeart (ICOMS), dans le but de fournir des recommandations pour réduire l'indice d'hémolyse de la pompe à sang FineHeart.

L'étude a commencé par des simulations numériques pour valider le nouveau modèle d'hémolyse pour le cas test de la tuyère FDA. Les simulations ont été effectuées à l'aide de trois modèles turbulents, et le modèle k-ω SST s'est avéré le plus fiable. L'indice d'hémolyse a été calculé en utilisant trois expressions différentes de la contrainte de cisaillement équivalente et les valeurs obtenues ont été comparées aux données expérimentales. Les résultats ont montré que l'expression τ_n était la plus fiable. l'effet de la constante C_n a été étudié dans l'expression de τ_n pour différentes espèces avait un impact significatif sur l'hémolyse, en particulier pour le sang bovin et le sang humain. Enfin, une plage appropriée pour la constante a été déterminée comme étant $18 < C_n < 30$ en comparant la courbe obtenue avec du sang bovin à la plage expérimentale de MIH dans trois conditions de fonctionnement différentes.

La deuxième partie de l'étude s'est concentrée sur le développement de méthodes numériques pour prédire l'hémodynamique et l'hémolyse du flux sanguin à l'intérieur pompe FDA. Le modèle Power-law a été utilisé avec l'approche eulérienne et la même expression de contrainte de cisaillement équivalente que la première partie de l'étude a été testée.. Les prédictions numériques ont été validées en comparant les résultats CFD aux mesures FDA PIV pour trois conditions opérationnelles. L'indice d'hémolyse a été calculé en utilisant la contrainte équivalente τ_n et s'est avéré fournir des résultats précis malgré les incertitudes expérimentales. L'impact de la constante C_n sur l'hémolyse pour différentes espèces conclu que la plage appropriée pour la constante est $18<C_n<27$.

Des simulations en régime permanent et transitoire pour prédire les aspects hémodynamiques et hémolytiques de la pompe à sang FineHeart (ICOMS) ont été menées, visant à identifier les sources d'hémolyse dans l'appareil. Les simulations ont été validées sur la base de tests de boucle de corrélation et de mesures PIV, et les résultats ont montré un bon accord entre les données numériques et expérimentales. Le modèle d'hémolyse validé a été ajouté aux simulations et les paramètres hémolytiques ont été calculés, comparés et validés avec les données FineHeart pour deux configurations de fonctionnement de la pompe. Les sources d'hémolyse comme des espaces entre les pièces rotatives

et fixes et les bords d'attaque et de fuite des pales ont été identifiées. quelques suggestions pour améliorer la conception des pompes à sang axiales sur la base de ces résultats ont également été fournis.

À la suite de cette recherche, nous espérons contribuer au traitement des patients cardiaques en optimisant la conception des pompes à sang.